Univerzita Karlova

Přírodovědecká Fakulta

Makromolekulární Chemie

Ing. Kristýna Kolouchová

*Samouspořádané polymerní systémy na bázi poly[(N-2,2-difluorethyl)akrylamidu]
jako diagnostické a theranostické tracery pro zobrazování ^{19}F magnetickou rezonancí*

Disertační práce

Školitel: Mgr. Martin Hrubý, DSc.

Ústav Makromolekulární Chemie, AV ČR, v.v.i

Praha

2020

Charles University

Faculty of Science

Macromolecular Chemistry

Ing. Kristýna Kolouchová

Self-Assembled Polymer Systems Based on Poly[(N-2,2-difluoroethyl)acrylamide] as Diagnostic and Theranostic Tracers for ^{19}F Magnetic Resonance Imaging

Doctoral thesis

Supervisor: Mgr. Martin Hrubý, DSc.

Institute of Macromolecular Chemistry CAS

Prague

2020

Prohlašuji, že jsem tuto disertační práci vypracovala samostatně a výhradně s použitím citovaných pramenů, literatury, dokumentace přístrojů a dalších odborných zdrojů. Při jejím vypracovávání byla použitá data získaná ve spolupráci s mými kolegy.

Prohlašuji, že jsem tuto práci ani žádnou její podstatnou část nepředložila k získání jiného či stejného akademického titulu.

V Praze dne 1. 10. 2020 Kristýna Kolouchová

Poděkování

Acknowledgement

Table of contents

List of abbreviations

Aβ	amyloid-β
ACVA	4,4'-azobis(4-cyanovaleric acid)
AD	Alzheimer's disease
AIBN	2,2′-azobis(2-methylpropionitrile)
ATRP	atom transfer radical polymerization
BocAEA	*N*-(2*N*'-boc-aminoethyl)acrylamide
CAC	critical association concentration
CAs	contrast agents
COSY	correlation spectroscopy
CTA	chain transfer agent
DDs	drug delivery systems
DL	drug loading
DLS	dynamic light scattering
DMSO	dimethyl sulfoxide
DOSY	diffusion ordered spectroscopy
DR	drug loading
EPR	enhanced permeability and retention
EXSY	exchange spectroscopy
FcAEA	*N*-[2-(*N*'-ferrocenylamido)ethyl]acrylamide]
FDA	Food and Drug Administration Agency
GIT	gastrointestinal tract
HEAM	*N*-(2-hydroxyethyl)acrylamide
HIFU	high intensity focus ultrasound
HSQC	heteronuclear single quantum coherence spectroscopy
ImPAM	*N*-[3-(*1H*-imidazole-1-yl)propyl]acrylamide
LCST	lower critical solution temperature
MALS	multiangle light scattering
MRI	magnetic resonance imaging
MRS	magnetic resonance spectrum
NMR	nuclear magnetic resonance
NMRI	nuclear magnetic resonance imaging
NOESY	nuclear Overhauser effect spectroscopy
PDFEA	poly[*N*-(2,2-difluoroethyl)acrylamide]
PEG	poly(ethylene glycol)
PERFECTA	1,3-bis[[1,1,1,3,3,3-hexafluoro-2-(trifluoromethyl)propan-2-yl]oxy]-2,2-bis[[1,1,1,3,3,3-hexafluoro-2-(trifluoromethyl)propan-2-yl]oxymethyl]propane
PET	positron emission tomography
PFC	fluorinated compounds
PFPE	perfluoropolyethers
PFCE	perfluoro-15-crown-5-ether
PFOB	perfluorooctyl bromide
PMeOx	poly(2-methyl-2-oxazoline)
PNIPAm	poly(*N*-isopropyl acrylamide)
POFPMA	poly[*O*-(2,2,3,3,4,4,5,5-octafluoropentyl methacrylate)]

PPFS	poly(2,3,4,5,6-pentafluorostyrene)
PTFEA	poly[O-(2,2,2-trifluorethyl)acrylate]
PTFEMA	poly[O-(2,2,2-trifluorethyl) methacrylate]
RAFT	reversible addition fragmentation chain transfer
RARE	rapid acquisition with relaxation enhancement
RF	radiofrequency
RI	refractive index
ROS	reactive oxygen species
ROMP	ring-opening metathesis polymerization
SANS	small-angle neutron scattering
SAXS	small-angle X-ray scattering
SEC	size exclusion chromatography
SLS	static light scattering
SPECT	single-photon emission computed tomography
SPIONs	superparamagnetic iron oxide nanoparticles
TE	echo time
TEM	transmission electron microscopy
TR	repetition time
UTE	ultrashort echo time
ZTE	zero echo time

Abstract

In this doctoral thesis we describe a series of stimuli-responsive polymers which could be used as diagnostic tools or as smart drug delivery systems with simultaneous diagnosis (theranostics). All hereby mentioned polymers are thermoresponsive copolymers of (*N*-2,2-difluoroethyl)acrylamide exhibiting lower critical solution temperature in aqueous milieu. This means that they are water-soluble at low temperature while when heated above a certain temperature, they self-assemble into nano- or macro- sized assemblies. Because of the high concentration of fluorine atoms, all these polymers could be used as ^{19}F MRI tracers.

We designed multiple different thermoresponsive, thermo- and pH-responsive, thermo-and reactive-oxygen-species-responsive polymers that could find numerous discussed applications in human medicine. We investigated their physico-chemical properties with ^{1}H and ^{19}F nuclear magnetic resonance (NMR), size exclusion chromatography (SEC), elemental analysis, dynamic light scattering (DLS), static light scattering (SLS), small angle neutron scattering (SANS), small-angle X-ray scattering (SAXS), and turbidimetry. After the physicochemical optimization of the parameters for the selected applications, their biocompatibility was tested *in vitro*. Several promising polymers were tested *in vivo* on animal models. The clinical applicability of our polymers was further confirmed *via* merged ^{1}H and ^{19}F MR imaging of our polymers *in vitro* as a phantom study and *in vivo* with a rat model. One polymer was tested using an instrument currently used in human medicine.

Keywords: ^{19}F MRI tracer, thermoresponsive polymers, self-assembly, theranostic, multi-responsivity

Abstrakt

V rámci této disertační práce jsme připravili a charakterizovali celou řadu polymerů citlivých na vnější podněty, které mají potenciální využití jako látky pro neinvazivní zobrazování v medicíně a zároveň jako chytré systémy na cílené doručování léčiv (tzv. theranostika). Všechny systémy popsané v této disertační práci jsou na bázi termoresponzivních kopolymerů (N-2,2-difluorethyl)akrylamidu, které vykazují tzv. dolní kritickou rozpouštěcí teplotu. Tyto polymery jsou rozpustné za nízké teploty a po jejím zvýšení jsou schopné vytvářet samouspořádané supramolekulární částice, což nám umožňuje připravit částice z roztoku polymeru pouze změnou teploty z laboratorní teploty na teplotu lidského těla. Díky vysoké koncentraci magneticky ekvivalentních atomů fluoru jsou všechny tyto polymery vhodné pro zobrazování pomocí fluorové magnetické resonance (^{19}F MRI).

Připravili jsme řadu různých termoresponsivních, termo- a pH- responsivních, termo- a ROS-responsivních (reaktivní formy kyslíku) kopolymerů, které mají potenciální využití pro širokou škálu aplikací v medicíně. Tyto systémy jsme charakterizovali pomocí různých instrumentálních metod jako jsou ^{1}H a ^{19}F nukleární magnetická resonance (NMR), gelová permeační chromatografie (SEC), elementární analýza, dynamický a statický rozptyl světla (DLS, SLS), maloúhlový rozptyl neutronů (SANS), maloúhlový rozptyl rentgenového záření (SAXS) a turbidimetrie. Poté jsme testovali jejich biokompatibilitu v různých *in vitro* studiích a vybrané polymery byly testovány i *in vivo*. Aplikovatelnost v klinické praxi byla potvrzena pomocí experiment testovaném na MRI běžně používané pro klinickou praxi na pacientech, kde byl instrument modifikován fluorovou sondou a měření bylo prováděno na bázi sloučení výstupu z protonové a fluorové MRI.

Klíčová slova: ^{19}F MRI tracer, termoresponzivní polymery, samouspořádané systémy, theranostika, multi-responzivita

List of publications and contributions at conferences

Publications included into this thesis

Kolouchova, K.; Sedlacek, O.; Jirak, D.; Babuka, D.; Blahut, J.; Kotek, J.; Vit, M.; Trousil, J.; Konefal, R.; Janouskova O.; Podhorska, B.; Slouf, M.; Hruby, M. Self-Assembled Thermoresponsive Polymeric Nanogels for ^{19}F MR Imaging. *Biomacromolecules* **2018**, *19*, 3515-3524.

Babuka, D.; **Kolouchova, K.;** Hruby, M.; Groborz, O.; Tosner, Z.; Zhigunov, A.; Stepanek, P. Investigation of the internal structure of thermoresponsive diblock poly(2-methyl-2-oxazoline)-*b*-poly[*N*-(2,2-difluoroethyl)acrylamide] copolymer nanoparticles, *European Polymer Journal* **2019**, *121*, e109306.

Kolouchova, K.; Groborz, O.; Černochová, Z.; Gandalovicova, A.; Svec, P.; Slouf, M.; Hruby, M. Thermo- and ROS-Responsive Self-Assembled Polymer Nanoparticle Tracers for ^{19}F MRI Theranostic, submitted to *Biomacromolecules* (**9.9.2020**)

Kolouchova, K.; Jirak, D.; Groborz, O.; Sedlacek, O.; Ziolkowska, N.; Vit, M.; Sticova, E.; Galisova, A.; Svec, P.; Trousil, J.; Hajek, M.; Hruby, M. Implant-forming polymeric ^{19}F MRI tracer with tunable dissolution, *Journal of Controlled Release,* **2020**, *327*, 50-60.

Jirak, D.; Galisova, A.; **Kolouchova, K.**; Babuka, D.; Hruby, M. Fluorine polymer probes for magnetic resonance imaging: quo vadis? *Magnetic Resonance Materials in Physics, Biology and Medicine* **2019**, *32*, 173-185.

Publications not included into this thesis

Groborz, O.; Poláková, L.; **Kolouchová, K**.; Švec, P.; Loukotová, L.; Madhav Miriyala, V.; Francová, P.; Kučka, J.; Krijt, J.; Pára, P.; Báječný, M.; Heizer, T.; Pohl, R.; Czernek, J.; Šefc, L.; Beneš, J.; Štěpánek, P.; Hobza, P.; Hrubý, M. Chelating Polymers for Hereditary Haemochromatosis Treatment, in press (**2020**) in *Macromolecular Bioscience*

Švec, P.; Nový, Z.; Kučka, J.; Petřík, M.; Sedláček, O.; Kuchař, M.; Lišková, B.; Medvedíková, M.; **Kolouchová, K.;** Groborz, O.; Loukotová, L.; Konefał, R.; Hajdúch, M.; Hrubý, M. Radioiodinated choline transport-targeted diagnostics, sent to *Journal of Medicinal Chemistry* (**24.1.2020**)

Babuka, D.[*]; **Kolouchova, K.**[*]; Groborz, O.; Tosner, Z.; Zhigunov, A.; Stepanek, P.; Hruby, M. Internal Structure of Thermoresponsive Physically Crosslinked Nanogel of poly[*N*-(2-hydroxypropyl)methacrylamide]-*block*-poly[*N*-(2,2-difluoroethyl)acrylamide], Prominent ^{19}F MRI Tracer, sent to *Nanomaterials* (**25.9.2020**), *contributed equally

Contribution at conferences

Kolouchová, K.; Sedláček, O.; Babuka, D.; Groborz, O.; Švec, P.; Jirák, D.; Hrubý, M. Polymerní diagnostické a theranostické kontrastní látky pro ^{19}F MRI. *ChemZi. Roč. 15, č. 1, s. 104 (6P07) 71. Zjazd chemikov, Horný Smokovec, Vysoké Tatry, SR,* **9.-13.9.2019**; presentation.

Kolouchová, K.; Sedláček, O.; Jirák, D.; Babuka, D.; Kotek, J.; Vít, M.; Trousil, J.; Konefał, R.; Šebestová Janoušková, O.; Podhorská, B.; Šlouf, M.; Hrubý, M. Self-assembled multiresponsive polymer nanogels as contrast agents for ^{19}F magnetic resonance imaging. *POLY Graphical Abstracts. Orlando: American Chemical Society, POLY-607, 257. ACS National Meeting & Exposition, Orlando, USA,* **31.3.-4.4.2019**; presentation.

Kolouchová, K.; Sedláček, O.; Jirák, D.; Babuka, D.; Blahut, J.; Kotek, J.; Vít, M.; Trousil, J.; Konefał, R.; Šebestová Janoušková, O.; Podhorská, B.; Šlouf, M.; Hrubý, M. Self-assembled thermoresponsive polymeric nanogels for ^{19}F MR imaging. *Sborník abstraktů, Praha: Ústav makromolekulární chemie AV ČR, v. v. i., s. 39. ISBN 978-80-85009-92-7 10. Česko-Slovenská konference POLYMERY Třešť, ČR,* **2.-5.10.2018**; presentation.

Kolouchová, K.; Sedláček, O.; Babuka, D.; Kotek, J.; Jirák, D.; Hrubý, M. Thermo- and redox-responsive amphiphilic block copolymers as diagnostic and theranostic contrast agent for ^{19}F magnetic resonance imaging (MRI). *Abstract book. Bordeaux: The Laboratoire de Chimie des Polymeres Organiques (LCPO), s. 249, Bordeaux Polymer Conference, Bordeaux, Francie,* **28.-31.5.2018**; poster.

Kolouchová, K.; Sedláček, O.; Babuka, D.; Jirák, D; Kotek, J.; Hrubý, M. Thermoresponsive self-assembled block copolymers as contrast agents for non-invasive medical imaging. *ChemZi. Roč. 13, č. 1, s. 190 (6Po05) 69. Zjazd chemikov, Horný Smokovec, Vysoké Tatry, SR,* **11.-15.9.2017**; poster.

1. Introduction

1.1.   Magnetic resonance imaging (MRI)

Magnetic resonance imaging (MRI) is a commonly used noninvasive diagnostic tool in medicine and research. MRI provides high-resolution morphological/anatomical information. The first MRI (originally called nuclear magnetic resonance imaging, NMRI) was designed by Prof. Paul Lauterbur at Stony Brook University in 1971. Prof. Lauterbur published the image of an NMR tube with water in *Nature*,[1] followed by the first MR image of a mouse.[2] Later, in the 1970s, the physicists P. Mansfield and P. Lauterbur developed the first MRI-related techniques.[3]

1.1.1.   General principle of NMR and MRI

Atomic nuclei contain protons and neutrons (nucleons), each having a spin number S = ½. The total spin number of the nucleus depends on the number of nucleons in it and their type. Usually, when the numbers of protons and neutrons in the nucleus are even, the overall spin is S = 0 because the spins of the nucleons cancel each other out. In all other cases, the total spin number can be $\pm 1/2, \pm 1, \pm 3/2, \pm 2$, etc. For example, of the common observably stable isotopes, ^{4}He and ^{16}O have $S = 0$; ^{1}H, ^{13}C, ^{31}P and ^{19}F have $S = + 1/2$; ^{15}N has $S = -1/2$; ^{2}D and ^{14}N have $S = + 1$; ^{27}Al has $S = + 5/2$; ^{10}B has $S = + 3$; ^{50}V has $S = + 6$; and ^{180m}Ta has $S = -9$. The nucleus exhibits a so-called nuclear magnetic dipole moment μ according to equation (1).

$$\vec{\mu} = \gamma \vec{S} \tag{1}$$

where γ is the so-called gyromagnetic ratio, a constant specific to each nuclide. The spin number correlates with the number of energetic states of the nucleus (m): the number of energetic states is equal to 2S + 1. Without an external magnetic field, these states have equal energies. However, when the nucleus is placed in an external magnetic field, these states have different energies (Zeeman effect), given by equation (2).

$$E = -\gamma m \hbar B_O \tag{2}$$

where $\hbar$ is the reduced Planck constant. The energy gap between two states is determined by equation (3).

$$\Delta E = \gamma \hbar B_O \tag{3}$$

Overall, the application of the strong external magnetic field then results in alignment of the spin vectors along the magnetic field vector ($\vec{B_0}$), as this alignment has a lower energy.

In basic NMR techniques, nuclei are subjected to a strong external magnetic field. The alignment is subsequently disturbed *via* a strong electromagnetic pulse: the nuclei are irradiated with a radiofrequency (RF) pulse with a frequency v_{RF} close to the particular v_L of the nuclei. The energy of the pulse may cause the nuclei to "flip", meaning that they are no longer perfectly aligned with the magnetic field, rather than their spin vector being tilted at a certain angle. The flip angle grows linearly with the length of the irradiation pulse.

Afterwards, the nuclei slowly return to their original alignment along the external magnetic field. While this second alignment is occurring, a so-called spin precession can be observed with the angular frequency determined by equation (4).

$$\omega_L = -\gamma B_0 \tag{4}$$

where the angular frequency ω_L is called the Larmor frequency, $\omega_L = 2\pi v_L$, and v_L is called the Larmor precession frequency. Such a precession can then be detected with a radiofrequency coil, as it induces an electric current (so-called free induction decay, FID). The magnetic field (and therefore the Larmor frequency) is not equal in all nuclei, as the nuclei are, to some extent, shielded by the electron shell of the atom. Therefore, we can write the following formula (4'):

$$\omega_L = -\gamma(1-\sigma)B_0 \tag{4'}$$

where σ is the so-called nucleus shielding tensor; σ is highly dependent on the electron density of the given atom in the given molecule. This means that the Larmor frequency of each atom in the molecule can be slightly different depending on the shielding tensor. The detected FID is then processed *via* the Fourier transform to find the frequencies of all nuclei in the sample. As these frequencies tend to be very similar, it is very common to present these values as chemical shifts. The chemical shift (δ) can be calculated from the deviation of the measured frequency from the frequency of a so-called reference compound (set by IUPAC, *e.g.,* tetramethylsilane for ^1H NMR and ^{13}C NMR and CCl_3F for ^{19}F NMR) and is usually expressed in parts per million (ppm).

The spin relaxation processes are described with time constants T_1 and T_2 (**Figure 1**).[4] The T_1 relaxation describes the period of alignment of the spin vector with the magnetic field vector from a nonequilibrium state. The relaxation transverse to the static magnetic field is called T_2 relaxation, which corresponds to an exponential decay of the observable signal. These relaxation processes are relatively independent due to their different relaxation mechanisms. T_1 relaxation corresponds to the redistribution of the spins to reach thermal equilibrium and involves the interactions with the surroundings, *i.e.*, the lattice (spin-lattice relaxation). T_2 relaxation involves the loss of coherence of the nuclear spins after excitation, resp. the decoherence of the spin magnetization, which involves only the interactions between the spins (spin-spin relaxation).
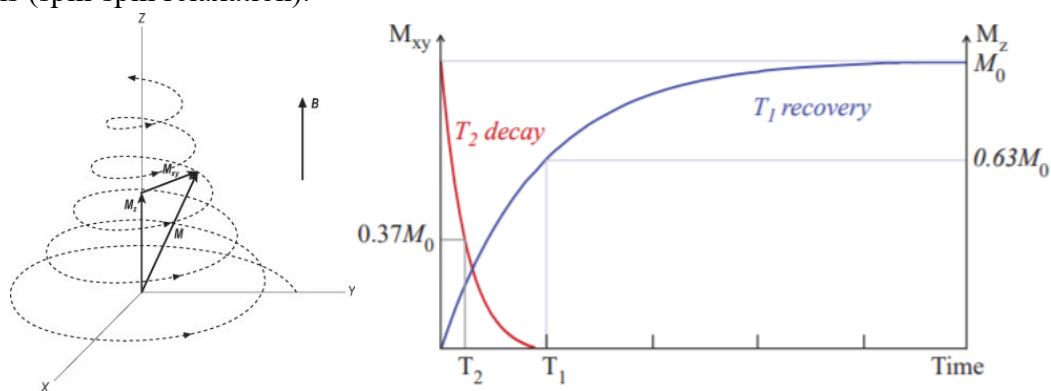
Figure 1. Schematic diagram of the spin relaxation from the Y-axis after a 90° pulse (right)[5] in T_1 and T_2 relaxation.[4] T_1 relaxation is in the direction of the external magnetic field, the direction of the Z-axis; therefore, the signal grows exponentially. T_2 relaxation is transverse to the induced magnetic field (in the xy-plane), and therefore, the signal decays exponentially.

However, unlike in an ideal system where all nuclei relax with the same frequency, in a real system, there are small differences arising from the anisotropy of the environment surrounding the nuclei. The recoherence caused by the inhomogeneities in the magnetic field cannot be considered as a part of the relaxation process. Therefore, the corresponding T_2^* is usually smaller and is described by equation (5).

$$\frac{1}{T_2^*} = \frac{1}{T_2} + \frac{1}{T_{inhomog.}} = \frac{1}{T_2} + \gamma \Delta B_0 \tag{5}$$

As a result of these inhomogeneities (especially relevant in *in vivo* MRI), T_2^* describes the decrease in the FID after the initial pulse. To detect the signal again, the so-called spin echo (180° pulse) can be applied to refocus the signal. The decay of the overall detectable signal follows the T_2 relaxation, as shown in **Figure 2**.
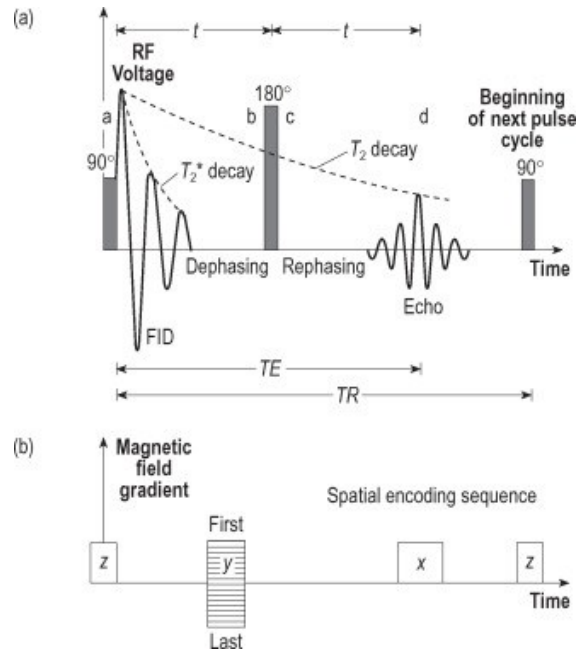
Figure 2. Scheme of one cycle of the spin-echo sequence (a) and application of magnetic field gradient switching to obtain the MR image (b). Reproduced from Allisy-Roberts and Williams.[5]

When studying biological systems, an MR spectrum (MRS) can be collected, which is analogous to the NMR spectrum. The information that it can provide is very limited, as the peaks are very broad due to local inhomogeneities of the field.

To obtain an image of the signal, we apply so-called magnetic field gradients, represented in **Figure 2**. When the magnetic field changes throughout the sample or the patient, the nuclei are exposed to different magnetic fields and consequently have different Larmor frequencies. This allows us to encode the depth (width or length) of an image into a chemical shift within the acquired spectrum. In medicine, ^1H hydrogen nuclei are used most often because hydrogen atoms are very abundant in living organisms, as they are present particularly in water, fat, and carbohydrates, and they have a very high gyromagnetic ratio.

The MRI instrument is composed of the main magnet, the shim coils for correcting the inhomogeneities of the main magnetic field, the RF coil, which excites the sample and detects the signal, and the gradient system, which enables image acquisition. The whole

system is controlled by a computer able to reconstruct the acquired images into a 3D MR image. The strength of the magnetic field for the commonly available instruments ranges from 0.2 to 7 T (mostly operating at 1.5 T). The MRI measurement process involves a so-called RF sequence, containing several radiofrequency pulses and gradients that result in a set of images. The adjustments of the RF sequences are based on the T_1 and T_2 relaxation constants. Based on T_1 and T_2, we can change two parameters based on the relaxation times (**Figure 2**): the repetition time (TR), *i.e.*, the time between excitation pulses, and the echo time (TE), *i.e.*, the detection time between the sequences. By setting the TR longer than the T_1 relaxation time, we can allow the atom magnetization to fully recover and obtain the so-called T_1-weighted image, which is useful for obtaining information on anatomy, fatty tissue, melanin, slowly flowing blood, *etc*. To obtain the so-called T_2-weighted image, we set the TE to let the magnetization decay fully before detecting the signal, with which we can detect tissues with higher water content, such as edema, inflammation, tumors or pathologies in general. The final image plotted is usually black and white, allowing us to distinguish between high signal (white) tissue (as mentioned above) and low signal tissue (black), which is tissue with less fat or water depending on the setting (bone, air, urine, etc.).[6] A comparison of T_1-weighted and T_2-weighted images can be seen in **Figure 3**, representing the possible use of MRI for the detection of focal cortical dysplasia, a congenital abnormality of the brain and common cause of epilepsy (red arrow).[7]
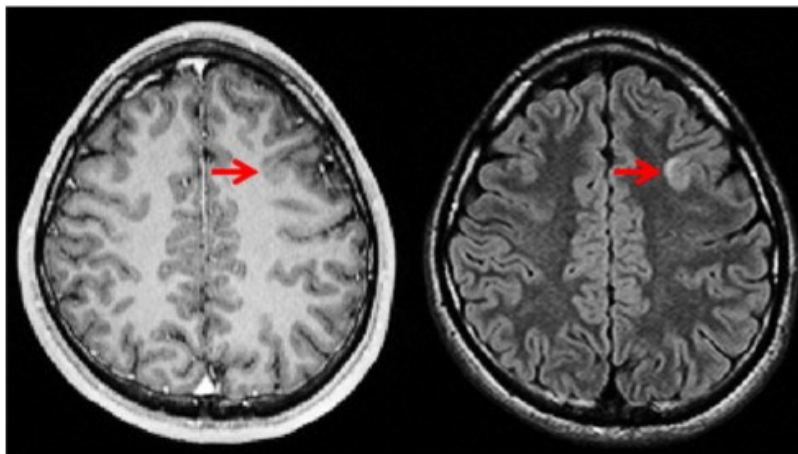
Figure 3. T_1-weighted (left) and T_2-weighted (right) axial MRI images taken from a 21-year-old male epilepsy patient. The red arrow indicates the focal cortical dysplasia as a loss of gray-white contrast in T_1-weighted imaging as well as hyperintensity in T_2-weighted imaging.[7]

In conclusion, parameter setting in MRI diagnosis is very important. The main advantage of the MRI technique is that it does not expose the patient to any ionizing radiation and can noninvasively visualize even relatively minor pathologies in soft tissues rather well. Its main disadvantage of this technique, except of its price, is its relatively low sensitivity, causing longer measuring times than in, *e.g.*, computed tomography. **Figure 4** shows an example of how the TR and TE settings can affect the intensity of the MRI signal (in this case, the ^{19}F signal).[8] A short TR (left) is based on T_1 because we do not allow the atom magnetization to fully recover, which is the abovementioned principle of T_1-weighted imaging. The TE setting is dependent on the T_2 relaxation time. If the TE is too long, then the atom magnetization decays

before we start to detect the signal. In some cases, this can lead to complete disappearance of the signal (contrast agents with too short T_2, discussed in more detail in the following Chapter).
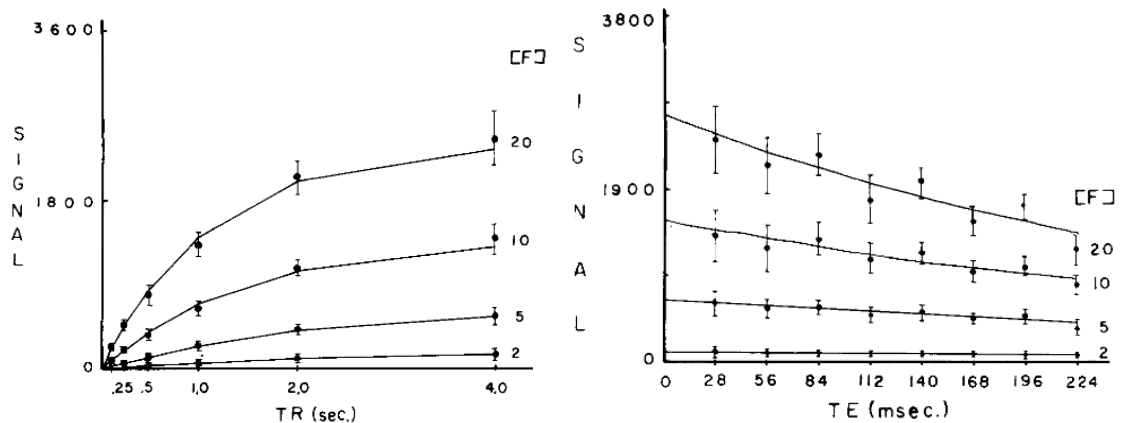
Figure 4. Signal strength plotted as a function of TR (left) or TE (right) for several concentrations of fluorine-19 contained in a tracer (20 M to 2 M).[8]

1.1.2. Contrast agents (CAs) for MRI

Differentiating between healthy tissue and pathology is not always feasible, especially in the early stages of the disease (amyloid plaques, a cause of Alzheimer's disease[9], tumors and other pathologies) when the contrast is low, *i.e.*, the difference between the relaxation times of the protons in different tissues is insufficient.[10] This issue can be solved by using contrast agents (CAs). The most common CAs contain paramagnetic species (mostly Gd[III]) that accelerate spin relaxation of surrounding water protons (T_1-contrast agents),[11,12,13] superparamagnetic iron oxide nanoparticles (SPIONs), serving as T_2-contrast agents,[14,15] or even a combination of both systems.[16]
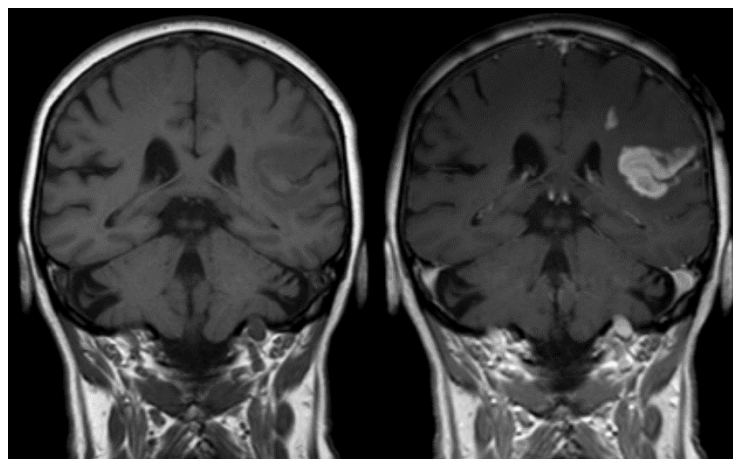
Figure 5. T_1-weighted images; left image without and right image with Gd(III)-based contrast medium administration showing a defect of the blood–brain barrier after stroke. Reproduced from wikimedia.org (http://creativecommons.org/licenses/by-sa/3.0/).[17]

CAs can be administered intravenously or orally, and they have various biodistribution pathways. CAs injected intravenously and biodistributed passively in the bloodstream, also known as "extracellular fluid agents", are commonly used in medicine for several applications, such as arterial or venous mapping and detection of internal bleeding or endovascular leakage

(gadodiamide, gadopentetic acid, gadoteric acid, *etc.*; see **Figure 5**). Moreover, to prolong the circulation of a contrast agent in the blood stream, contrast agents can also be designed to bind to a carrier such as albumin or a polymer; these carriers are so-called blood pool agents.[18] CAs can be targeted to an organ, a specific pathology or a tumor and thus accompany smart drug delivery systems or stimuli-responsive polymers.[19–23]

Despite the higher contrast provided, the commonly used paramagnetic CAs are based on toxic heavy metal ions (typically gadolinium), with poor biodistribution; therefore, only the lack of alternatives has ensured that their clinical interest is maintained.

1.1.3. Fluorine-19 MRI
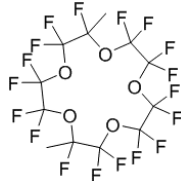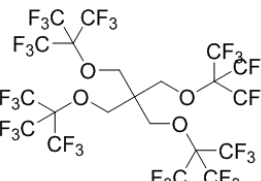
An interesting approach to widen the use of MRI in medicine is the detection of nuclei other than protons for imaging purposes. ^{19}F is possibly the most prominent non-^{1}H nucleus for MRI purposes. An important benefit of ^{19}F MRI over other non-^{1}H MRI variants is the characteristically high ^{19}F MR sensitivity (83 % sensitivity compared to that of ^{1}H MR) and the possibility to measure ^{19}F in commonly used ^{1}H MRI devices (^{19}F and ^{1}H have similar gyromagnetic ratios) in the so-called multimodal imaging (**Figure 1** shows an example of ^{1}H and ^{19}F imaging of a polymeric tracer *in vivo*). In contrast to the ubiquitous presence of ^{1}H in living organisms, the bodily concentration of ^{19}F nuclei is negligible. Therefore, unlike ^{1}H MRI, this imaging requires the administration of a tracer. The lack of bodily ^{19}F, on the other hand, increases the specificity of the signal detection, as there is virtually no background signal. Fluorinated compounds started to be tested as a possible MRI tracer shortly after the first proton MRI in the 1970s. The first image was obtained in 1977, with NaF and perfluorotributylamine as representatives of the first MRI tracers. Nevertheless, the research on ^{19}F MRI, despite its benefits, was somewhat slower than the scientific boom in the ^{1}H MRI field. Currently, many fluorinated compounds (PFCs) that have been found to be nontoxic and chemically inert are being used in various medical applications.[24,25,26,27] The benefits of using fluorine-19 as a tracer are as follows:

1) As already mentioned, the background is marginal: the natural fluorine concentration in the body is very low, usually below the MRI sensitivity.
2) The natural abundance of the ^{19}F isotope is 100 %; therefore, no enrichment is required.
3) The MR sensitivity is very high (83 % sensitivity of ^{1}H).
4) The gyromagnetic ratio of ^{19}F is very high (94 % of the gyromagnetic ratio of the ^{1}H nuclide). This means that it is possible to adjust a commonly used imaging device for ^{19}F MRI instead of for ^{1}H MR, and the RF coils for ^{19}F MRI may be initially constructed to be dual-tuned for both ^{1}H and ^{19}F MRI.
5) ^{19}F MRI tracers are an alternative to T_1 and T_2 contrast agents for ^{1}H MRI.
6) Fluorinated molecules can have an extraordinarily large chemical shift range (from nearly –600 ppm to +600 ppm). Therefore, it is even possible to administer and monitor several ^{19}F MRI tracers simultaneously.
7) Fluorinated compounds can be made chemically inert and biocompatible.

Fluorinated molecules were used for many applications in medicine due to their biocompatibility; therefore, they have also been studied in ^{19}F MRI research.[28] The fluorinated compounds used in ^{19}F MRI applications are specifically regarded as 'tracers' or 'probes', sometimes even incorrectly as 'contrast agents'. Choosing the term 'probe', which is also used for the detection device, often leads to a confusing description of the system. For the purpose

of this thesis, all the systems described for the ^{19}F MRI application will be addressed as 'tracers'. The most common tracers are PFCs. The main benefit of using PFCs as ^{19}F MRI tracers is the high concentration of fluorine atoms (as high as 60-70 %).[29] For a long time, perfluorinated hydrocarbons were the most commonly used ^{19}F MRI tracers in research and medicine (perfluorooctyl bromide was approved by the food and drug administration agency, FDA, over 25 years ago, in 1993[30]). Although these materials tend to have high concentrations of fluorine atoms per mass (as high as 70 %), their application is limited. The abovementioned perfluorooctyl bromide has negligible biological availability and therefore is used only for gastrointestinal tract (GIT) "virtual colonoscopy" with no radiation exposure of the patient. If administered intravenously, PFCs often accumulate in the organism due to the withdrawing of them by the reticuloendothelial system, such as in lymph nodes, liver, spleen and bones.[31] Besides this particular application, the use of PFCs is very limited. Furthermore, most PFCs provide multiple ^{19}F MR signals, which is a severe disadvantage for ^{19}F MRI purposes because the simultaneous detection of multiple signals for MRI is very problematic (but not impossible). The most common low-molecular-weight PFC tracers can be seen in **Table 1**, along with the fluorine content and reference.

Table 1. Summary of developed ^{19}F MRI low-molecular PFC tracers.[29]

Systematic name	Abbrev.	Structure	M_w (g mol^{-1})	Fluorine atoms % wt.	Ref.
Perfluoro-15-crown-5-ether	PFCE		579.9	65.5	32–35
Perfluorooctyl bromide	PFOB		497.9	64.7	36
1,3-Bis[[1,1,1,3,3,3-hexafluoro-2-(trifluoromethyl)propan-2-yl]oxy]-2,2-bis[[1,1,1,3,3,3-hexafluoro-2-(trifluoromethyl)propan-2-yl]oxymethyl]propane	PERFECTA		1008.0	67.8	37

To design a ^{19}F MRI tracer, the right balance between a high concentration of fluorine (sensitive enough to be detectable in a scalable concentration) and the hydrophobicity of the molecule has to be found for every system. For routinely used MRI scanning techniques (*e.g.*, rapid acquisition with relaxation enhancement sequence, RARE), T_2 should be longer than 10 ms.[29] Short T_2 relaxation requires the use of particular sequences, such as ultrashort echo time (UTE) or zero echo time (ZTE) sequences,[38] which are very hardware demanding. **Figure 6** summarizes the dependences of T_1 and T_2 on the viscosity and molecular weight, where with growing viscosity of the molecule, T_1 increases and T_2 rapidly decreases.
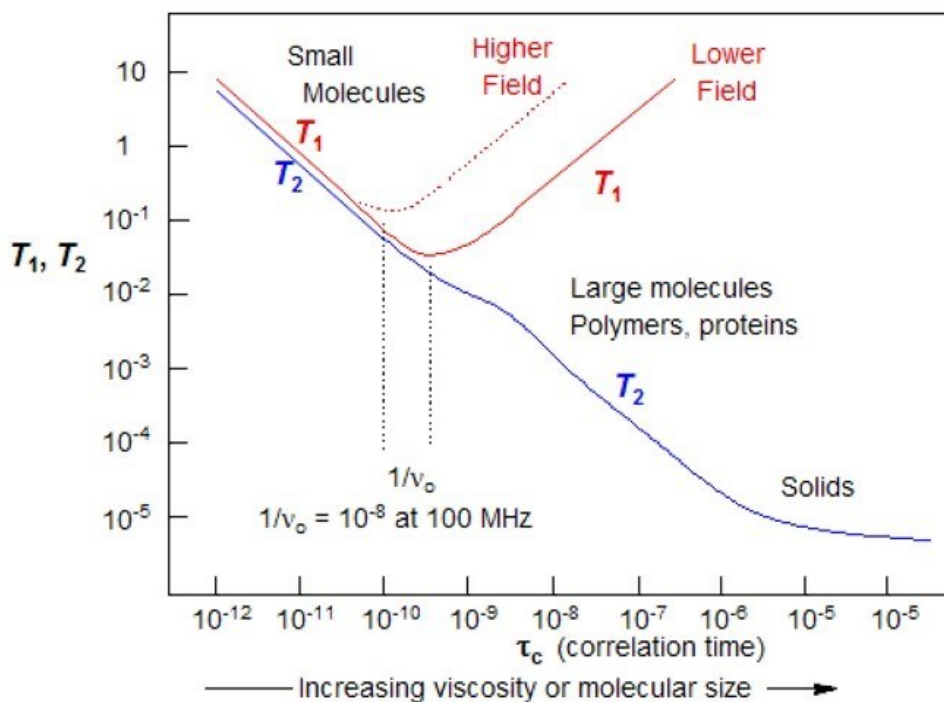
Figure 6. T_1 and T_2 as a function of correlation time for spin ½ nuclei relaxing by the dipole-dipole mechanism. τ = molecular correlation time: the time it takes the average molecule to rotate one radian.[39]

In conclusion, the hydrophobicity of the PFCs with increasing number of fluorine atoms can lead to a significant loss of applicability. This phenomenon was described in a very thorough review, presenting recent advances in amyloid imaging using ^{19}F MRI.[9] The formation of senile plaques followed by the deposition of neurotoxic amyloid-β is the earliest stage of Alzheimer's disease (AD). Amyloid-β (Aβ) plaques occur even 20 years before the clinical onset of AD; therefore, it is very important to develop effective imaging of even a marginal pathology for early diagnosis.[40] Tracers for use in amyloid imaging must be able to cross the blood brain barrier and bind to Aβ plaques at high concentration to display a high signal intensity and must be biocompatible. It has been reported that ^{19}F NMR signals are very sensitive to the tissue environment. The first example can be seen in **Figure 7**. [19]F MRI probes (A, D) with different polarities (different log$P$ values) were injected into muscle and brain. Then, 1 h after administration, ^{19}F MRI was performed. As shown in images C and F, the ^{19}F MR signal of one of the tracers (TFMB-2Et) was observed only in the muscle (left image, arrow) and not in the brain. In comparison, ^{19}F MR images of the more polar derivative (lower log$P$) (TFMB-3Et) were observed in both the muscle and brain (right image, arrows). The reason why the signal in the brain of the more lipophilic tracer disappeared was the inhibition of the ^{19}F signal (loss of mobility, described above) due to interaction of the fluorine atoms with lipids (myelin) in the brain.
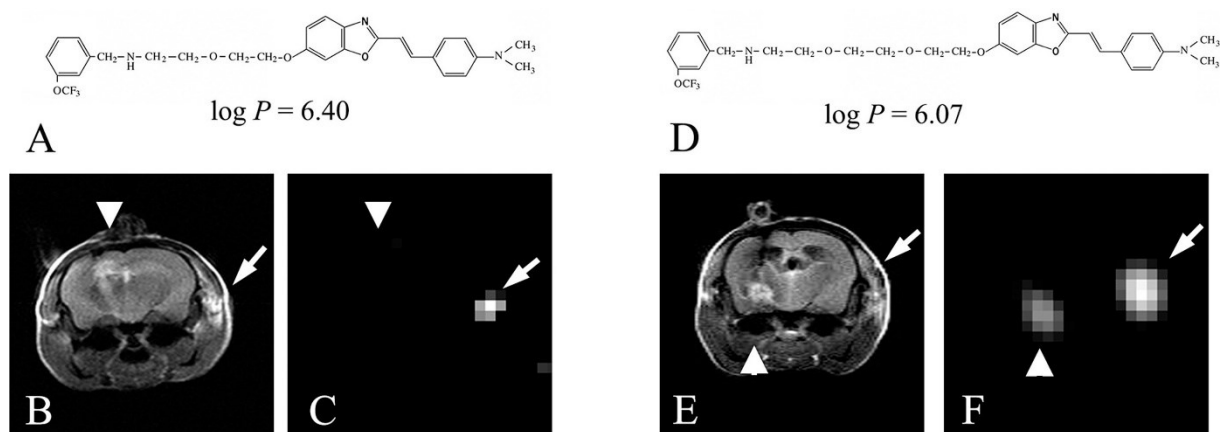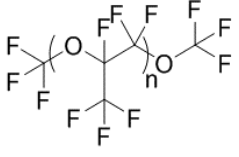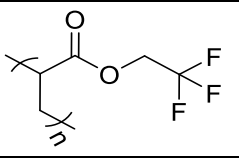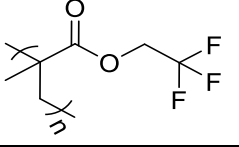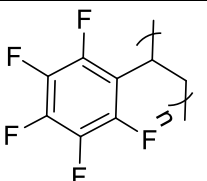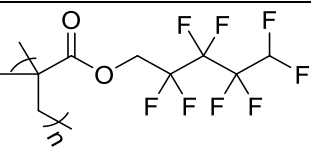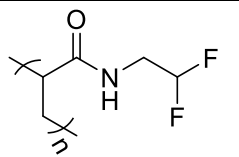
Figure 7. Structures of TFMB-2Et (A) and TFMB-3Et (D), the ^{1}H gradient echo (B, E) and ^{19}F MR images (C, F). The left arrow is pointing to the area where the brain is located, and the right arrow is pointing to the muscle (images B, C, E, F).[40]

To avoid signal loss, the authors decided to use short poly(ethylene glycol) (PEG) oligomers (3 - 7 units have been found to be optimal) as a carrier for the fluorinated group. The short PEG with the fluorinated group at the end can decrease the lipophilicity of the tracer and increase the mobility of the fluorine atoms. Different fluorinated groups were introduced for ^{19}F MRI: the trifluoroethoxy (3 fluorine atoms), hexafluoroisopropoxy (6 fluorine atoms) and 3′,5′-bis(trifluoromethyl)benzylamino (6 fluorine atoms) groups. Afterwards, an *in vitro* study was performed, showing as anticipated that increasing the number of fluorine atoms results in a higher intensity of the signals. However, an *in vivo* study revealed that the trifluoroethoxy group, with the lowest number of fluorine atoms, shows the highest signal intensity, probably due to the higher mobility of the atoms. This review described that increasing the amount of fluorine is not always a straightforward way to obtain a strong ^{19}F MRI signal.

How can we obtain the key property needed for fluorine probes, as high a fraction of chemically equivalent ^{19}F atoms in the molecule as possible, while avoiding a poor biodistribution of the tracer or signal loss due to the low mobility of the fluorine atoms? These demands can be met, *e.g.*, by designing probes based on polymer structures. Polymeric probes enable the incorporation of a large amount of chemically equivalent fluorine atoms into a single molecule and thus can overcome the sensitivity issue of ^{19}F MRI. Moreover, polymer probes can be easily modified to increase their biodistribution and respond to the environment in living systems (pH responsive or thermoresponsive domains or bonds that may be enzymatically degraded) or to add imaging labels to drug moieties. **Table 2** outlines some examples of developed perfluorinated macromolecular ^{19}F MRI tracers. In general, polymeric ^{19}F MRI tracers have many possible applications for special therapies and imaging, while they can be modified to exhibit additional properties and a targeting function (**Chapter 1.3**). Most of the polymeric tracers are designed to create supramolecular structures (particles and polymeric implants). These supramolecular structures can form a drug delivery system, be used for cell labeling and sustained drug release or be targeted to diagnosis of pathology, *e.g.*, venous thrombosis, aortic valve disease, atherosclerosis, or tumors.[24,27,33–35,41–54,]

Table 2. Summary of developed ^{19}F MRI macromolecular tracers, including the reference.[29]

Systematic name	Abbrev.	Structure	M_w^* (g mol^{-1})	Fluorine atoms % wt.	Ref.
Perfluoropolyethers	PFPE		320.0	71.2	55–59
Poly[O-(2,2,2-trifluoroethyl)acrylate]	PTFEA		154.0	37.0	60–62
Poly[O-(2,2,2-trifluoroethyl) methacrylate]	PTFEMA		168.0	33.9	60–62
Poly(2,3,4,5,6-pentafluorostyrene)	PPFS		194.0	48.9	63
Poly[O-2,2,3,3,4,4,5,5-octafluoropentyl methacrylate)]	POFPMA		300.0	50.6	63
Poly[N-(2,2-difluoroethyl) acrylamide]	PDFEA		135.0	28.1	29,64,65,66

*Per monomer unit

However, the preparation of such supramolecular systems results in a change in the solvation of the rather lipophilic polymers described in **Table 2** as well as the relaxation properties of the tracer. The change in solvation and decrease in mobility of the polymer chains lead to loss of the ^{19}F signal intensity in the same manner as described above with low-molecular-weight tracers. Moreover, many of the polymers described in **Table 2** (PFPE, PPFS, and POFPMA) contain chemically nonequivalent atoms of fluorine, scattering the ^{19}F signal into several peaks. As described earlier, MRI provides imaging only from a narrow range of chemical shifts. In other words, more than one signal of fluorine due to chemically nonequivalent fluorine nuclei is detrimental, as it only increases the unfavorable hydrophobicity.

In this thesis, we describe our ^{19}F MRI tracer systems based on the N-(2,2-difluoroethyl)acrylamide monomer. Poly[N-(2,2-difluoroethyl)acrylamide] (PDFEA) is a thermoresponsive polymer containing a high concentration of magnetically equivalent fluorine atoms, providing one signal in ^{19}F MRI. This polymer exhibits the so-called lower critical solution temperature (LCST) in water, which means that it can be injected into

the body at room temperature as an aqueous solution. Upon heating to body temperature, the polymer rapidly loses its hydration layer, forming aggregates and insoluble depots at the site of injection (described in more detail in the following Chapter). Upon temperature change-induced self-assembly into supramolecular structures, it loses the solvation and mobility as well; nevertheless, the supramolecular structures based on PDFEA still show advantageous T_1 and T_2 relaxation properties. According to T_1 and T_2, the solvation of the fluorine atoms within the self-assembled supramolecular structures is more than sufficient for ^{19}F MRI. The concentration of fluorine is the lowest compared with the other systems; however, it was already proven that for MRI purposes, a lower fluorine concentration can result in a higher signal intensity. It is difficult to compare developed tracers, considering that most scientific papers provide only *in vitro* (MRS or so-called MRI phantoms) or direct *in vivo* data. Only images obtained with the same techniques, concentration and time can be compared; otherwise, the information will be incorrect. The best information about the system is probably the relaxation properties, ideally under physiological conditions (PBS buffer, pH 7.4, 37 °C). Unfortunately, when comparing relaxation properties, several parameters can also produce different results, such as the ionic strength of the used buffer or the magnetic field. Last but not least, the setup of sequences to obtain relaxation properties is not simple, but it can be an asset in several ways. In conclusion, it is difficult to compare the systems across the wide spectrum of developed tracers. However, the T_1 and T_2 relaxation properties and the signal intensity in the physiological environment of each system can be considered to provide sufficient information on the tracer suitability for ^{19}F MRI.

1.2. Lower critical solution temperature (LCST) – stimuli-responsive polymers

1.2.1. Thermoresponsive polymers

The theory of the thermoresponsive behavior of polymers began in the 1940s with Flory and Huggins. The theory describes that a polymer in solution has an expanded coil conformation, and upon increasing the temperature, it can collapse into compact globules. In a simplified way, the process can be described with the Gibbs free energy equation (6). The expanded coil is solvated along the chain with the solvent molecules, resulting in a negative change in the enthalpy of mixing contribution ($\Delta H_{\mathrm{mix}} < 0$, enthalpy-driven process). However, the solvated polymer chains possess an unfavorable negative entropy contribution ($\Delta S_{\mathrm{mix}} < 0$, the entropy of mixing), which increases with increasing temperature ($-T\Delta S_{\mathrm{mix}}$ increases), resulting in a positive Gibbs free energy ($\Delta G_{\mathrm{mix}} > 0$) and consequent phase separation.

$$\Delta G_{\mathrm{mix}} = \Delta H_{\mathrm{mix}} - T\Delta S_{\mathrm{mix}} \qquad (6)$$

The temperature at which the macroscopic phase separation is observed is regarded as the cloud point temperature (T_{CP}), named for the cloudiness of the solution due to the formation of larger particles and precipitates above this temperature. T_{CP} is dependent on the polymer concentration. To fully describe the thermoresponsive behavior of a particular polymer, we can determine the so-called lowest critical solution temperature (LCST), corresponding to the lowest possible T_{CP} in the phase transition diagram (**Figure 8**). The presented experimental phase diagram (**Figure 8,** right) corresponds

to the thermoresponsive polymer poly(*N*-isopropyl acrylamide) (PNIPAm) in water. An LCST of ~ 32 °C was determined for PNIPAm in the 1960s by M. Heskins and J. E. Guillet.[67]
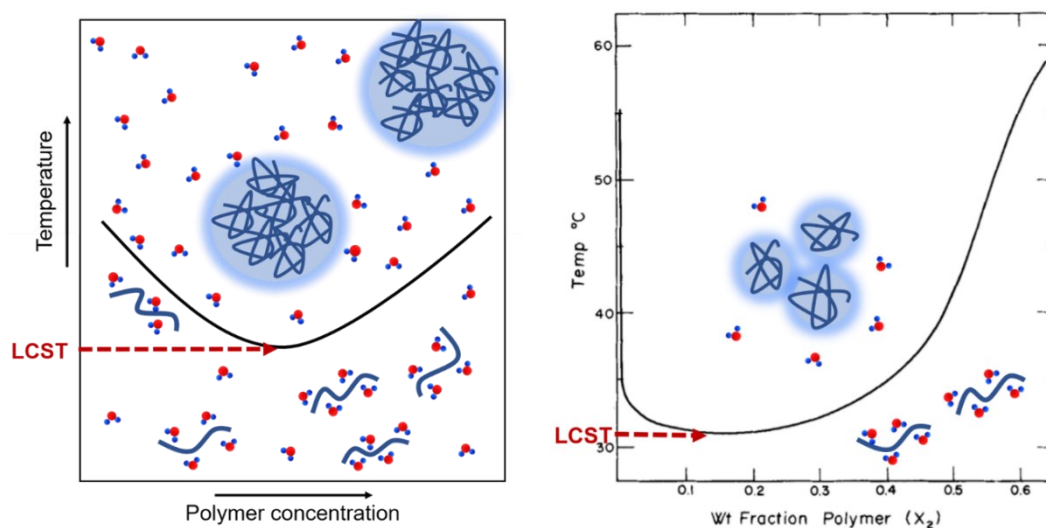
Figure 8. Theoretical scheme of the phase transition diagram of a polymer solution (left), and experimental phase transition diagram of the PNIPAm aqueous system (adapted from reference[67]). The polymer solvated by water molecules precipitates into clusters above the transition curve.

The LCST is sensitive to environmental changes and can be affected by the ionic strength of the solution, the pH or the interaction with salts or proteins. The LCST can also vary with the polymer length, especially for relatively short polymers.[68] Determination of the LCST requires a relatively large amount of polymer and is very time consuming. Therefore, the T_{CP} measured under carefully chosen conditions usually provides sufficient information about the polymer. Ideally, T_{CP} is measured at relevant polymer concentrations in a physiological buffer (*e.g.*, 150 mM PBS) to simulate biological conditions. **Figure 9** shows examples of thermoresponsive poly(*N*-alkyl acryl/methacrylamides) and poly(2-alkyl-2-oxazoline)s along with their particular LCSTs.[69–71]
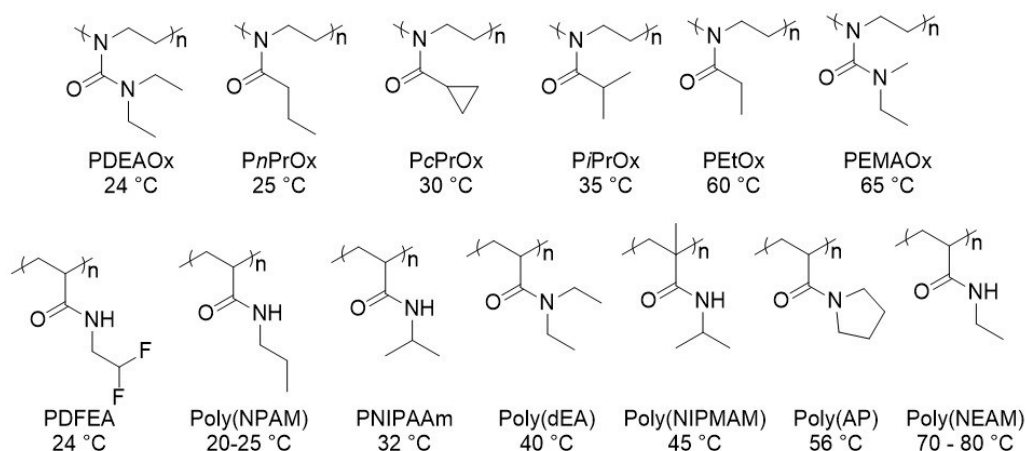
Figure 9. Examples of a range of thermoresponsive polymers and their approximate LCST values.

1.2.2. Tuning the LCST and designing supramolecular polymer architectures

Pure thermoresponsive polymers form rather undefined clusters above their T_{CP}. These clusters can be particles (usually with broad polydispersity), macroscopic precipitates, or gels, depending on the polymer concentration, length and type. In biomedical applications, thermoresponsive polymers are usually utilized as a component of more complex smart systems.[68–73] The architecture of such systems then determines the morphology of the self-assembly as well as the polymer LCST behavior.

The most common example of controlled self-assembly involves amphiphilic block copolymers, containing two distinct blocks of a thermoresponsive polymer and a hydrophilic polymer. Depending on the architecture, these copolymers can create uniform particles such as micelles, vesicles or polymersomes, worm-like (cylindrical) micelles, and physically crosslinked nanogels,[64,65] among others.[74–76] The method for predicting the final morphology of the nanoparticles depending on the blocks ratio and length and can be seen in **Figure 10**, which is based on the so-called packing parameter, *p*, defined by the equation in **Figure 10**. However, the predictions can be applied only for simple block copolymer architectures (usually based on PEG), while there is a wide and diverse range of architectures of block copolymers with different morphologies and medicinal applications. Overall, particles can be used for drug formulation due to the core capable of encapsulating hydrophobic (micelles) as well as hydrophilic (vesicles, nanogels) drugs.
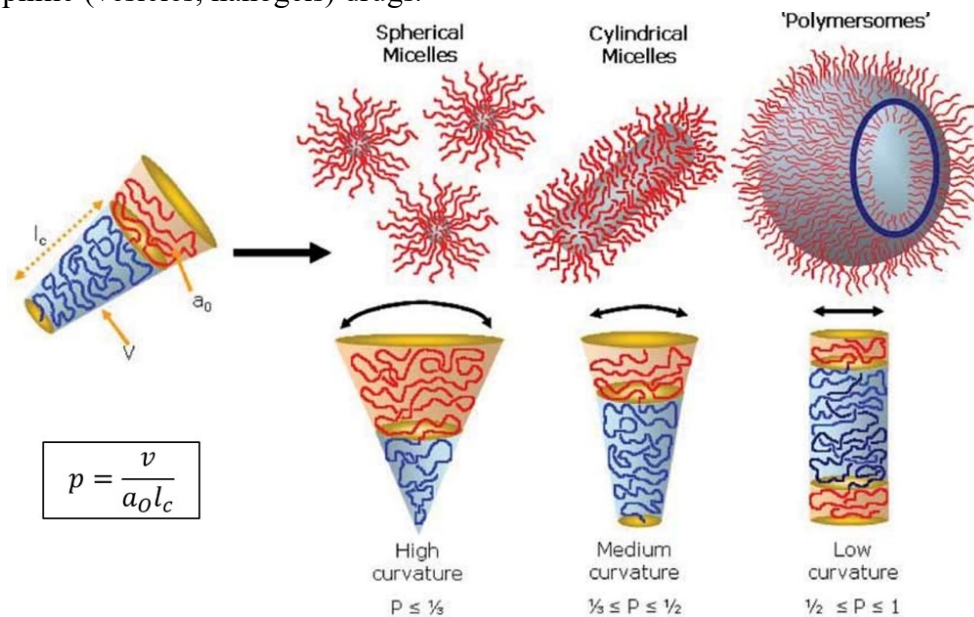
Figure 10. Various self-assembled structures formed by amphiphilic block copolymers in water (the red polymer corresponds to the hydrophilic block and the blue to the hydrophobic block). The morphology of the self-assembled particle is estimated based on the packing parameter *p*, where *v* is the volume of the hydrophobic chains, a_o is the optimal area of the head group, and l_c is the length of the hydrophobic tail. Figure adapted from reference[76].

Another way of using thermoresponsive polymers is as hydrogels or polymeric implants. The hydrogel or solid polymeric implant can simply be prepared *in situ* by heating a polymer in aqueous solution or a polymer coated on a specific surface, without any other requirements for chemical or environmental treatment. Therefore, they can be used in several biomedical applications, such as sustained drug release (DR), tissue engineering, and cell cultivation.[77,78]

1.2.3. Multiresponsive polymers

Modern medicine depends heavily on the use of pharmaceuticals. Most of them, however, suffer from more or less severe side effects that might limit their use or the comfort and compliance of the patient. Organ-specific side effects can be limited by administering the drug in a way that limits off-target organ exposure to the drug. The so-called drug delivery systems (DDSs) are of major importance to improve the bioavailability and pharmacokinetics of pharmaceuticals.[79] Tissue-specific drug delivery systems are designed to use one or several specific properties of the target tissue that, ideally, cannot be found anywhere else in the body than at the target site.[80–82] One of the oldest known and possibly the most studied polymer targeting approaches is the so-called enhanced permeability and retention (EPR) effect.[83,84] It is known that the majority of solid tumors take up nanoparticles of a certain size more than healthy tissues do. Moreover, due to the common lack of lymphatic drainage in solid tumors, these nanoparticles are very poorly cleared away; therefore, they are virtually trapped in the tumor (**Figure 11**). Hence, if a pharmaceutical-containing nanoparticle is administered into the bloodstream, its accumulation in the malignancy might increase.
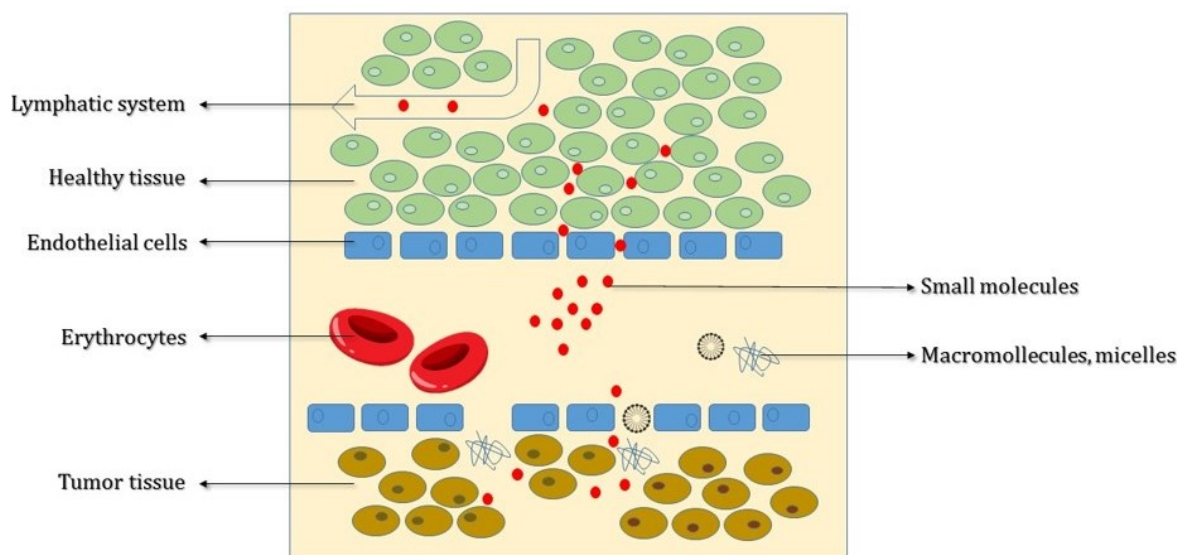
Figure 11. Illustration of the enhanced permeability and retention (EPR) effect of macromolecular structures as drug delivery systems in malignant tissue.

To obtain a DDs capable of releasing the drug into the target tissue, we have to modify the polymer-based carrier with a molecule sensitive to certain changes in the environment. The general idea is to disrupt the ability of the carrier to form a supramolecular structure in certain conditions. There are several ways to achieve this disassembly by increasing the polymer solubility in water, *e.g.*, *via* the design of a pH- or a reactive oxygen species (ROS)-responsive system,[85,86,95–101,87–94] *via* a change in the molecule conformation, or by using host-guest interactions (*e.g.*, light- or enzyme-responsive systems).[96,98,99,102,103]

For a stimuli-responsive system, its LCST may increase above the physiological temperature after changes in the environment, making the polymer soluble in water and promoting drug-carrier disassembly. An example of such a system is a thermo- and pH-responsive polymer based on a PDFEA statistical copolymer with two different monomers (**Figure 12**).

One of them is hydrophilic and contains a hydroxyl moiety. The hydrophilic monomer is used to adjust the transition temperature ($T_{CP} \approx 24$ °C, higher than that of pure PDFEA) to improve the polymer biodistribution (see **Chapter 1.4**). The second monomer contains the pH-responsive imidazole molecule, which is protonated in slightly acidic conditions (the pK_A of the conjugated acid of imidazole is 6.95[104]). The protonation of the imidazole moiety increases the solubility of the polymer in water, leading to a significant change in the polymer transition temperature ($T_{CP} \approx 65$ °C at pH = 5.0). In conclusion, the LCST varies as a function of the pH of the surrounding solution. The values of T_{CP} in **Figure 12** were measured using turbidimetry (**Chapter 1.5.7.**).
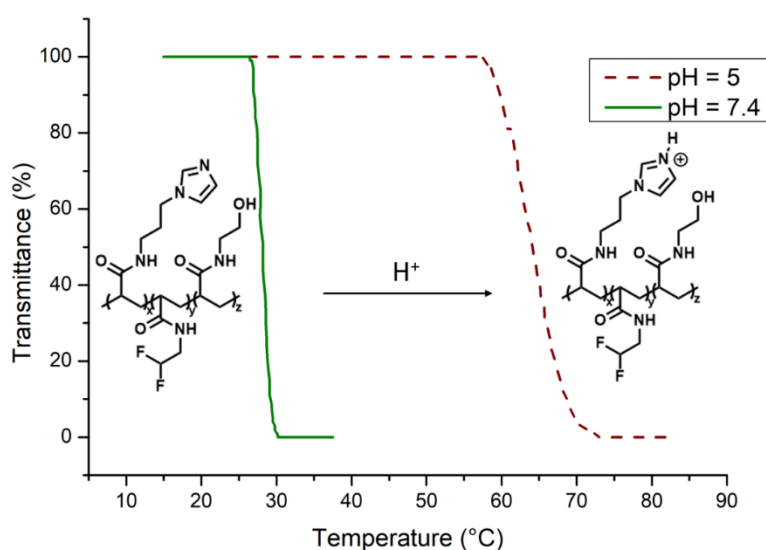
Figure 12. Transmittance ($\lambda = 600$ m) of the polymer solution (polymer F1, $c_{pol} = 5.0$ mg·mL^{-1}) as a function of temperature at pH 7.4 (continuous green curve) or 5 (discontinuous red curve). Adapted from reference[105].

In conclusion, the described copolymer can be used as an injectable depot for targeted release of loaded drugs at the site of injection. The main advantage of such a system is that the polymer can be dissolved in a slightly acidic aqueous solution and injected into the body without the possibility of the polymer solidifying and thus obstructing the needle, which is a common issue with thermoresponsive polymers. To avoid this problem, thermoresponsive polymers are commonly administered as solutions in dimethylsulfoxid (DMSO), which can cause undesirable side effects. The slightly acidic aqueous solution undergoes quick neutralization and therefore enables the quick formation of a solidified depot.

Furthermore, if the pH in a certain tissue is lowered for some reason (*e.g.*, tumor tissues have lower pH due to the so-called Warburg effect), the solidified polymeric implant would dissolve quicker (or not solidify at all) and release the co-administered compound quickly (under acidic conditions, the LCST is higher than the body temperature), while nonpathological tissues would be exposed to much lower concentrations of the drug (for a longer period of time).[106]

1.3. Theranostic

The term 'theranostic' was coined in 2002 by J. Funkhouser,[107] and it represents the idea of combining a therapy with diagnostic imaging. This approach was later adopted by many pharmaceutical companies, who believed that combining a therapy with a diagnostic tool can accelerate drug development and testing, reduce the side effects of drugs, and improve the treatment in general. Theranostic systems are mostly based on the same principle as drug carriers, the DDs, which means that they improve the pharmacokinetics and biodistribution of the drug while also carrying a kind of imaging modality. The diagnostic tool is primarily used for tracking the drug carrier to investigate the system and its biodistribution. If the system reaches its target, then it can be used for diagnosis of the pathology as well as for monitoring the response to the treatment.[108–112] The optimal drug carrier is usually a nanosized particle able to target a specific location and to encapsulate the drug with a high loading capacity due to its relatively large core. Nanoparticles are also used to reduce the fast clearance from the organism through the kidneys, which is dependent on the particle size and the functionalization present on the surface. In the past two decades, many so-called "smart theranostic systems" have been developed, combining therapeutic strategies, such as chemotherapy, photo- and photothermal therapy, radiotherapy, immunotherapy or nucleic acid delivery, with various imaging methods using contrast agents (MRI), tracers for nuclear imaging (PET/SPECT), fluorescence markers and quantum dots or tracers for ^{19}F MRI.

To prepare a theranostic material, we can follow two basic approaches. The first is simple modification of the studied DDs, which can target and contain any therapeutic modality (encapsulated or chemically bound drug), with the imaging unit, such as a tracer molecule, a fluorescence dye or a contrast agent. This approach can be described as a building kit, where we connect several units to form a multimodal smart system with all parts being tailored for their specific intended partial tasks.

The second approach is to use a material that already combines all the mentioned properties together, making the whole system much less complicated and more feasible to prepare. The simplest example is a therapeutic drug or material that is already able to actively target or be injected directly into pathological tissue without any need for an external DDs (the molecule of coumarin as a potential Alzheimer's disease treatment[9], the immunomodulating β-glucan, which naturally occurs as spherical particles and can be targeted *via* the EPR effect[113], etc.). The theranostic system is then obtained after simple modification of such a system with the imaging modality. Another example is the molecules for imaging methods that simultaneously can serve as therapeutics, such as tracers for radiotherapy (simultaneous detection with PET/SPECT and tissue radioablation *in situ* after irradiation) and phototherapy (fluorescent photosensitizers that create ROS after irradiation *in situ* or thermal ablation of the tissue). The last example is architectures having an imaging modality directly as a building unit of the system, such as the fluorinated polymer, being able to form particles or implants and be visualized by ^{19}F MRI.[29,64–66,105] These polymers are then capable of *in situ* or targeted drug delivery with simultaneous diagnosis and need to be modified only to manage accelerated release of the drug under exact conditions (**Figure 12**).

1.3.1. Theranostic ^{19}F MRI tracers

The remarkable strength of the C-F bond provides numerous unique properties to fluorinated compounds, such as chemical and thermal inertness, immiscibility with both water and most organic solvents, and the ability to dissolve oxygen.[31] As previously mentioned, the oldest

commonly used tracers were PFC nanoemulsions (**Table 1**). The first applications of PFCs as a theranostic material were investigated by Ahrens et al. in 2005.[59] He found that PFCs can be used as potential immunotherapeutic in a cell tracking device, replacing the commonly used superparamagnetic iron oxide (SPIO, T_2 contrast agent), which suffers from artifacts. Moreover, ^{19}F MRI cell tracking presents a quantitative method that is not possible with CAs due to the high background. Ahrens's research was followed by many other research groups applying ^{19}F tracers for cell tracking, such as macrophages[114] or stem cells.[115] Theranostic systems based on PFCs have been investigated in several other biomedical applications, such as in angiography (imaging the inside of the blood vessel) as an alternative to T_1 CAs,[116] as a potential high intensity focused ultrasound (HIFU) contrast agent,[48] *etc*. However, the PFCs have several limitations, mostly the high lipophilicity causing long retention times in the organism or the splitting of the signal intensity due to nonequal fluorine atoms. To overcome these drawbacks, macromolecular particles were developed as ^{19}F MRI probes. These probes were further modified to present targeting moieties and stimuli-responsive behavior to become an advanced new class of theranostic systems as ^{19}F MRI tracers. Some of the macromolecular ^{19}F MRI tracers for diagnostic application are summarized in **Table 2**, accompanied by the reference. Some examples of developed theranostic ^{19}F MRI tracers are summarized in **Table 3**.

Table 3. Examples of theranostic systems for ^{19}F MRI.

Stimuli	Targeted environment	Release mechanism	Type of tracer	Ref.
Temp.	Higher temp. (42 °C)	Accelerated DR at higher temperature	Peptidic M-PEG with fluorinated L-Lysine	117
pH	Lower pH	Accelerated DR at low pH	PEGylated crosslinked nanogel with CF$_3$ groups	118
			Diblock copolymers PEG-*b*-Poly(*N*-alkylacrylates) containing pH-sensitive and fluorinated groups	119
			PPEGMA star polymer with TFEA and DMAEMA branched core	120
			Metal organic framework ZIF-8 carrier containing a TFMIM ligand core coated with PEG	121
			Polyacrylamides containing DFEA, ImPAM and HEAM	66,105
Redox	ROS	DR after oxidation	PEG-*b*-poly(TFEMA-*co*-ETEMA) copolymers	121
			PHPMA-b-poly(DFEA-co-FcAEA)	Ch. 3.3
	Hypoxia	DR after reduction	Branched fluorinated glycopolymers	122
			Fluorinated Cu(II)ATSM derivatives	123
Enz.	β-gal	Enzymic hydrolysis	Fluorosalicylaldehyde aroylhydrazone β-d-galactopyranoside	124
			2-Fluoro-4-nitrophenyl β-d-galactopyranoside	125
	Caspase-3	Cleavable linker	FLAME-DEVD2	126

1.4. Choice of the polymers and synthesis

All polymers described in this thesis are based on the thermoresponsive poly[N (2,2 difluoroethyl)acrylamide] (PDFEA). PDFEA is the building unit of these systems as well as the imaging moiety with 28 m/m % magnetically equivalent fluorine atoms, providing one signal in ^{19}F MRI. As elaborated earlier, thermoresponsive polymers may create supramolecular structures depending on the architecture of the polymer. The polymers described in this thesis can be divided into two groups – block copolymers creating supramolecular particles (**Chapter 3.1.**) and statistical copolymers creating polymeric implants (**Chapter 3.3.**). All polymers were prepared to achieve a narrow molecular mass distribution (dispersity $Đ \leq 1.20$) using a living polymerization method, which is usually required for biomedical applications.

1.4.1. Living polymerizations

The so-called living polymerizations are a group of techniques that result in well-defined polymers with low polydispersity (Đ), tunable lengths and control over the initiating and terminating groups. The end groups can be further modified after polymerization to incorporate, *e.g.*, the targeting or imaging unit or to continue polymerization with another block. Living polymerizations are providing a controlled polymerization rate. This can be achieved with less active polymerization centers relative to, *e.g.*, the hydrocarbon radical center in traditional radical polymerizations. The most common living polymerization techniques are atom transfer radical polymerization (ATRP), living cationic or living anionic polymerizations, reversible addition fragmentation chain transfer (RAFT), and ring-opening metathesis polymerization (ROMP).

In this thesis, we describe two different polymerization techniques. The first is RAFT polymerization, which can be used to obtain, *e.g.*, polyacryl- or polymethacrylamides. The mechanism of RAFT polymerization is based on a reversible chain transfer equilibrium between active and dormant chains (**Figure 13**).[127]
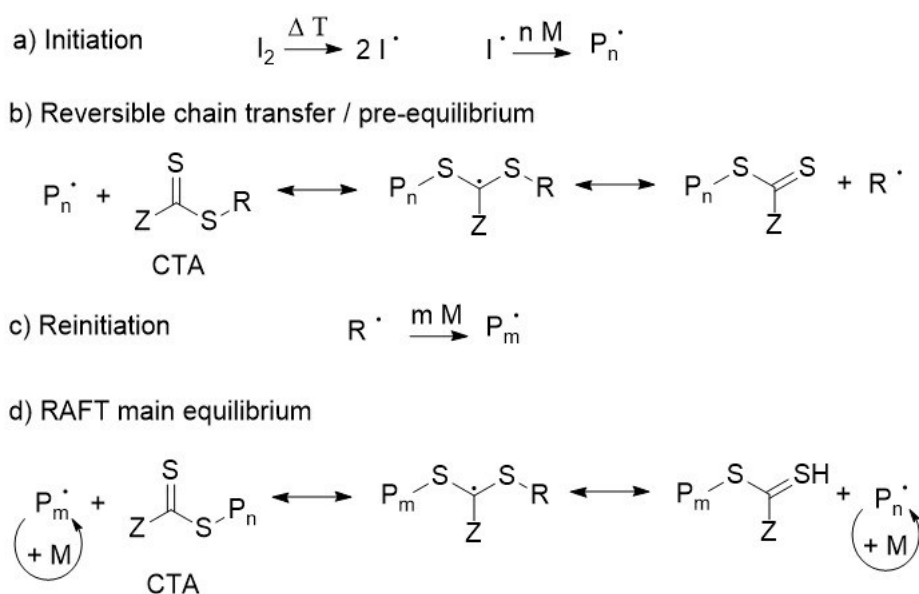
Figure 13. Schematic mechanism of RAFT polymerization.

The first step is initiation, analogous to traditional radical polymerization, where we obtain the active species $P_n\cdot$. The most widely used initiator systems in RAFT are 2,2′-azobis(2-methylpropionitrile) (AIBN) and 4,4'-azobis(4-cyanovaleric acid) (ACVA), which are activated by heat. The active chains $P_n\cdot$ react with the so-called chain transfer agent (CTA) to form an intermediate radical. Conventional CTAs are based on dithioesters or trithioesters, where the Z group (phenyl, dodecyl) has the role of stabilizing the radical intermediate, while the R group (cyanopentanoic acid, *iso*-propylcarboxylic acid) must act as a good leaving group to form the reactive R$\cdot$ radical. The next step is the fragmentation of the radical intermediate into a dormant polymeric chain containing the CTA group and the R$\cdot$ radical. Afterwards, R$\cdot$ reinitiates the polymerization and forms an active polymer chain $P_m\cdot$, which enters the rapid RAFT equilibrium between the dormant and active radicals. If the concentration of the dormant chains is higher than the concentration of the active chains (initiator:CTA ratio is approx. 1:3), then we obtain a well-defined and narrowly distributed polymer mass.

The dormant chains can also be referred to as the macroCTA, and they contain the macromolecular species and the CTA group. The macroCTA can be purified and reused for another polymerization, resulting in the formation of a diblock copolymer. The polydispersity of the resulting diblock copolymer then depends also on the stability of the macroCTA. RAFT polymerization is very sensitive to nucleophilic agents such as amines. Even traces of nucleophiles in the reaction can lead to the removal of the CTA group, resulting in the termination of the chain and broadening of the molar mass distribution. This can be overcome using more stable CTA molecules such as trithio-compounds, which are not sensitive to hydrolysis. After polymerization, the CTA group can be replaced by a functional group or an inert group by the described procedures. The macroCTA does not have to be prepared by RAFT polymerization; it can also be prepared by modifying the already prepared polymer using different polymerization techniques (PMeOx, PEG, etc.) with the CTA molecule. [128]

The second living polymerization described in this thesis is cationic ring-opening polymerization (CROP, **Figure 14**) of 2-alkyl-2-oxazolines. CROP is initiated by the alkylation (usually methyl or allyl for further functionalization) of the nucleophilic imine in the oxazoline ring, forming the activated cationic intermediate. The counteranion must be nonnucleophilic to avoid termination of the polymerization. The most commonly used alkylation agent initiators are tosylates (*e.g.*, methyl tosylate), nosylates (*e.g.*, methyl nosylate), triflates, or alkyl bromides (*e.g.*, allyl bromide). The initiation is then followed by the propagation step, where the nucleophilic imine from another oxazoline attacks the carbon in the 5 position (C_5) of the activated intermediate. C_5 is partially positively charged due to resonance equilibrium with the intermediate containing the iminium ion. Nevertheless, the carbocation is more reactive; therefore, the propagation step is favored at the C_5 end. The polymerization is terminated by a nucleophile such as hydroxide, amine, azide, or carboxylate (CTA with the carboxylic acid group), which also allows further polymerization or functionalization if required.
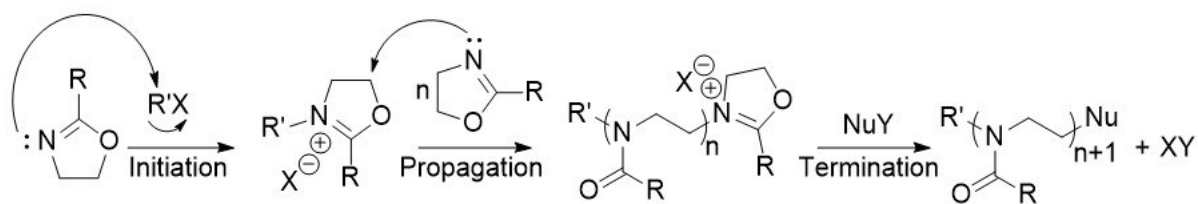
Figure 14. Schematic mechanism of the CROP of 2-substituted-2-oxazolines.

1.4.2. Block copolymers

A block copolymer is a linear polymeric architecture defined at the constitutional level, where each block comprises a specific constitutional unit – a specific monomer. By definition, block copolymers do not include branched structures, even though the branches are composed of blocks or star polymers.[129] The synthesis of block polymers can be carried out by living polymerization of the first monomer to form the first block (homopolymer A), followed by the addition of a second monomer (B), which reacts with the living active center to extend the chain and form a second block (A-B block copolymer). The addition of a 3rd monomer allows the obtention of even more complex block architectures (*e.g.*, A-B-A and A-B-C block copolymers).

1.4.3. Statistical copolymers

Statistical copolymers are copolymers where the sequence of different types of monomers follow the rules of statistics. The monomer distribution along the polymer chain is dependent on the reactivity ratios of the monomers involved. To obtain an ideal random copolymer, the reactivity ratios of all monomers must be similar. It is possible to achieve such a random or pseudorandom constitution in a copolymer when the monomers have similar chemical properties, *e.g.*, acrylamide monomers with similar polymerization rates and both well soluble in the solvent used for the polymerization.

1.4.4. Biocompatibility of polymers

Polymers constituted by a saturated hydrocarbon chain have been found to be nondegradable in most living organisms.[130,131] However, polymers must eventually be excluded from the body to avoid bioaccumulation. It has been found that numerous hydrophilic polymers, *e.g.*, polyacrylamides, polyoxazolines or PEG, can be eliminated *via* the kidneys (renal clearance). However, the kidneys have a size threshold (so-called renal threshold), which means that molecules above a certain molar mass (approximately 45 kDa for acrylamide-type polymers [132]) have a slower renal elimination or cannot be excreted. This is not a sharp threshold: even heavier molecules may be excreted *via* the so-called worm-like effect, and charged, rigid or lipophilic molecules may have a substantially different renal threshold. The estimated renal threshold for hydrophobic polymers is considered to be higher due to the higher packing degree of the polymer in the water environment. On the other hand, polymer coating can prolong the circulation time of a drug and its biodistribution in the body. A well-known method based on this finding is PEGylation, *i.e.*, coating with poly(ethylene glycol). This technology was developed to prolong the circulation of therapeutic proteins in an organism by using a polymeric carrier (in this case PEG), which shields the drug from proteolytic enzymes and decreases its renal clearance.[133]

In general, the residence time of a polymer in an organism can be controlled by the chain length. **Figure 15** shows a comparison of the biodistribution of PEG and

poly(2-ethyl-2-oxazoline) (PEtOx) as a function of their chain length (expressed as size, from 20 to 70 kDa) measured by μPET/CT.[131] The biodistribution of the polymer to the kidneys is clearly visible, and the longer the polymer length is, the longer the residence time in the body. The signal visible in the livers was later proven to be an artifact caused by the disassembly of the ^{89}Zr complex.[134]
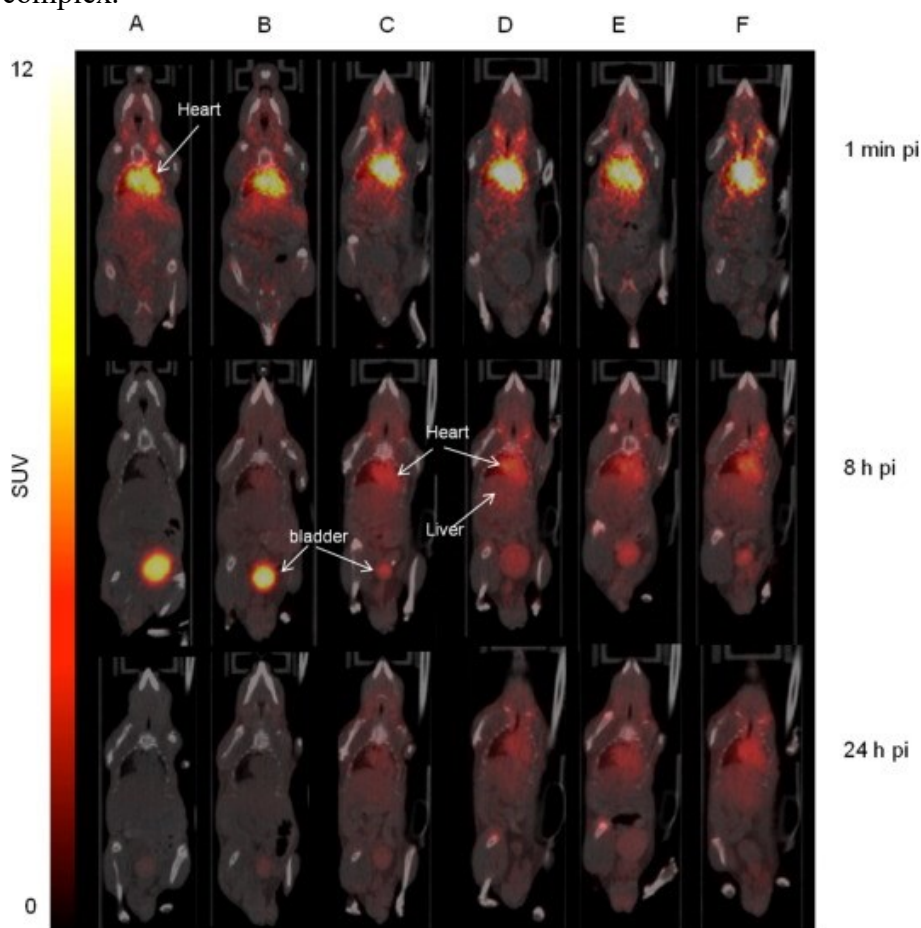
Figure 15. Representative μPET/CT images of C57/BL6J mice intravenously injected with 100 μg (corresponding to 3.7–22 MBq) of ^{89}Zr-Df-PEtOx 20 kDa (A), ^{89}Zr-Df-PEG 20 kDa (B), ^{89}Zr-Df-PEtOx 40 kDa (C), ^{89}Zr-Df-PEG 40 kDa (D), 89Zr-Df-PEtOx 70 kDa (E) or ^{89}Zr-Df-PEtOx 110 kDa (F). PET images are presented in coronal orientation at 1 min, 8 h and 24 h post tracer injection.[131]

Another case are polymeric assemblies. Polymeric nanoparticles are too bulky to be excluded from the body *via* urine. The disassembly of these supramolecular particles into polymeric chains is equilibrium-based and the polymeric chains can eventually be below renal threshold and therefore eliminable from the body by renal route. In other words, the kinetics of the equilibrium between the polymer forming the particle and free polymer chains in solution determine the biodegradability of the system over time. It has been found that polymers with strongly hydrophobic chains can form particles with a so-called 'frozen' core, especially if glass transition temperature of the core is above the measurement temperature, where the equilibrium kinetics rate is close to zero.[135] The biodegradability of these systems is very slow, which makes them rather unsuitable for medicinal use.

1.5.   Methods for characterization of polymers and their assemblies

1.5.1. 1D and 2D NMR measurements

One-dimensional NMR experiments, such as ^{1}H (proton), ^{13}C (carbon), and ^{19}F (fluorine) NMR measurements (**Chapter 1.1.**), are crucial for determination of the polymer composition and purity. Conventional ^{1}H NMR measurements have three stages – first, the sample is placed into a strong magnetic field, then the spins are exited using an RF pulse, and last, the precession of the magnetization vector is measured as the FID and processed with the Fourier transform to obtain the spectrum. In the case of too strong heteronuclear coupling between nuclei (*e.g.*, ^{13}C), pulse sequences able to decouple neighboring nuclei are applied.

To assign the peaks in a complicated spectrum precisely or to determine the 3D structure of the polymer/particles, we can use more advanced one-dimensional and two-dimensional NMR methods. The most common advanced NMR methods are correlation spectroscopy (COSY), diffusion ordered spectroscopy (DOSY), exchange spectroscopy (EXSY), nuclear Overhauser effect spectroscopy (NOESY), etc.[136]

Heteronuclear single quantum coherence spectroscopy (HSQC) is used to detect correlations between nuclei of two different elements (heteronuclear) that are separated by a single chemical bond. HSQC works by transferring magnetization from one nucleus to the other nucleus using so-called cross-polarization. The measurement results in a two-dimensional spectrum, with which we can determine the molecular structure.

To determine the conformations of a polymer in a solution or as a part of an assembled particle, we can use a method based on the so-called nuclear Overhauser effect (NOE). The NOE is defined as a change in one spin intensity when the spin transition of the nuclei in spatial proximity is perturbed from equilibrium. In other words, NOE spectroscopy (NOESY) can give the 3D geometry obtained from evaluating the ^{1}H-^{1}H interactions of protons in proximity. In polymer chemistry, NOESY can be used, *e.g.*, to determine polymer conformations, hydrogen bonding in polymer particles or the proximity of monomers.

The diffusion NMR technique can be used to determine polymer impurities, such as low-molecular-weight compounds and oligomers, or even to distinguish between diblock copolymers and homopolymer impurities. In principle, the diffusion ordered spectroscopy (DOSY) method measures the translational self-diffusion of molecules in solution. This enables a precise analysis of a complex mixture without any prior separation of the different components.

1.5.2. Size exclusion chromatography (SEC)

SEC, initially called gel-permeation chromatography (GPC), is a method in which molecules are separated by their size (molecular weight). The separation column is packed with a porous material swollen in the mobile phase, where the size of the pores determines the range of the molar masses that are effectively separated. The first material for SEC purposes was used in 1964 by J. C. Moore, and the chemical composition was based on a porous cross-linked polystyrene material with controllable pore sizes.[137] This material was later replaced with more advanced gels, such as dextran polymer composites (Sephadex^{TM} gel) or agarose gels (Sepharose^{TM}). The possibility of determining molar mass distributions made SEC a very useful method for polymer chemists and biochemists. In addition to the analytical benefits, SEC is also very useful as a fast purification method, where we can simply filter the polymer out from low-molecular-mass impurities.

To determine the polymer molar mass distribution, a chromatographic column packed with a gel stationary phase is attached to an HPLC instrument, where it replaces the silica columns used to separate molecules based on their polarity. HPLC is further upgraded by installing an additional detector suitable for macromolecules, such as the refractive index (RI) detector or the static light scattering (SLS) detector, which allows us to determine the molar mass of the polymer directly without the need for an external standard.

1.5.3. Dynamic light scattering (DLS)

To determine the size distribution of small particles in a solution, we can use the DLS method.[138] The general principle is based on the fluctuation of an inhomogeneous environment. Small particles (nm scale) fluctuate in a solution undergoing Brownian motion, which is a random motion of the particles suspended in the solution as a result of their collisions with the molecules of the fluid. The fluctuations are analyzed by introducing an external light source, which, after interfering with particles, is scattered in all directions (Rayleigh scattering). This scattering fluctuates with the moving particles and is recorded in short time intervals and collected. These data are then analyzed by an autocorrelator, which compares the intensity of light over time. **Figure 16** shows an example of two samples with different particle sizes and the hypothetical light scattering intensity records. The velocity of the Brownian motion of the particles is inversely proportional to their size, which results in different spectra of the light scattering (LS) intensity over time.
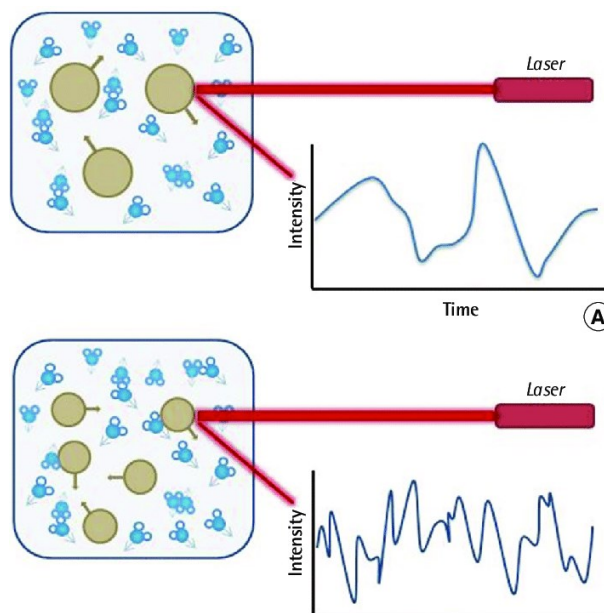
Figure 16. Hypothetical measurement of the light scattering intensity for two different samples with different particle sizes.[139]

Information about the dynamics of the particles is obtained from the autocorrelation function of the recorded intensity fluctuations, postprocessed by various data analysis methods. While the DLS initially measures the diffusion of the particles in the solution, the translation diffusion coefficient, D_t, can be determined from a first-order autocorrelation function, postprocessed as a simple exponential decay, according to equations (7), (8), and (9).

$$g^1(q; \tau) = \exp(-\Gamma\tau) \tag{7}$$

$$\Gamma = q^2 D_t \tag{8}$$

$$q = \frac{4\pi n_0}{\lambda} \sin\frac{\theta}{2} \tag{9}$$

where $g^1(q; \tau)$ is the autocorrelation function for wave vector q and delay time τ, and Γ is the decay rate. n_0 is the refractive index, λ is the incident laser wavelength, and θ is the angle of the detector relative to the incident beam.

The described equations correspond to the simplest monodisperse and diluted system (to suppress the collision between particles). D_t is then used to determine the hydrodynamic radius R_h of the spherical particles using the Stokes-Einstein equation (10),

$$D_t = \frac{k_B T}{6\pi\eta R_h} \tag{10}$$

where k_B is the Boltzmann constant, T is the temperature of the solution and η is the viscosity of the solution.

However, for polydisperse samples or nonspherical particles, the data analysis is more complex. Instead of simple exponential decay, the function is composed of the sum of the exponential decays for each population of particles, or in the case of nonspherical particles, it also contains the rotational diffusion coefficient. In conclusion, light scattering methods require rather complicated data analyses; nevertheless, once the data are processed, the information is very complex and accurate. For example, it provides information about the size of the whole moving object, including a solvation layer. This information cannot be obtained by, *e.g.*, electron microscopy due to the poor contrast; therefore, the sizes do not match when comparing the results of these two methods.

1.5.4. Static light scattering (SLS)

The SLS method provides information on the molar mass of polymers or proteins in solutions by measuring the intensity of the scattered light. Compared to DLS, the SLS method analyzes the scattered light directly, instead of monitoring the Brownian motion, using one or many detectors at one or many angles. To characterize the assemblies in the solution, we must know many parameters, such as the laser intensity, quantum efficiency of the detector, full scattering volume, solid angle of the detector, and refractive index (RI) of the sample or RI increment. However, many of these parameters are already calibrated for commercially available instruments or can be determined using additional methods (*e.g.*, the RI increment is measured by a differential refractometer). The most common way to calculate particle parameters is the Zimm equation (11),[140]

$$\frac{Kc}{\Delta R(\theta,c)} = \frac{1}{M_w}\left(1 + \frac{q^2 R_g^2}{3} + O(q^4)\right) + 2A_2 c + O(c^2) \tag{11}$$

where q is the scattering vector for vertically polarized light, c is the solution concentration and $\Delta R(\theta, c)$ is the difference between the scattering intensity of the analyte and the scattering intensity of the solvent.

During SLS, the sample is usually measured at many concentrations (at least 4) and for many different angles (multiangle light scattering - MALS). The results can be analyzed in several ways; however, for a polymer chemist, the most typical is the so-called Zimm plot (double extrapolation of the Zimm equation to zero angle and zero concentration), from which we can

obtain the radius of gyration (R_g), molecular mass (M_w) of the particle and second viral coefficient (A_2).

1.5.5. Small angle neutron scattering (SANS) and small angle X-ray scattering (SAXS)

SANS and SAXS are analogs to the previously mentioned SLS. Both are so-called small angle scattering (SAS) techniques, which measure the small deflection (angle of 0.1 - 10°) of a collimated beam of radiation (neutrons - SANS, X-rays - SAXS), occurring after collision with macromolecular structures within the size range of 1 - 100 nm. The important feature of these techniques is the possibility of analyzing the inner structure of the systems, especially the systems with nonequal arrangement of the density (micelles, vesicles, etc.). Nevertheless, to obtain valuable information about the system from the data analysis, we need to make a model assumption; otherwise, the only information we obtain is R_g. Therefore, these methods give us only additional and more detailed morphological information about the system that approximates the architecture we already determined with other methods, such as DLS or SLS.[141]

SAXS uses hard X-rays with wavelengths of 0.07 – 0.2 nm, while SANS uses a focused beam of neutrons. In comparison to the neutron source, the X-ray beam is easily available. However, the X-ray beam can heat up the sample and thus is not very suitable for thermally unstable samples. The SANS method is nondestructive; nevertheless, the possibilities for measurement are limited to neutron facilities, such as research reactors and spallation sources.

1.5.6. Transmission electron microscopy (TEM)

A transmission electron microscope is an instrument that uses a beam of electrons transmitted through a sample to form an image. Transmission electron microscopes are capable of imaging at a significantly higher resolution than light microscopes (thousands of times smaller objects) owing to the smaller de Broglie wavelength of electrons. Transmission electron microscopy is a commonly used analytical method in polymer chemistry to determine the morphology of nanoscale particles. The first TEM instrument was developed in 1931 by Max Knoll and Ernst Ruska, later awarded the Nobel Prize in physics.[142] In general, TEM can operate in an enormous array of operating modes, such as conventional imaging (with a wide range of possible contrast settings), scanning TEM (used in material chemistry), diffraction TEM, and TEM spectroscopy.

To determine the polymer assemblies in a solution, the most commonly used technique is conventional TEM imaging. During the measurement, the sample is deposited onto a TEM carbon-coated copper grid, and the solvent is removed by fast drying (*e.g.*, evaporated in a heated oven or wicked away with a piece of filtration paper). However, the fast drying method results do not describe the system very precisely due to the rather significant change in the environment. Another possible method is so-called cryo-TEM, where the sample is deposited onto a TEM holey carbon-coated copper grid and flash frozen in liquid ethane or liquid nitrogen. This method allows imaging of the sample in vitreous ice, which simulates the condition of the macromolecules in the water solution in the way most similar to reality. However, due to the low contrast, the size result does not contain the solvation layer of the particles. Moreover, during the fast freezing or drying, we cannot determine the exact temperature of the sample at which the particles froze or were dried from the solution. This information is especially important for thermoresponsive samples where the size and morphology change rapidly with a change of only a few degrees. In conclusion,

TEM is mostly used to provide information about the system supplemental to the more valuable data from light scattering methods.

1.5.7. Turbidimetry

The turbidimetry method is the fastest and possibly simplest way to determine the cloud point temperature of a polymer; nevertheless, it does not provide any additional information about the parameters of the particles. The method measures the loss of intensity of transmitted light due to the scattering caused by forming particles. Light of a known wavelength passes through a vial containing the polymer solution, and the resulting transmittance is then plotted against the temperature (**Figure 12**). This method is suitable for thermoresponsive polymer hydrogels or implants, for which no information other than T_{CP} is required. Originally, turbidimetry was developed as a biochemical method for examination of biological samples (immune reactions, denaturation of proteins, *etc.*).[143]

2. Aims of the thesis

2.1.   Preparation of thermoresponsive self-assembled polymeric nanoparticles as a highly promising tracer for ^{19}F MRI. The chosen polymer architecture is amphiphilic diblock copolymers containing poly(2-methyl-2-oxazoline) or poly[*N*-(2-hydroxypropyl)methacrylamide] as a hydrophilic block and poly[*N*-(2,2-difluoroethyl)acrylamide] as a thermoresponsive fluorinated block.

2.2.   Investigation of the inner structure of self-assembled nanoparticles based on poly(2-methyl-2-oxazoline)-*block*-poly[*N*-(2,2-difluoroethyl)acrylamide] with physically crosslinked nanogel-like properties.

2.3.   Preparation of double stimuli-responsive polymeric nanoparticles as a theranostic system for controlled drug release. The theranostic systems are based on poly[*N*-(2-hydroxypropyl)methacrylamide]-*block*-poly[*N*-(2,2-difluoroethyl)acrylamide] containing a few molar percent of a monomer with a ferrocene moiety that is sensitive to oxidation. The polymers can be used in ^{19}F MRI (reduced state) and as a T_1 contrast agent for ^{1}H MRI (oxidized state).

2.4.   Synthesis of thermo- and pH-responsive injectable self-assembled polymeric implants based on the statistical copolymers poly{*N*-(2,2-difluoroethyl)acrylamide-*co*-*N*-[3-(*1H*-imidazol-1-yl)propyl]acrylamide-*co*-*N*-(*2*-hydroxyethyl) acrylamide} suitable for ^{19}F MR imaging.

2.5.   Review of the properties and applications of the low-molecular-weight and macromolecular ^{19}F MRI tracers.

3. Results and discussion

3.1. Fluorinated thermoresponsive nanoparticles

3.1.1. Polymer design, synthesis, and characterization

We designed new nanosized particles with potential use as ^{19}F MRI tracers. Nanoparticles with an imaging modality can be used for a variety of applications such as cell/tissue labeling for transplantation or labeling of pathology *via* passive or active targeting. To obtain a system capable of forming well-defined nanoparticles, we designed various amphiphilic diblock copolymers (**Scheme 1**). These copolymers contain two different types of hydrophilic polymers combined with thermoresponsive fluorinated polymers prepared at 3 different block ratios.
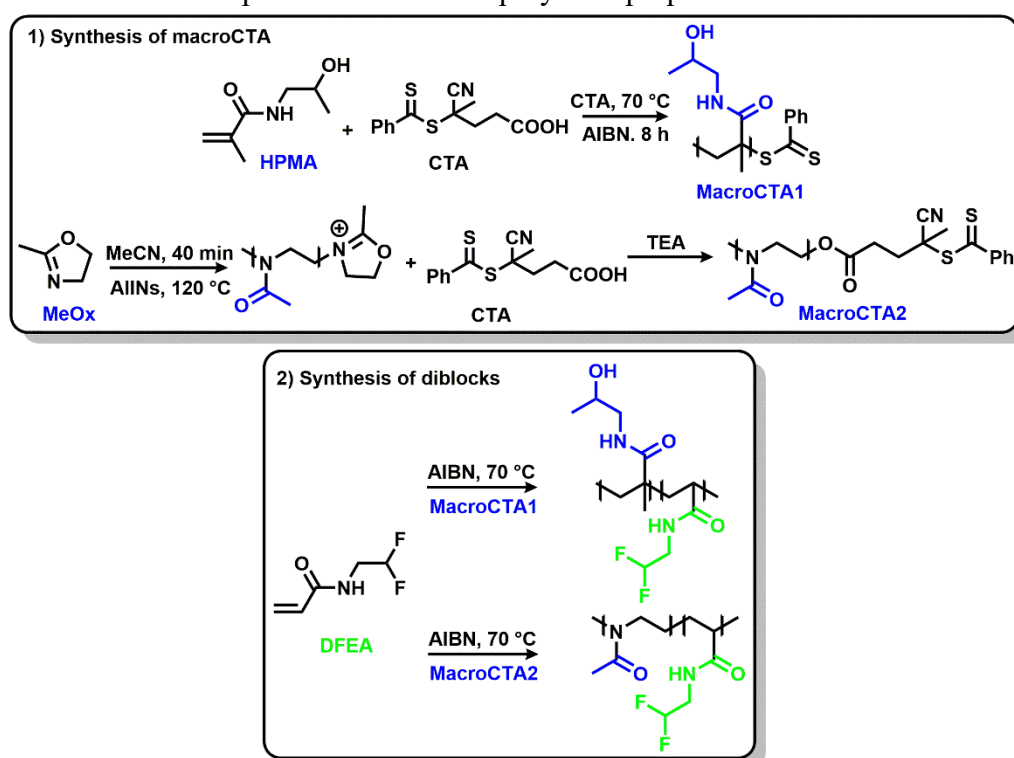
Scheme 1. Synthesis of thermoresponsive diblock copolymers *via* two-step RAFT polymerization and combined CROP and RAFT polymerization.

The copolymer poly[N-(2-hydroxypropyl)methacrylamide]-*block*-poly[*N*-(2,2-difluoroethyl)acrylamide] (PHPMA-PDFEA) was prepared by two successive RAFT polymerizations of the corresponding monomers with 4-cyano-4-(phenylcarbonothioylthio)pentanoic acid as the chain-transfer agent and-α,α′-azoisobutyronitrile (AIBN) as the initiator (**Scheme 1**). As previously mentioned, RAFT polymerization is a technique that yields polymers with a low PDI (**Chapter 1.4.1.**). The polymerization is sensitive to oxygen and nucleophiles (amines and some CTAs also to water content). Argon flushing is a sufficient method of avoiding the presence of unwanted oxygen in the flask. To avoid hydrolysis and aminolysis, the polymerization is typically performed in dry, pure solvents free of any amines. In this reaction, HPMA was polymerized in dry *tert*-butanol in an oil bath heated to 70 °C for 7 h. After polymerization, the resulting polymer was precipitated by the addition of diethyl ether and purified by gel filtration using

a Sephadex LH-20 column with methanol as the eluent. Methanol was evaporated under reduced pressure, and the polymer was purified by freeze-drying. To initiate polymerization of the second block, the concentration of CTA1 in macroCTA1 was first determined by UV−vis spectroscopy. The second block was prepared by polymerization of the DFEA monomer in dry DMF overnight in an oil bath at 70 °C. The resulting polymer was purified by the same procedure as that with PHPMA. After the polymerization was complete, the dithiobenzoate end-group was removed by radical reaction with AIBN to avoid the influence of the CTA end-groups on the thermoresponsive properties.

Poly(2-methyl-2-oxazoline)-*block*-poly[*N*-(2,2-difluoroethyl)acrylamide] (PMeOx-PDFEA) was prepared by CROP polymerization of the MeOx monomer and subsequent RAFT polymerization of the DFEA monomer (**Scheme 1**). CROP polymerization is a living polymerization, which also results in polymers with a narrow molecular weight distribution (**Chapter 1.4.1.**). In contrast to RAFT, where unfavorable hydrolysis side reactions only occur with sensitive CTAs, CROP is highly sensitive to even trace amounts of water in the polymerization mixture. Therefore, the monomer was distilled under an inert argon atmosphere in the presence of a desiccant (in our case, calcium hydride), and dry acetonitrile was used as the solvent. The polymerization of MeOx was performed in Ace$^®$ pressure tubes in an oil bath heated to 120 °C for 30 min. After the polymerization, the cationic living chain-ends were treated with triethylammonium salt of 4-cyano-4-[(dodecylsulfanylthiocarbonyl)sulfanyl]pentanoic acid (CTA2) to form macroCTA2. The polymer was purified by the same procedure as the previous polymers, and the concentration of CTA2 was determined by UV-vis spectroscopy at $\lambda = 308$. The second block was prepared by RAFT polymerization of the DFEA monomer using the same polymerization conditions and purification methods as those used for the PHPMA-PDFEA copolymers. The trithiocarbonate end-group was removed by aminolysis followed by Michael addition.

To describe the unknown properties of the newly developed amphiphilic systems, all copolymers were prepared with three different block ratios (**Table 4**, HF1-3 and MF1-3 copolymers). The disappearance of CTA1 and CTA2 was confirmed by NMR spectroscopy (**Figures 14** and **15**). The purity of the polymer and the block ratios were determined by NMR analysis (**Figures 14** and **15**) using the methylene protons of the CHF$_2$ group of PDFEA ($\delta = 5.9$), the proton coupled with the carbon atom of the CHOH group of PHPMA ($\delta = 3.9$), and protons of the CH$_3$ group of MeOx ($\delta = 2.1$). All prepared polymers were obtained with a narrow molecular weight distribution and a PDI < 1.20, and the molecular sizes of the prepared polymers ranged from 10 to 55 kDa. Molecular weights and polydispersity were obtained using SEC (**Table 4**, **Figure 16**).
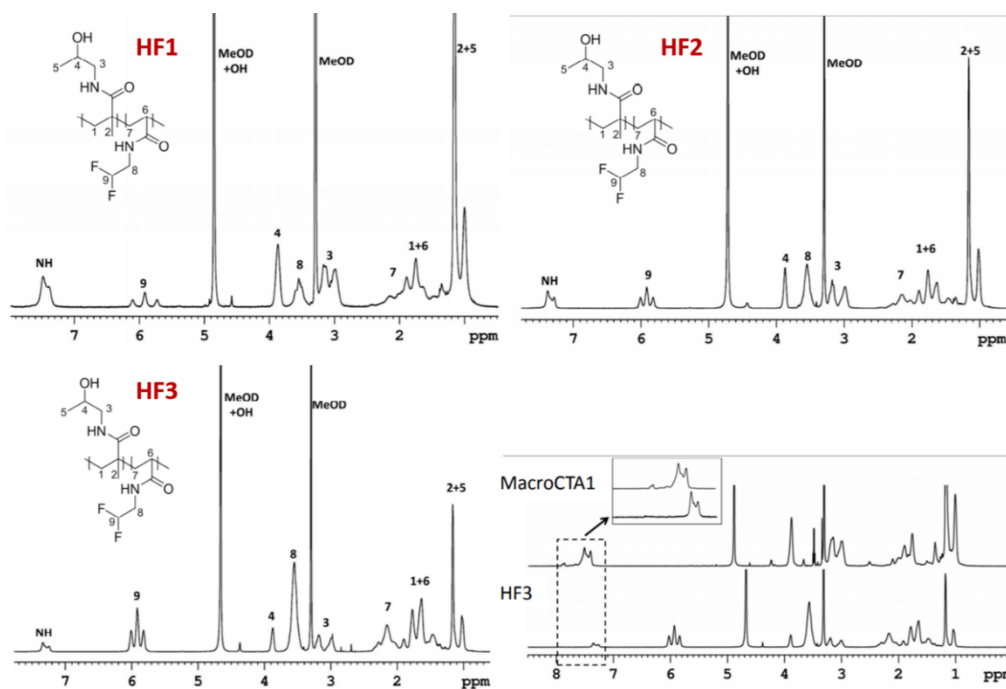
Figure 14. The 300.1 MHz ^{1}H NMR spectra of copolymers HF1 (block ratio PHPMA-PDFEA 2:1), HF2 (block ratio PHPMA-PDFEA 1:1), HF3 (block ratio PHPMA-PDFEA 1:2), and the CTA1 end-group removal (bottom right). All spectra were acquired using a Bruker Avance III 600 (or Avance DPX 300) spectrometer operating at 600.2 MHz (300.1 MHz).
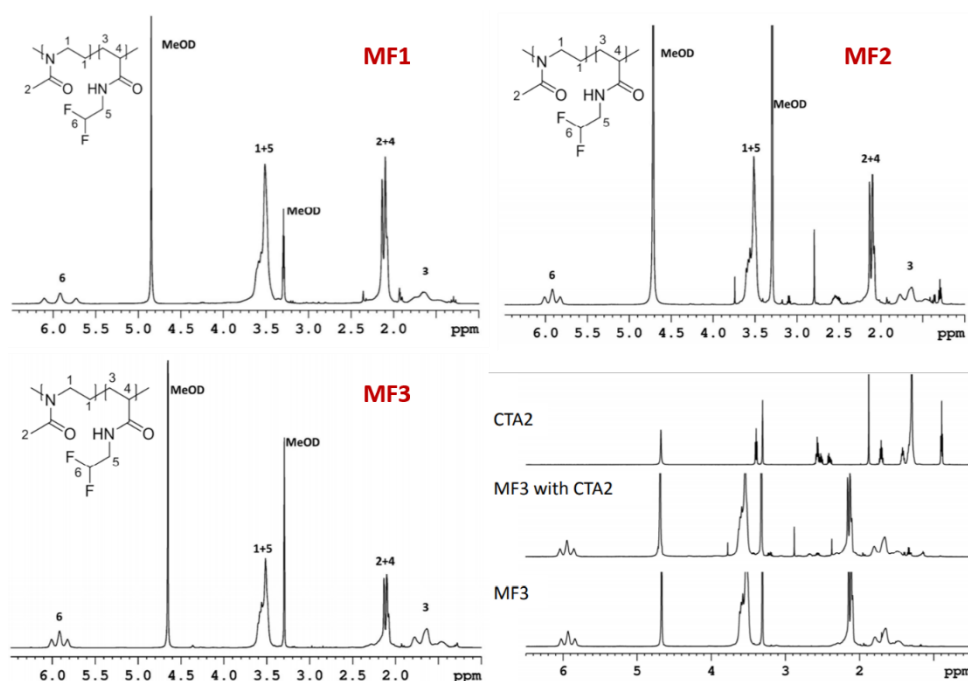

Figure 15. The 300.1 MHz ^{1}H NMR spectra of copolymers MF1 (block ratio PMeOx-PDFEA 2:1), MF2 (block ratio PMeOx-PDFEA 1:1), MF3 (block ratio PMeOx-PDFEA 1:2), and the CTA2 end-group removal (bottom right). All spectra were acquired using a Bruker Avance III 600 (or Avance DPX 300) spectrometer operating at 600.2 MHz (300.1 MHz).
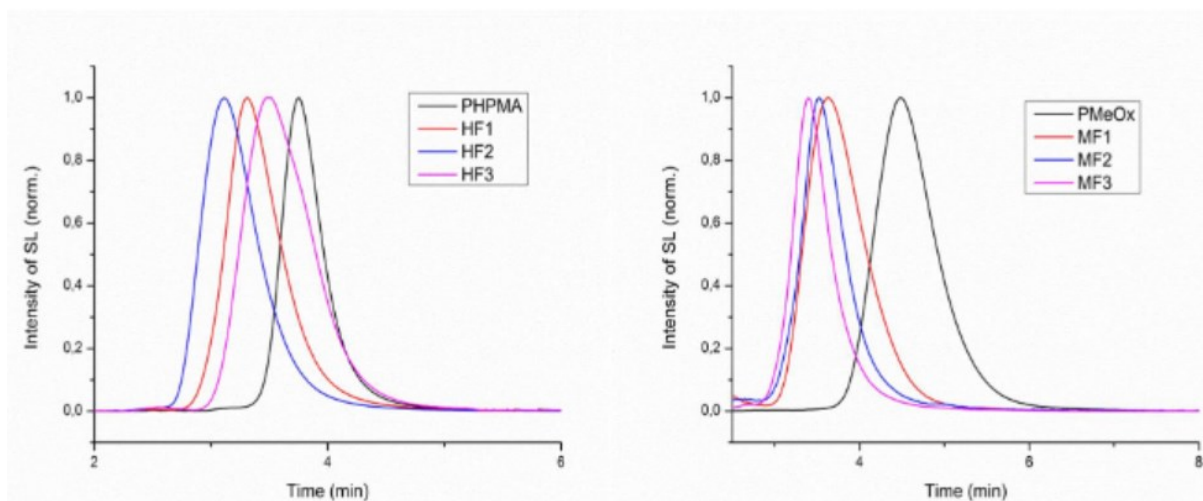
Figure 16. Size exclusion chromatography (SEC) results of the hydrophilic blocks (PHPMA, PMeOx) and the corresponding diblock copolymers (HF1, HF2, HF3, MF1, MF2, MF3) with a mixture of a methanolic 5.0 mg·mL^{-1} polymer solution and sodium acetate buffer (0.3 M, pH 6.5) (80:20 w %, flow rate of 0.5 mL·min^{-1}) as the mobile phase. The SEC instrument uses an HPLC Ultimate 3000 system (Dionex, USA) equipped with an SEC column (TSKgel SuperAW3000 150 × 6 mm^2, 4 μm) and three detectors: UV/Vis, refractive index (RI) Optilab®-rEX and multiangle light scattering (MALS) DAWN EOS (Wyatt Technology Co., USA).

Table 4. Physicochemical characteristics of the prepared polymers.

Sample name	Polymer	Block ratios[a]	w % of fluorine	M_w (kDa)[b]	M_n (kDa)[b]	Đ (M_w/M_n)
MacroCTA1	PHPMA	-	-	13.3	12.7	1.05
HF1		2:1	6.7	17.6	15.8	1.11
HF2	PHPMA−PDFEA	1:1	16.9	33.7	31.9	1.06
HF3		1:2	20.7	51.5	48.3	1.07
MacroCTA2	PMeOx	-	-	8.1	7.2	1.12
MF1		2:1	10.1	12.7	11.9	1.07
MF2	PMeOx-PDFEA	1:1	14.0	16.2	15.3	1.06
MF3		1:2	18.7	24.5	22.8	1.08

[a]Determined by NMR spectroscopy. [b]Determined by SEC. [c]Determined by DLS.

3.1.2. Determination of the self-assembly property

All copolymers exhibited an LCST behavior; above a certain temperature, the polymer chains, which were dissolved in aqueous environment (150 mM PBS buffered saline), started to assemble and form larger particles. The change in the hydrodynamic radii (R_h) was measured in the temperature range from 10 to 50 °C by dynamic light scattering (DLS). The cloud-point temperature (T_{CP}) was determined as the temperature at which the small polymer chains with R_h corresponding to a few nanometers formed larger clusters with R_h corresponding to tens of nanometers (**Figure 17** and **18**). The T_{CP} was investigated for 3 different polymer concentrations (1, 5, 10 mg·mL^{-1}); however, the concentration appeared to have only a minor influence on the T_{CP}. On the other hand, the T_{CP} appears to be highly dependent on the ratio

between homopolymer blocks in the copolymers with PHPMA, in which the higher content of the more hydrophobic block resulted in the lower T_{CP}. However, the copolymers with PMeOx did not show the same trend (**Table 5**), implying that this effect was also dependent on the type of hydrophilic monomer, consistent with other studies.[135] The reversibility of these temperature-dependent changes was also investigated. After DLS, the polymer solution was cooled from 50 °C to 10 °C, and the data were collected. The results showed that the nanoprecipitation was fully reversible. This is important for the unimer-nanoparticle equilibrium-based degradability of the particles. The DLS results are summarized in **Table 5**.

One of the possible applications is the imaging of tracers accumulated in tumors *via* the EPR effect. To accomplish this goal, we selected the polymers HF3 and MF3 (in which the ratio between hydrophilic and PDFEA blocks is approximately 1:2) as ideally sized polymeric nanoparticles. To fully determine the properties of these particles, the samples of HF3 and MF3 were further analyzed by static light scattering (SLS) to obtain the respective particle molecular weights ($M_{w,par}$), radii of gyration (R_g) and nanoparticle densities (ρ) (**Table 5**).

Table 5. Physical properties of self-assembled particles.

Sample name	T_{CP} (°C)*[a]	$R_h \pm \sigma$ (nm)[a]	$M_{w,par}$ (MDa)#[b]	R_g (nm)[b]	ρ (g·cm^{-1})[b]
HF1	37	123 ± 19	-	-	-
HF2	31	35 ± 5	-	-	-
HF3	23	77 ± 52	66.8	106	0.022
MF1	31	670 ± 203	-	-	-
MF2	30	31 ± 12	-	-	-
MF3	33	47 ± 14	10.4	67	0.013

*Polymer concentration 1 mg·mL^{-1} in 150 mM PBS buffer. #Molecular weight of self-assembled particles. [a] Determined by DLS. [b] Determined by SLS.

The DLS measurements yield the hydrodynamic size of the particles, which can be considered accurate because our particles are spherical objects. To investigate the morphology of the particles, we employed transmission electron microscopy (TEM) measurements in addition to the DLS measurements. The samples for the TEM measurements can be prepared in several ways. First, a solution of the polymers (the chosen concentration was 5.0 mg·mL^{-1} in a 150 mM PBS buffer solution) and the tools needed for sample preparation were heated to 50 °C to ensure that the temperature was above the T_{CP} during the measurement. One way to obtain TE micrographs is called fast drying: 2 μL of the solution is deposited onto a TEM carbon-coated copper grid, and the solvent is removed either by evaporating in a heated oven at 50 °C or by touching the bottom of the copper grid with a small piece of filter paper. The second method is cryo-TEM: 3 μL of the solution is deposited onto a holey carbon-coated copper TEM grid, flash-frozen in liquid ethane, and kept under liquid nitrogen. The preparation of the TEM samples is very different from the direct measurement of the solution at a given temperature, as in case of, *e.g.*, the DLS method, which is the main reason for the different size values.

Selected examples of polymers evaluated by DLS and TEM are shown in **Figure 17** (polymer MF1) and **Figure 18** (polymer HF3).
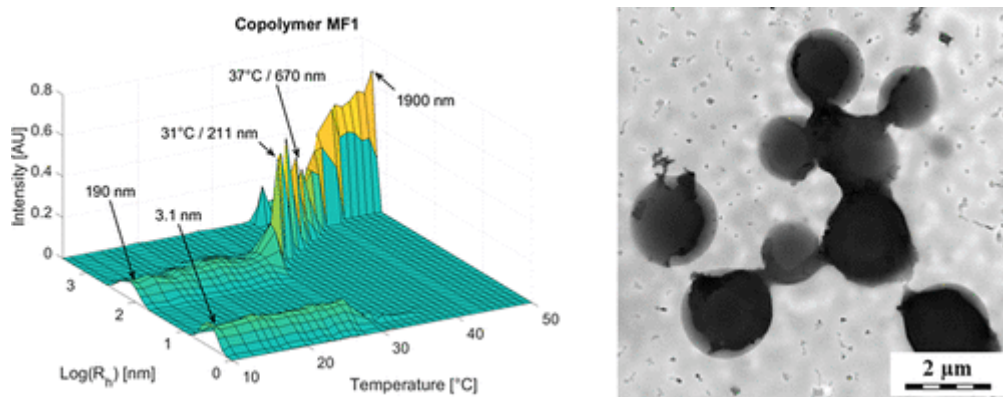

Figure 17. Self-assembly of MF1 (1% polymer solution in 150 mM phosphate-buffered saline, pH 7.4): 3D graph of the dependence of the size distribution on the temperature (left), and TEM image (right).
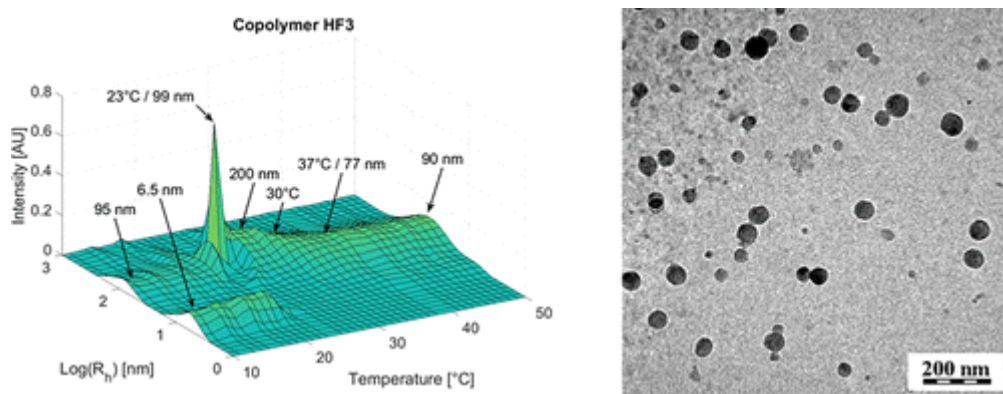
Figure 18. Self-assembly of HF3 (1% polymer solution in 150 mM phosphate-buffered saline, pH 7.4): 3D graph of the dependence of the size distribution on the temperature (left), and CryoTEM image (right). The peak with the increased intensity at 23 °C is attributed to anomalous micellization.

The results showed that both polymers (PMeOx-PDFEA and PHPMA−PDFEA) formed substantially larger particles when the amount of hydrophilic monomer was higher (note copolymers MF1 and HF1 in **Table 5)** and smaller particles when the amount of PDFEA was higher (copolymers MF3 and HF3). The particles of both polymers prepared at a ratio of 1:1 were unstable during the TEM sample preparation; moreover, DLS did not provide very comprehensive information. However, the results obtained for the other polymers were very interesting. The morphology of the polymers prepared with different block ratios was exactly opposite to the expected morphology estimated morphology based on the packing theory (**Figure 10**). The results show that the morphology of self-assembled particles is quite extraordinary traditional micelles or vesicles. In this study, we proposed the theory that these particles are based on nanogels that are physically crosslinked *via* hydrogen bonding between amide groups. This theory was supported by the DLS, TEM and additional SLS results of the HF3 and MF3 polymers (**Table 5**). The first indication was the size of the particles (by DLS and SLS): the particles were too large to be considered simple micelles. The second

indication was the very low density of the particles (determined by SLS, **Table 5**), which indicated a nanogel or vesicular system. However, vesicular particles can be distinguished by TEM due to their nonuniform distribution, which was not observed in our micrographs. The last indication was the molecular weight of the particles ($M_{\text{w,par}}$), indicating that approximately 500 −1000 polymer chains comprise one nanoparticle, while micelles usually contain approximately 10 −100 polymer chains.

Moreover, we hypothesized that our polymers could be described according to the "plum pudding" model of an atom. Most of the volume of the particles is formed by hydrated hydrophilic blocks whose chains are swollen and extended in aqueous environments, and within this hydrophilic gel (the "pudding"), smaller pockets of hydrophobic blocks (the "plums") are noncovalently bound to each other. This theory was based on the morphological arrangement to explain the size ratio of the blocks versus the size of the particles: Polymers with a larger amount of PDFEA blocks contain insufficiently long hydrophilic polymer segments and form larger particles (and vice versa). However, this theory was shown to be wrong in a subsequent and more detailed study of the inner structure of these particles, where we proposed a rather uniform distribution of both polymer blocks throughout the particle volume. These results are described in more detail in **Chapter 3.2**.

3.1.3. Biocompatibility studies

The selected samples HF3 and MF3, which were characterized by an ideal size and monodisperse particle population as well as the highest content of fluorine among all the samples (important for ^{19}F MRI purposes), were further evaluated in several *in vitro* studies. As previously mentioned, the reversibility of self-assembly is a very important property to avoid slow particle degradation and bioaccumulation in living organisms. On the other hand, if the stability of the particles is too low, the system can degrade too fast and fail to accomplish the intended task. A common method to determine the stability of the system is the assessment of the so-called critical association concentration (CAC, **Chapter 1.5.9.**). Solutions of the copolymers for measuring the CAC were prepared by direct dissolution in cold phosphate-buffered saline (PBS, 150 mM, pH 7.4) at a concentration range from 1 to 10^{-5} mg·mL^{-1}. The CAC was measured using pyrene as a fluorescence dye, which undergoes a spectral change in response to a change in the environment (hydrophobic core of the particle versus water solution). The CAC was then determined as the intersection between the decay curve, corresponding to the decrease in the particle concentration, and the stational curve, where the particles are no longer present. The resulting CAC of HF3 was 51.6 mg·L^{-1}, and the CAC of MF3 was 26.2 mg·L^{-1}, both of which were considered sufficient for the intended applications.

To assess the biological properties, the cytotoxicity of the polymers was studied. The copolymers HF3 and MF3 did not show any significant cytotoxicity even at the highest tested polymer concentrations of 1 g·L^{-1} towards all tested cell lines (HeLa - human cervical carcinoma, J774A.1 - murine monocyte/macrophage, HF - primary fibroblasts and SU-DHL-5 - human B lymphoblast). Subsequently, we measured the interaction of the polymers with red blood cells to rule out a possible hemolytic effect of the polymer. The HF3 copolymer induced no hemolysis after a 3-, 6- or 24-h incubation at 37 °C within the tested concentration range (*i.e.*, 100 to 800 µg·mL^{-1}). The MF3 copolymer caused

no observable hemolysis after a 3-h incubation within the tested concentrations. However, the onset of hemolysis (*i.e.*, values ranging from 2 to 4%) was observed at longer incubation times (6 and 24 h) and higher polymer concentrations (200, 400, and 800 μg·mL^{-1}). This behavior might be caused by the amphiphilic character of the polymers; however, the level of hydrolysis as well as the high concentration were not relevant for the intended application. In conclusion, the polymers were considered nontoxic based on the cytotoxic results of the samples at relevant concentrations.

3.1.4. ^{19}F relaxation times, MRS and MRI measurements

Finally, the suitability of polymers HF3 and MF3 for ^{19}F MRI applications was studied. The first measured parameter was the T_1 of ^{19}F nuclei. Interestingly, no noticeable change in the ^{19}F T_1 relaxation times was observed with the phase-transfer of the polymers in the solution. The main reason could be that the physically crosslinked nanogels still contain a rather high concentration of water molecules inside their cavities (in contrast to, *e.g.*, a micelle with a highly hydrophobic core). Further MR spectroscopy experiments showed the dependence of the signal on the temperature (**Figure 19**). However, the temperature effect was negligible for MRI purposes.

The possibility of using the polymer as a ^{19}F MRI tracer was experimentally confirmed by measuring aqueous polymer-containing phantoms with various tracer concentrations and total acquisition times. At a relatively short total acquisition time (17 min 4 s), even the most diluted sample (3.3 mg·mL^{-1}) could be detected (**Figure 19**). The thermoresponsive nanogels appeared to have a fairly high sensitivity as ^{19}F MRI tracers even in their solidified state and thus could be considered a very promising diagnostic tool that, after further modification, could be employed in more advanced applications.
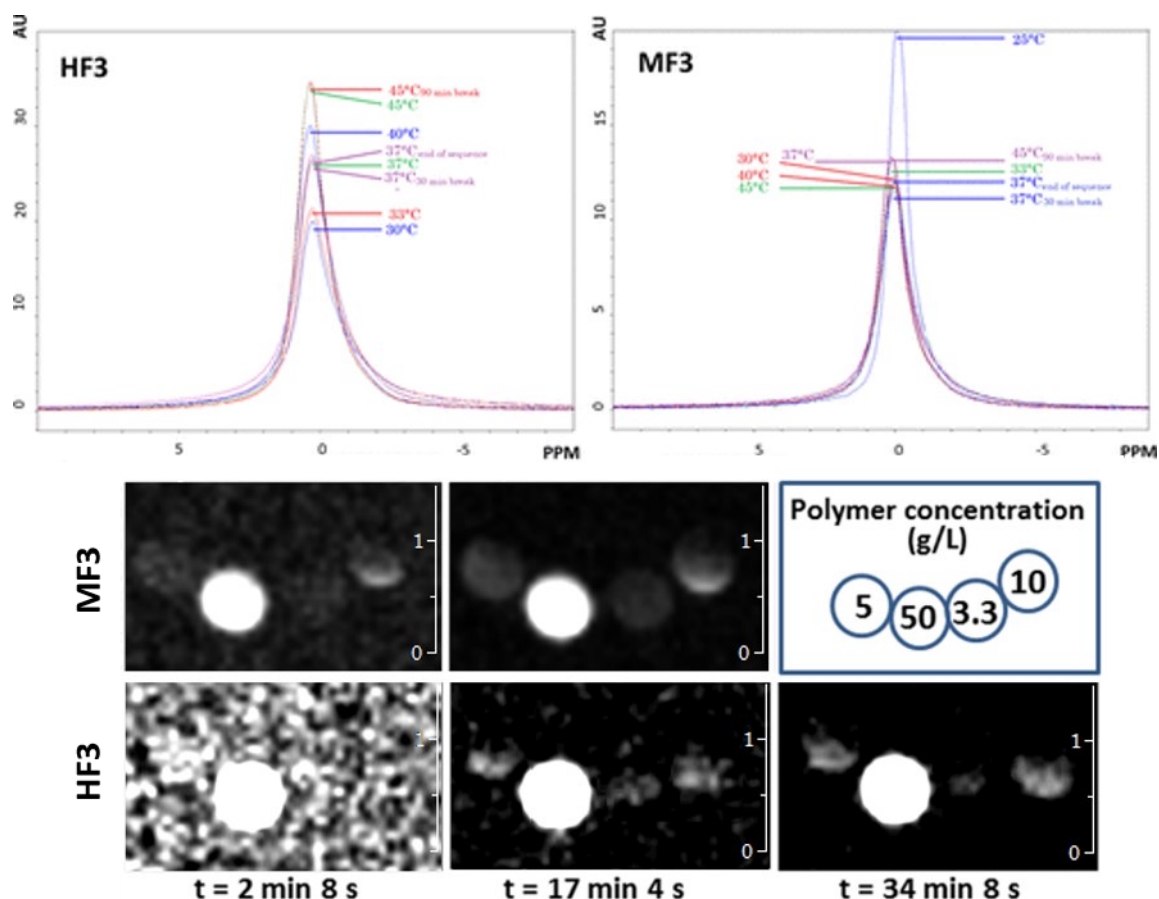
Figure 19. Temperature-dependent MR spectrum (top) and the MRI of phantoms (bottom). The MRS was acquired for the highest polymer concentration of 50 g·L^{-1}. The ^{19}F MRI is displayed for three different acquisition times.

3.2. Investigation of the inner structure of poly(2-methyl-2-oxazoline)-*b*-poly[*N*-(2,2-difluoroethyl)acrylamide] copolymer

3.2.1. The aim of this study

The poly(2-methyl-2-oxazoline)-b-poly[N-(2,2-difluoroethyl)acrylamide] self-assembled nanoparticles with a ratio of 1:2 (copolymer MF, in a previous study MF3) showed great potential in biological applications as diagnostic tools. The morphology and internal structure of the particles should therefore be thoroughly investigated. In general, these investigations are also helpful to gain insight into the temperature-dependent self-assembly behavior of copolymers composed of hydrophilic and thermoresponsive blocks. Many studies focusing on biomedical applications describe amphiphilic particles as simple micelles or vesicles; however, a thorough description of the system is usually missing. In this study, we investigated the morphology of MF-based particles using various techniques. In our previous study, we proposed the structure of the particle as a physically crosslinked nanogel with the areas of accumulated PDFEA (plums) stabilized by a hydrophilic polymer gel (pudding) (**Chapter 3.1.**). In this study, we revealed that the particle structure was rather unorganized; however, the interaction between the monomers suggested the separation between the PDFEA and PMeOx blocks. Moreover, we found that the whole system was formed initially from small micelle-like structures, which are present above the cloud point temperature (T_{CP}).

The presence of thermoresponsive homopolymer chains, however, caused the formation of larger aggregates interconnected through hydrophobic networks and hydrogen bonds, which contained large amounts of solvent (**Figure 20**).
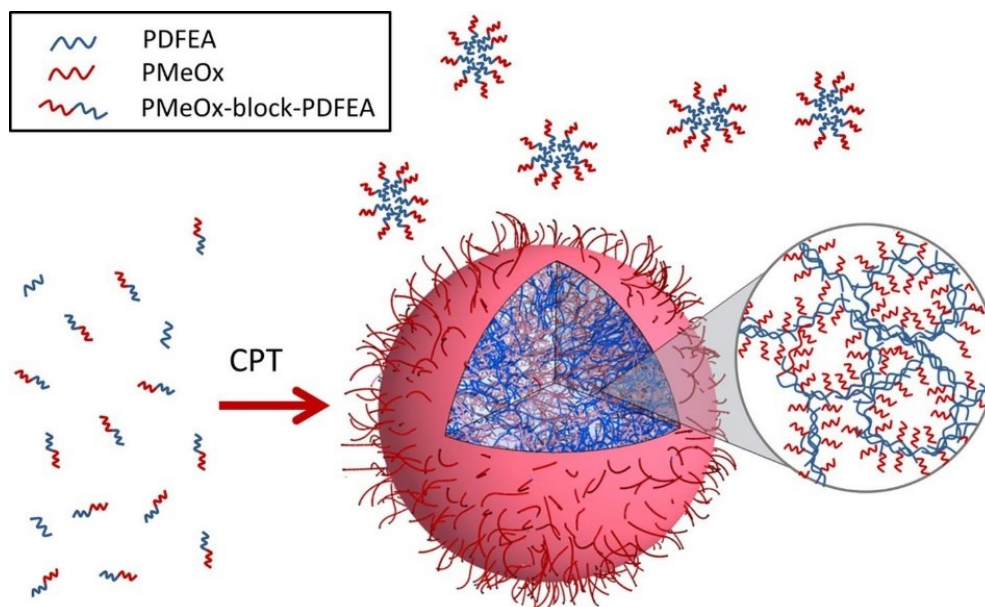

Figure 20. Schematic illustration of the thermoresponsive MF3-based particles.

3.2.2. Investigation of the morphology by light scattering methods

The temperature dependence of the size distributions was first measured by DLS in several solvents (H_2O, D_2O, and PBS in H_2O) to account for the fact that different solvents may be required in various experimental methods. The measurements in D_2O were particularly important as a reference for our SANS and NMR measurements. The importance of these considerations has already been described in several studies.[144–146] The results showed that the parameters of our system were dependent on the solvent composition to some extent, as indicated by a shift of T_{CP} from 33 °C in H_2O to 31 °C in PBS and to 25 °C in D_2O (**Figure 21**). The DLS data clearly showed the transformation from a free polymer in solution below the T_{CP} (size 4 nm) into two populations of particles, small particles (approx. 10 nm, population 1) and the larger assembled nanogel particles (30-50 nm, population 2). In PBS, an additional population of larger assemblies was observed above the T_{CP}. This result can be explained by the well-known aggregation behavior of particles with a hydrophilic shell, which tend to form larger clusters.[147]

To avoid the risk of introducing errors of magnitude, we represent our data obtained from dynamic light scattering as intensity-based size distributions (**Figure 21**). However, we have to keep in mind that the scattering intensity is directly proportional to the third power of the particle size. Therefore, larger particles scatter much more light than smaller particles, and thus, the intensity-based size distributions may be skewed towards larger particles. However, the smaller particles might constitute the majority of the sample mass.
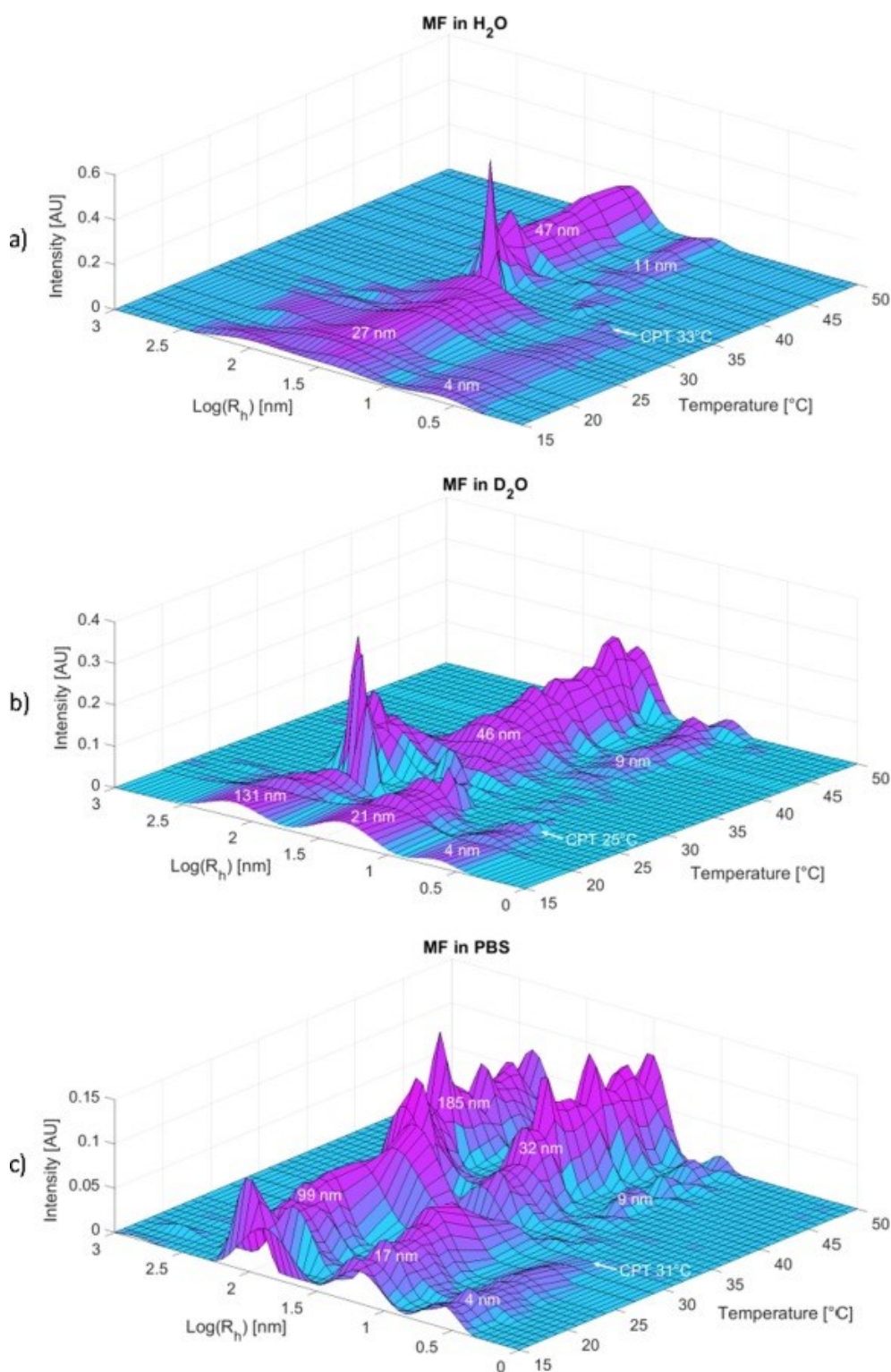
Figure 21. Temperature dependence of the intensity distributions of R_h obtained from DLS of our MF sample in (a) H_2O, (b) D_2O, and (c) PBS.

We further investigated the system by performing SAXS and SANS experiments. Below the T_{CP}, the calculated radius of gyration R_g for the population of free polymer chains was 12.07 ± 0.13 nm. Given the width of the DLS distributions and the difference between R_g and R_h, this was in good agreement with previous results. The generalized Gaussian coil function was used for the calculation of R_g, and the sample exhibited a Flory exponent

of approximately 0.52, which was in agreement with the SANS data and indicated that the copolymer existed in a good solvent with rather relaxed and well-solvated chains. The SAXS and SANS results above the T_{CP} provided information about the smaller population (population 1) in the DLS spectrum. With increasing temperature, the PDFEA chains in this population became less mobile, and the polymer collapsed into smaller assemblies. This behavior was observed from the obtained data by means of the evolution of the Flory exponent v of the present polymer coils with increasing temperature from $v = 0.560$ at 15 °C to $v = 0.368$ at 42 °C (**Figure 22**). This shift is in accordance with general polymer theory, which predicts a Flory exponent of $v = 0.6$ for polymer chains in good solvent and $v = 0.3$ for polymer chains in poor solvent. The overall behavior could be described as the formation of a loose sphere of radius 15 ± 1 nm with an internal structure represented by Gaussian chains. The radius of gyration of the internal coils was 1.3 ± 0.7 nm.
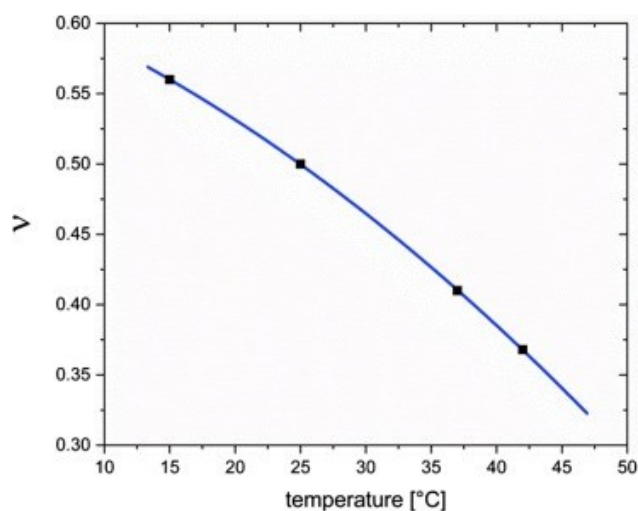
Figure 22. Evolution of the Flory exponent v with increasing temperature as calculated from SANS experiments.

Additionally, we used a concentration series measurement to calculate the excess scattering amplitude. Based on this measurement, we obtained the molar mass of the particles in population 1 as $M_{w,par} = 3 \cdot 10^6$ g·mol^{-1} and a swelling degree of almost 80%. Given the calculated $R_g = 15 \pm 1$ nm and $M_{w,par} = 3 \cdot 10^6$ g·mol^{-1}, we determined the number of aggregated particles in population 1 as $N_{agg} = 122$. Based on these results, the smaller population of particles (the minority population) was considered micelles. SANS and SAXS measurements are specific and precise for samples with one population and smaller particles in general. Therefore, we decided to characterize the larger population (population 2) with additional methods. However, the precise description of population 1 as micelles was vital to revealing the possible equilibrium between the formation of small particles and the higher molar mass nanogel assemblies.

3.2.3. Advanced NMR methods

To characterize our assembled nanogels (population 2) on the atomic level and the inner core of these particles, we used NMR experiments to determine the interaction between the monomers and the solvent.

First, we determined the loss of mobility of atoms after self-assembly by comparing the overall integrals of the corresponding peaks in the NMR spectrum with increasing temperature (**Figure 23**). The results showed that the mobility of the PDFEA atoms decreased

by approx. 45%, while only a marginal decrease in the mobility was observed for the hydrophilic PMeOx. This result suggested that the PDFEA blocks constituted a rather condensed part of the particles, while the PMeOx blocks maintained their flexibility and were solvated.
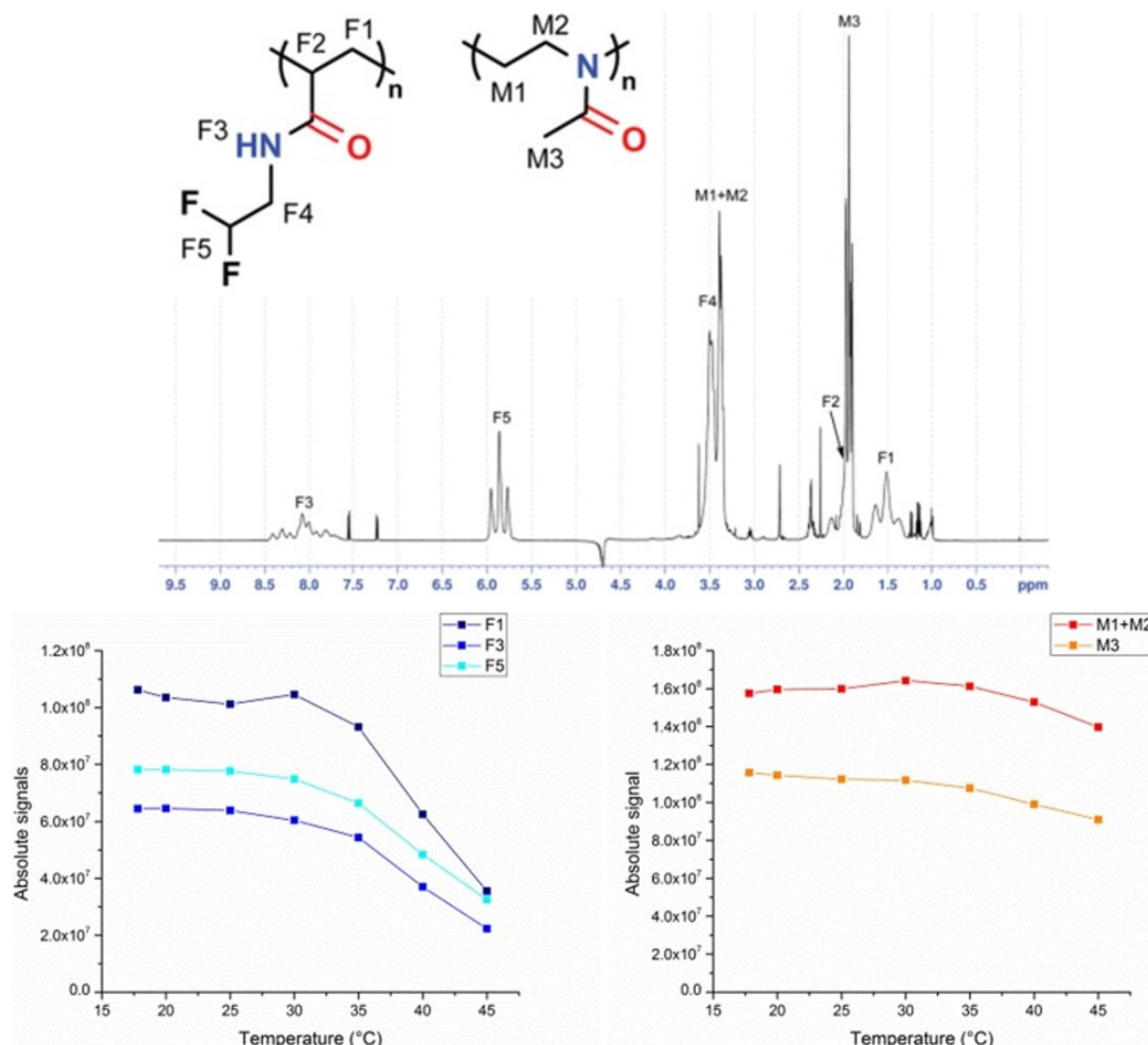
Figure 22. ^{1}H NMR spectral assignment of MF copolymer sample, acquired at 25 °C in H_2O/D_2O mixture (volume ratio 9:1) (top) and the NMR signal intensities as a function of temperature (bottom).

We investigated the inner structure of the particles using a NOESY experiment, which reveals the spatial proximity of hydrogen atoms that are separated by no more than 5 Å (**Figure 23**). The NOESY experiment allowed us to determine the interaction between the monomers and answer the question of whether the different types of monomers are in close proximity to or separated from each other. The NOESY signals of the protons in amide group F3 of the PDFEA block were compared with all the other protons of this block. The remarkable cross-peak between the F3 and F1/F2 protons supported the idea of hydrogen bonds between the amide groups of the PDFEA monomer. This arrangement brings sidechain end-groups closer to the backbone and allows for tight packing of thermoresponsive blocks

inside the particles. Finally, no interaction between the different copolymer blocks was observed. The sidechain interactions occurred exclusively between blocks of the same type.
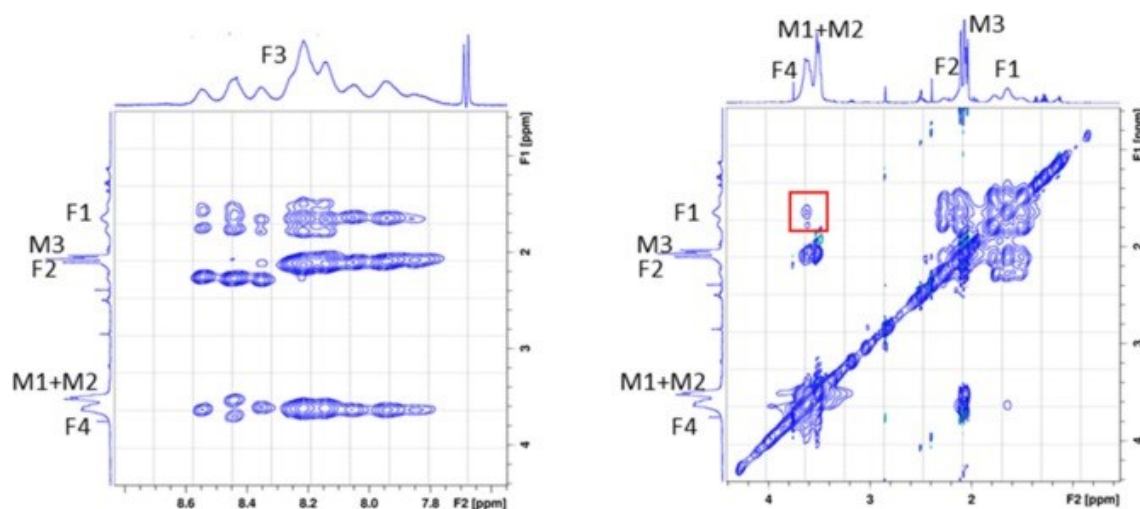
Figure 23. NOESY spectra of polymer MF in a H_2O/D_2O mixture (volume ratio 9:1).

Additionally, we measured the translational self-diffusion coefficients by means of a pulsed field gradient NMR method (DOSY). Our data showed that the diffusion coefficient of each block was slightly different; the measured diffusion constants of the PMeOx block were larger than those of the PDFEA block (**Figure 24**). The results supported the previous measurement results, where we prove the separation of the blocks within the particle and showed that the PMeOx retained its mobility inside the particle.
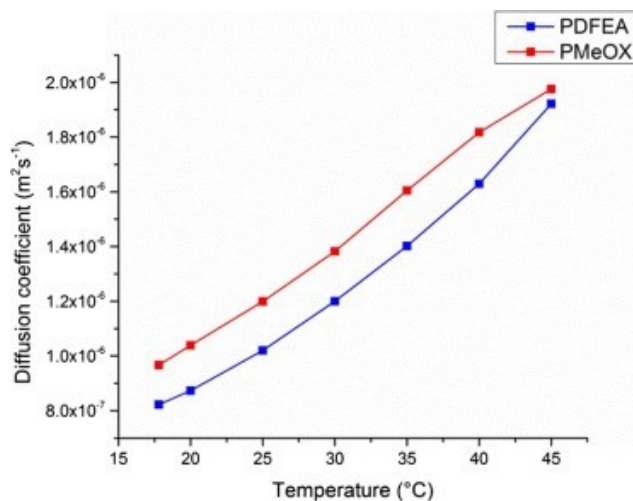
Figure 24. Self-diffusion coefficient of the particular blocks of the MF block copolymer at various temperatures.

Finally, we evaluated the ^{19}F NMR signal to confirm the suitability of the system for the ^{19}F MRI experiments. The obtained signal at approximately -123 ppm at different temperatures is shown in **Figure 25**. By heating the polymer from 20 to 45 °C, the polymer integral decreased due to polymer aggregation, but surprisingly, the signal decreased by only 20%. This result indicated that the effect of precipitation on the ^{19}F signal integral was much less significant than that observed in ^1H NMR (the signal decreased to 45% of its original

magnitude) in the same CF_2H moiety. Additionally, we observed a slight broadening at the signal foot, which suggested the presence of an additional signal component with short T_2 relaxation. This result indicated the presence of larger particles. The difference between fluorine and proton spectra can be explained by the relaxation properties of ^{19}F atoms in the CHF_2 group, which differ from the ^1H atom. Therefore, ^{19}F NMR spectroscopy may allow for the observation of larger polymer aggregates than ^1H NMR spectroscopy.
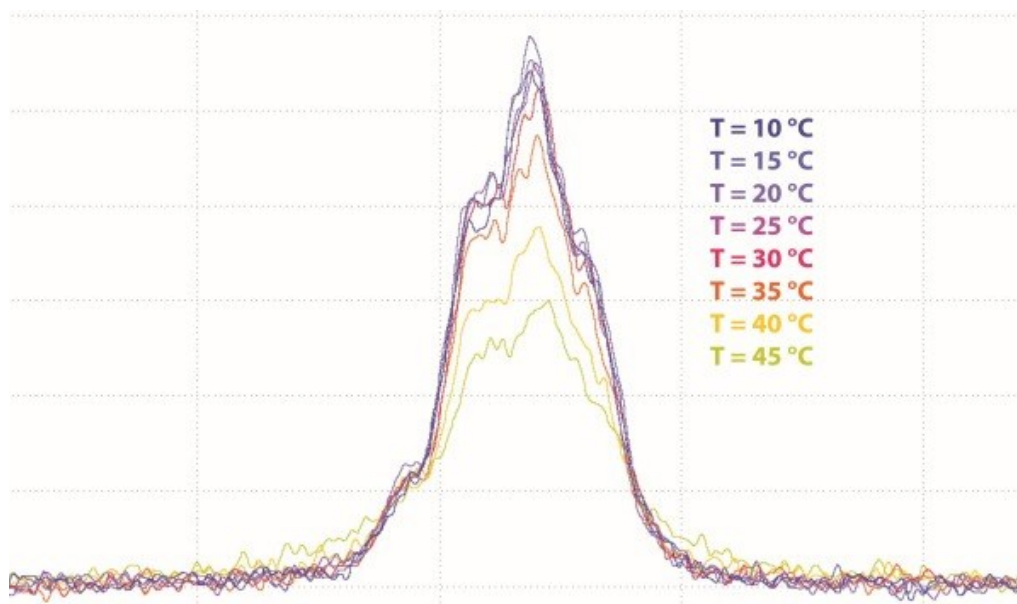
Figure 25. ^{19}F NMR spectra of the MF copolymer at different temperatures. Spectra at higher temperatures show increasing linewidth.

3.3. Thermo- and ROS-responsive theranostics using ^{19}F MR imaging

3.3.1. Polymer design, synthesis, and characterization

We modified the previous system based on the PHPMA-PDFEA diblock copolymer with a block ratio of 1:2 (in the previous study, polymer HF3) to enhance its possible application from an imaging tool to a smart theranostic system. The polymer was modified by incorporation of a functional amine moiety into a thermoresponsive block (**Scheme 2**). These functional groups can then be further used to tune the LCST behavior of the polymer resulting in stimuli-responsive degradation of the particles for possible drug release (DR). In our case, we modified the polymers with a ferrocene moiety using a reaction of the amine moiety with the NHS ester of ferrocenecarboxylic acid. Ferrocene is sensitive to oxidation: it can be oxidized in an oxidative environment by reactive oxygen species (ROS), which are abundant in inflamed tissues or malignant cells. The oxidation of neutral ferrocene to ferrocenium cations changes the solubility of the polymer in water (increases the hydrophilicity) and causes the degradation of the self-assembled polymers under physiological conditions.
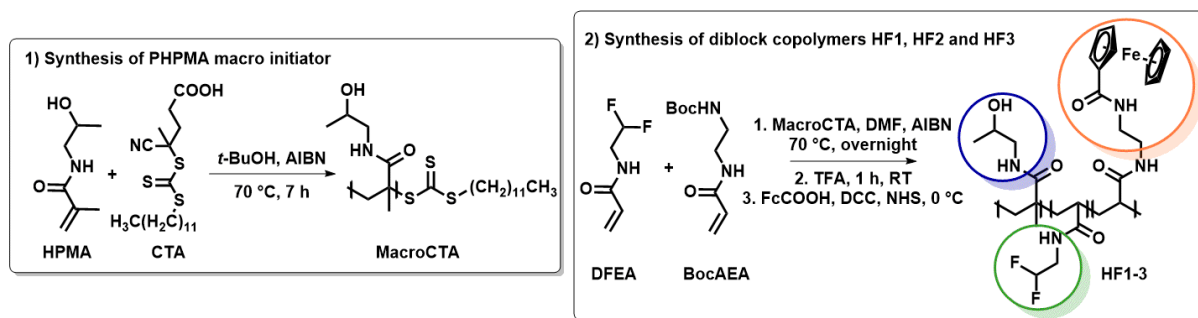
Scheme 2. Synthesis of the thermo- and ROS-responsive theranostic system *via* two-step RAFT polymerization.

The amphiphilic diblock copolymers containing the ferrocene moiety, poly[*N*-(2-hydroxypropyl)methacrylamide]-block-poly[*N*-(2,2-difluoroethyl)acrylamide-co-*N*-[2-(*N'*-ferrocenylamido)ethyl]acrylamide] (PHPMA-PDFEA-FcAEA) with a 1:2 ratio and various contents of HF1-HF3 (0.5 to 3.0 mol. %) were prepared by the same procedure as polymer HF3 in **Chapter 3.2.1.** by two successive RAFT polymerizations using 4-cyano-4-[(dodecylsulfanylthiocarbonyl)sulfanyl]pentanoic acid as the chain-transfer agent and α,α′-azoisobutyronitrile (AIBN) as the initiator (**Scheme 2**). The modification from the previous procedure was the incorporation of a small amount (0.5 – 3 mol. %) of the *N*-(2*N'*-Boc-aminoethyl)acrylamide monomer into the thermoresponsive PDFEA block as a statistical copolymer. Both RAFT polymerization and purification of the resulting polymers were conducted under the same conditions as in **Chapter 3.2.1.** After polymerization, the Boc- (*tert*-butyloxycarbonyl) protective group was removed under acidic conditions (10% trifluoroacetic acid) and then neutralized and purified by LH-20 Sephadex gel chromatography. The concentration of amino groups was determined using the reaction with 2,4,6-trinitobenzene-1-sulfonic acid and measured by UV-vis according to the literature.[148] Afterwards, the amino groups were reacted with the ferrocenecarboxy-*N*-hydroxysuccidimide ester to form the resulting polymer HF1-HF3 with different ferrocene contents.

The structure, purity of all copolymers and the ratio between two blocks were determined by ^{1}H NMR spectroscopy (**Figure 26**) using the signals of the protons of the CHF_2 moiety of PDFEA (δ = 5.9 ppm) and the proton in the CHOH moiety of PHPMA (δ = 3.9 ppm). Narrow molecular weight distributions (dispersity Đ ≤ 1.20) and molar masses (**Table 6**) of all copolymers were determined by size exclusion chromatography (**Figure 26**).

Table 6. Composition and physicochemical properties of the prepared polymers.

Polymer	Block ratio[a]	M_w[b] (kDa)	M_n[b] (kDa)	Đ (Mw/Mn)	Mol. % of Fluorine	Mol. % of ferrocene[c]
PHPMA	-	8.68	8.02	1.11	-	-
HF1	1:1.8	32.3	26.3	1.2	16.7	0.49 ± 0.12
HF2	1:1.9	29.1	26.0	1.1	18.0	0.80 ± 0.12
HF3	1:1.8	34.0	27.9	1.2	16.6	2.63 ± 0.66

Determined by ^{1}H NMR spectroscopy[a], SEC[b] or ICP-MS-MS[c].
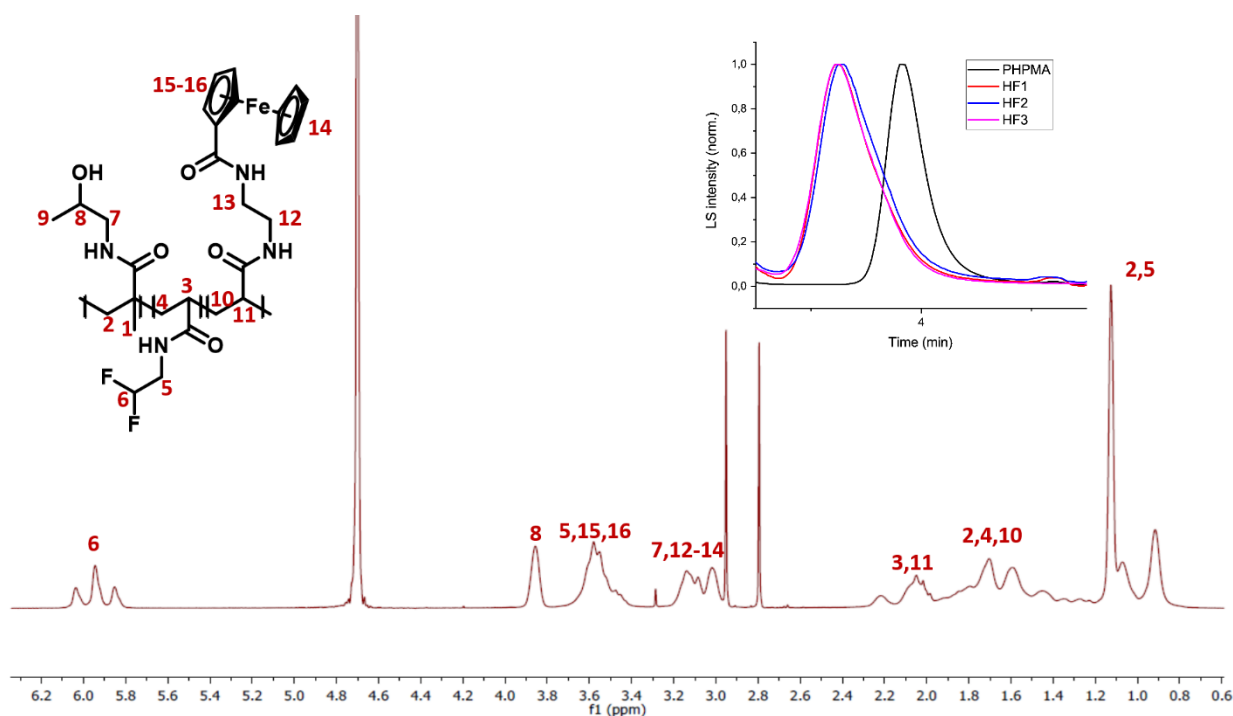
Figure 26. ^{1}H NMR spectrum of polymer HF2, measured in MeOD-d_4 (c_{pol} = 16.7 mg·mL^{-1}), NS = 32, D_1 = 30.00 s, acquired on a Bruker 400 MHz spectrometer. Size exclusion chromatography (SEC) traces of the prepared polymers PHPMA-b-P(DFEA-BocAEA) 1-3 using an HPLC Ultimate 3000 system (Dionex, Sunnyvale, USA) equipped with an SEC column (TSKgel SuperAW3000 150 × 6 mm, 4 μm) with a methanol and sodium acetate buffer (0.3 M, pH 6.5) mixture (80:20 v/v, flow rate of 0.6 mL min^{-1}) as the mobile phase.

3.3.2. Determination of the thermo- and ROS-responsive solution behavior

To determine the thermoresponsive self-assembly of the copolymers HF1-HF3 in an aqueous environment, we assessed the dependence of the hydrodynamic radii (R_h) on the temperature by DLS (**Figure 27,** gray trendline). In addition to the DLS measurements, transmission electron microscopy (TEM) images of one of the copolymers (HF1) at two different concentrations were obtained (**Figure 28**). The measurements were performed in a phosphate-buffered saline (PBS) solution (pH 7.4) as the simplest biologically relevant model in the temperature range of 10 to 50 °C. The results revealed the formation of spherical polymeric nanoparticles very similar to the previous system (**Chapters 3.1.** and **3.2.)**; therefore, additional methods to determine the structure were not necessary. In general, the added ferrocene moiety did not significantly influence the self-assembly behavior of these polymers. The diameter (R_H) of the particles was approximately 30 to 40 nm, and the cloud point temperature (T_{CP}) of all three polymers was 34 °C. By comparison, the cloud point temperature of the corresponding polymer without ferrocene in **Chapter 3.2.** was lower, probably due to the higher content of the thermoresponsive PDFEA (the ratio was higher than 1:2). The initially increased R_H (~ 80 nm) corresponded to the previously mentioned formation of particle clusters.[147]

To determine the ROS-responsive behavior, we oxidized the ferrocene moiety and measured the size distributions in response to temperature changes by DLS (**Figure 27**, red points).

The oxidation of ferrocene can be realized in many possible ways. Macroscopically, the process can be observed as a color change from yellow-orange to greenish to blue.[149,150,151,152] However, for our intended application, we simulated the conditions of tumor tissue for *in vitro* measurements with hydroxyl radicals and acidic conditions (pH 5.0), representing the well-known environment in most tumor tissues.[49] For this purpose, we measured the samples in acetate buffer (pH 5.0) with the added hydrogen peroxide (0.003 to 0.01 vol. %) and a catalytic amount of $CuCl_2 \cdot 2H_2O$ to accelerate the oxidation (Fenton oxidation reagent[153]). The data showed that all three polymers could not generate particles in the oxidized state at the measured temperatures. Finally, we also titrated a hydrogen peroxide solution of our sample under neutral conditions to determine the concentration of H_2O_2 at which the particles decompose. A concentration of 0.1% H_2O_2 was sufficient for the polymer with the lowest concentration of ferrocene to decompose, indicating the high sensitivity of the system to even a slightly oxidative environment. Generally, the particles can switch between self-assembled and disassembled states upon oxidation under physiological conditions; therefore, the polymeric particles could potentially release encapsulated drugs into ROS-rich tissues.
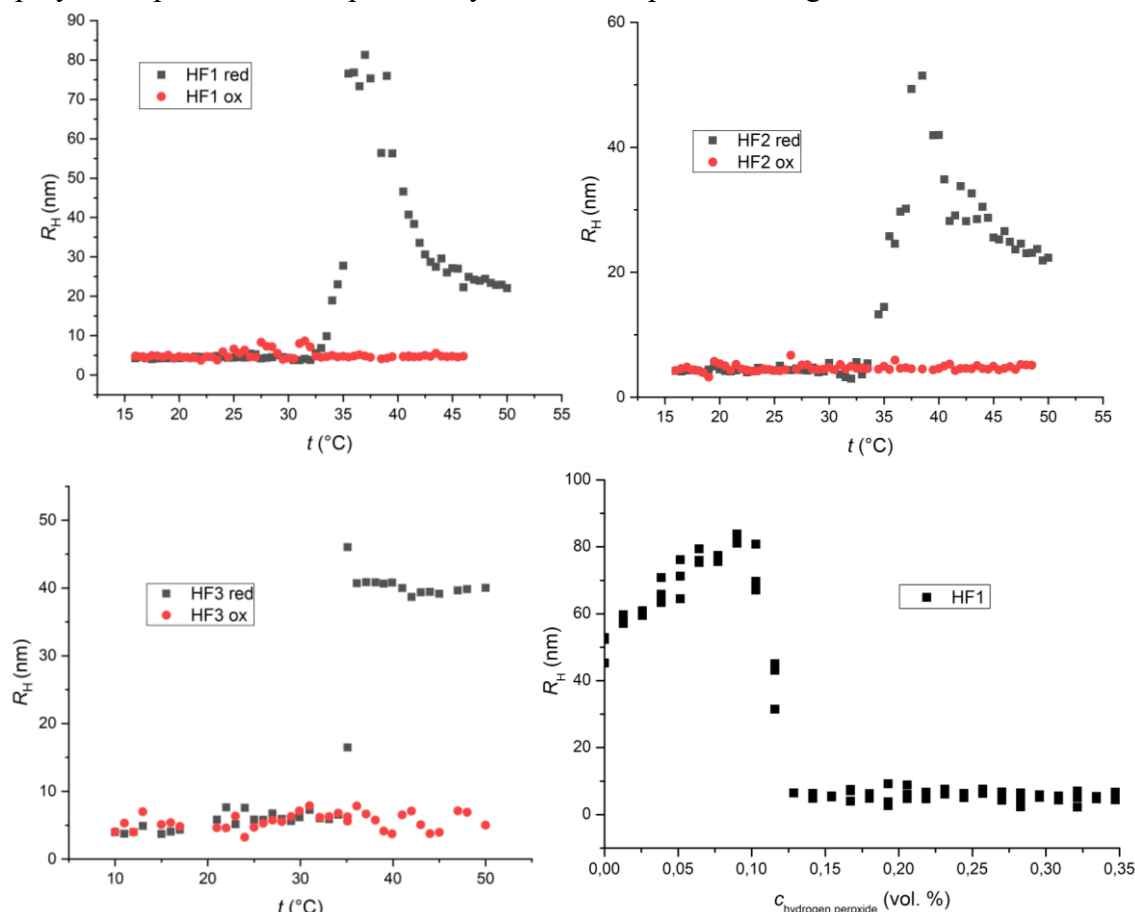
Figure 27. DLS determination of the particle size as a function of temperature. Graphs A), B) and C) show the thermoresponsive behavior of polymers HF1, HF2 and HF3 in their oxidized and nonoxidized forms. The gray points show the particle formation in the neutral conditions (PBS), where the ferrocene moiety is in the reduced state. The red trendline shows the simulated condition of tumor tissue, in which ferrocene is oxidized. Graph D) shows the titration of particles based on polymer HF1 in neutral conditions with H_2O_2 to simulate the oxidative environment and particle degradation with increasing concentrations of H_2O_2.
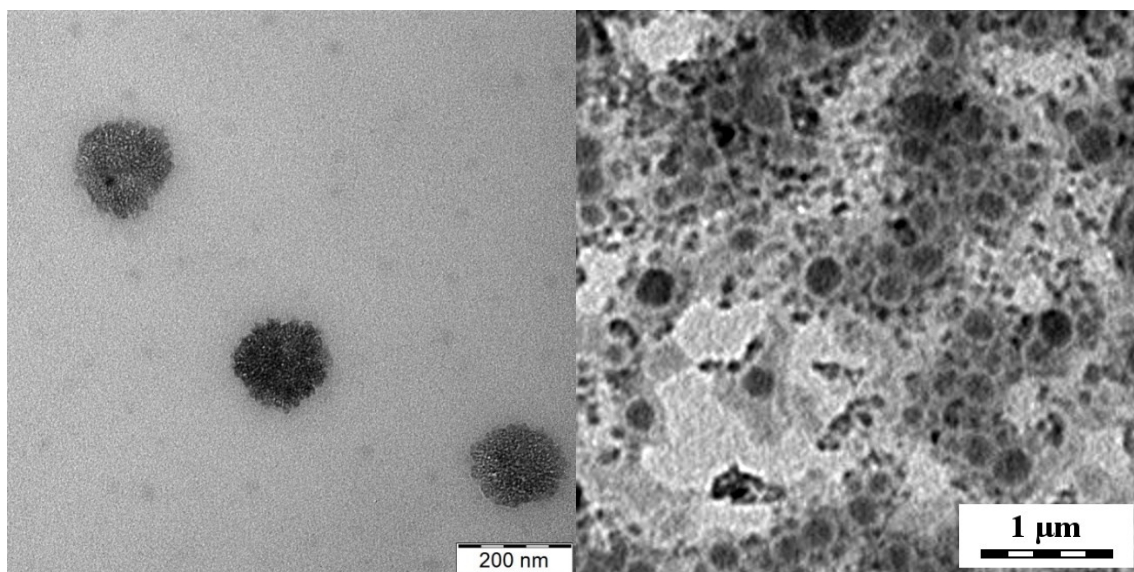
Figure 28. TEM micrograph of polymer HF1 particles. Left: polymer concentration 1 mg·mL^{-1}, right: polymer concentration 10 mg·mL^{-1}.

3.3.3. ^{19}F relaxation, MRS and MRI

The suitability of a contrast agent to be used in routine ^{19}F MRI techniques is highly dependent on several key parameters. First, it is beneficial if the ^{19}F atoms are chemically and magnetically equivalent (this ensures a very intense and narrow peak of the ^{19}F signal); their concentration should be as high as possible. Second, the choice of applicable ^{19}F MRI scanning techniques and therefore the quality of the image is highly dependent on the T_2 and $T_2{}^*$ relaxation properties of the fluorine atoms. For purposes of routinely used MRI scanning techniques (*e.g.*, RARE and FLASH),[154] the T_2 should exceed 10 ms.[29] Short T_2 relaxation requires the use of particular sequences, such as ultrashort echo time (UTE)[38] or zero echo time (ZTE)[38] sequences, that are very hardware-demanding techniques.

It should be noted that these parameters can change rather drastically under different conditions; therefore, they should be measured under conditions closely resembling the *in vivo* environment. It is known that the aggregation of polymers may lead to a significant decrease in the ^{19}F signal, partially due to the significantly faster T_2 relaxation times in aggregates,[64] ultimately decreasing the intensity of the signal from the contrast agent. However, we did not observe any significant ^{19}F signal broadening as a result of aggregation, consistent with previous reports of similar materials.[105] Therefore, we measured the T_1 and T_2 relaxation times at 37 °C in 150 mM PBS buffer (pH 7.4) to simulate physiological conditions using the standard ^{19}F NMR instrument.[155]

The results showed an expected decrease in the relaxation times with increased ferrocene content (**Table 7**). The T_2 was above the threshold value for the ^{19}F MRI sequences for polymer HF1 and HF2 ($T_2 \approx 17$ ms), indicating their suitability for currently used ^{19}F MRI scanners.

Table 7. T_1 and T_2 relaxation times of ^{19}F of all three polymer solutions in a 9.4 T field at 37 °C in PBS-D_2O buffer (150 mM, pH 7.4). All points were fitted with $R^2 \geq 0.998$.

Polymer	T_1 (ms)	T_2 (ms)
HF1	460 ± 4.0	16.9 ± 0.6
HF2	458 ± 6.0	11.0 ± 0.4
HF3	395 ± 10.0	7.0 ± 0.6

Based on our results, we decided to use polymer HF1 for further measurements due to its well-defined self-assembly properties[65] and its suitable T_1 and T_2 relaxation times for ^{19}F MRI purposes. However, our results indicated that the ferrocene content might differ considerably without severely changing the T_{CP} or MR properties (the particle size can change).

Subsequently, various concentrations of the polymer with the best MR relaxation properties (HF1) were dissolved in a 150 mM PBS solution. The phantom measurement revealed a ^{19}F MRS signal change upon changing the temperature. The signal was measured at room temperature (24 °C, red trace) and at body temperature (37 °C, blue trace). No significant signal decrease was observed upon heating (and particle formation), which is ideal for ^{19}F MRI purposes.
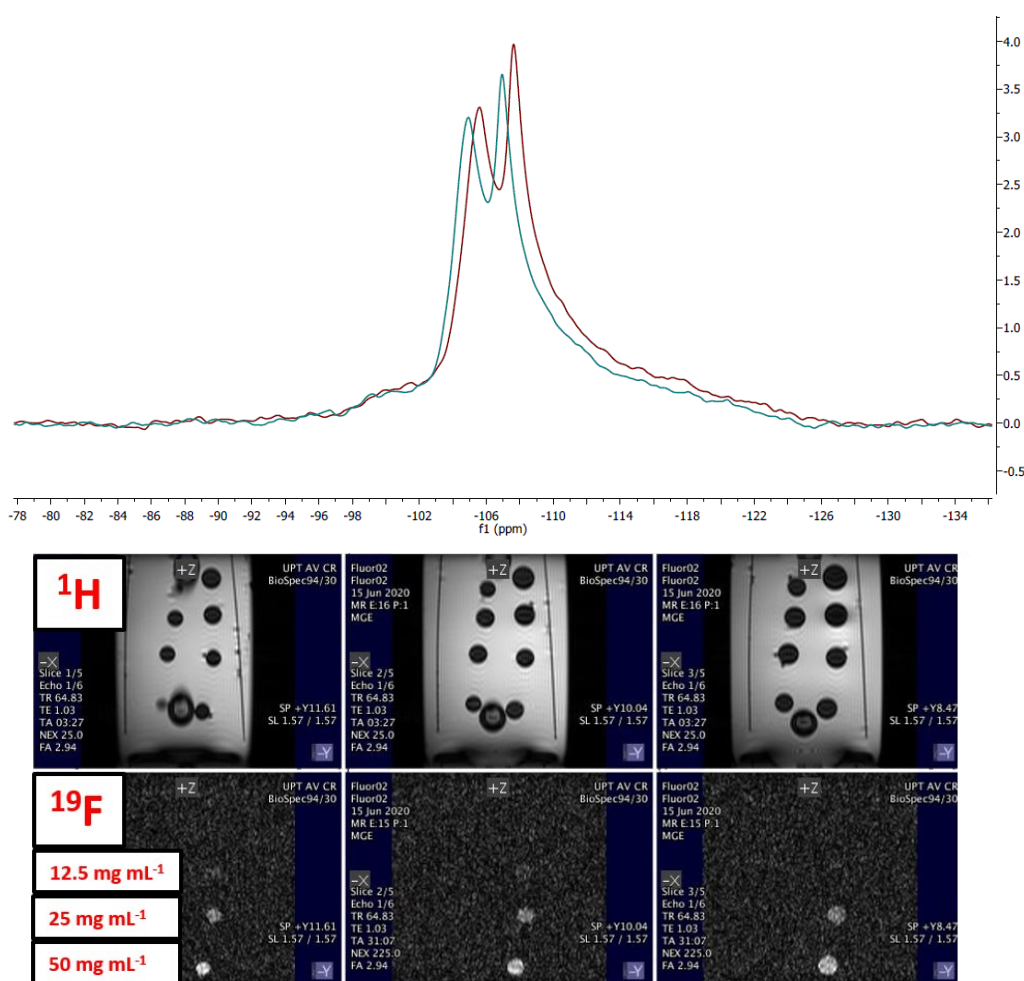

Figure 29. Top: ^{19}F MRS spectrum of the HF1 polymer with trifluoroacetic acid as the chemical shift reference at 24 (red trace) and 37 °C (blue trace). Bottom: *In vitro* phantom ^1H MR and ^{19}F MRI images at different polymer concentrations.

3.3.4. Biocompatibility and drug release study

The selected polymer HF3 was further analyzed by means of a cytotoxicity experiment with several relevant cell lines. Polymer HF3 did not decrease the viability of any of the studied cells below 70% (**Figure 30**); the noncytotoxicity of the polymer towards all the tested cell lines within the concentration range used ($0.125 - 2.0$ mg·mL^{-1}) was confirmed.
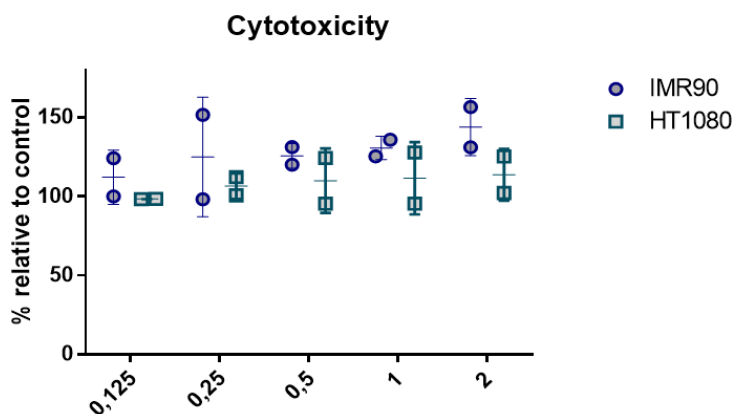

Figure 30. Viability of different cells (IMS90 and HT1080) with increasing concentrations (0.125-2.0 mg·mL^{-1}) of polymer HF3.

The developed system should exhibit the ability to release drugs in the presence of ROS; therefore, we decided to further analyze this mechanism in an *in vitro* study with perfectly spheroidal cancer cell clusters called "spheroids". These clusters are well known to create their own ROS-rich and acidic microenvironment due to solid tumor-like hypoxia. In this study, we monitored the proliferation of cancer cells in the presence of a polymer formulation with a cytostatic drug (doxorubicin, DOX) or with an inhibitor of proliferation (GSK-429286). The perfectly symmetrical 3D structure of the cancer cell clusters allowed us to quantify the effect of the compound as well as its distribution with high precision.

To provide comprehensive data, we first determined the polymer's ability to encapsulate hydrophobic drugs (DLs) and determined the concentration limit for the particle assembly.[156] The DL study was carried out by determining the drug-loading factor f_{DL} and entrapment efficiency factor f_{EE}, calculated with equations (14) and (15).

$$f_{DL} = \frac{m_{drug,II}}{m_{polymer} + m_{drug,II}} \cdot 100\% \tag{14}$$

$$f_{EE} = \frac{m_{drug,II}}{m_{drug,I}} \cdot 100\% \tag{15}$$

where $m_{polymer}$ is the mass of the polymer, $m_{drug,I}$ is the mass of drug added to the system (cumulative mass of the drug within both the aqueous phase and polymer phase), $m_{drug,II}$ is the mass of the drug in the formulation, and m_{aq} is the mass of the aqueous phase. The DL was measured for three different concentrations of rifampicin in the presence of polymer (1.0 mg·mL^{-1} in 150 mM PBS buffer) at 37 °C by ultracentrifugation (**Table 8**). The DL was measured for four different concentrations of doxorubicin (DOX) and inhibitor (GSK 429286) in the presence of polymer (1.0 mg·mL^{-1} in 150 mM PBS buffer, pH = 7.4) at 37 °C

by ultracentrifugation. The lowest concentration of the drug measured (0.025 mg of the drug for 1.0 mg of polymer) resulted in $f_{EE} \approx 93.75\%$ (DOX) and $f_{EE} \approx 72.6\%$ (GSK 429286), which corresponded to the approximate concentrations used in the following *in vitro* measurements, proving efficient drug encapsulation during these experiments.

Table 8. Data obtained from the DL study for polymer HF1 at a concentration of 0.1% m/v in PBS buffer, pH 7.4, and with DOX/GSK 429286 as the drug at concentrations of 0.10, 0.05 and 0.025 mg·mL^{-1}.

Doxorubicin			
$m_{drug,I}$ (mg)	0.10	0.05	0.025
$m_{drug,II}$ (mg)	0.03	0.03	0.02
f_{EE} (%)	31.7	62.8.	93.8
f_{DL} (%)	3.09	3.04	2.29
GSK 429286			
$m_{drug,I}$ (mg)	0.10	0.05	0.025
$m_{drug,II}$ (mg)	0.03	0.02	0.02
f_{EE} (%)	32.5	37.5	72.6
f_{DL} (%)	3.14	1.84	1.78

The lowest concentration of the drug measured (0.25 mg of rifampicin for 1.0 mg of polymer) resulted in an f_{EE} ~71%. The critical association concentration (CAC) was measured using the same method as in **Chapter 3.1.**, using Nile red (NR) as the fluorescent probe. The fluorescence spectra of the samples were recorded ($\lambda_{ex}/ \lambda_{em}$ = 485/636 nm) and plotted as a function of polymer concentration. The CAC was determined as the intersection between two fitted linear functions and was 15.7 mg·L^{-1}.

After determining the DL and CAC, we performed a drug release study. First, an experiment with the cytostatic drug DOX was performed to determine the distribution of the drug in the 3D spheroids by fluorescence. The distribution of the drug can provide information about the availability of the drug encapsulated in the polymeric particle (**Figure 31**) in comparison to the free drug. The DOX distribution was determined by directly adding doxorubicin (at a final concentration of 10 µM DOX) to the control medium or the medium with 0.2 mg·mL^{-1} of polymer after embedding in 3D collagen; the resulting micrographs were obtained after 3 h. The results showed that the low-molecular weight drug could easily penetrate through the clusters of cells into the core of the spheroids; however, the presence of the drug encapsulated within the nanoscale particles appeared to have no impact on the distribution of cytostatic drugs. In conclusion, our results suggested that the drug penetration was on the same scale for the DOX-polymer formulation and free DOX, which was used as a control measurement.

Free DOX   **Polymer + DOX**
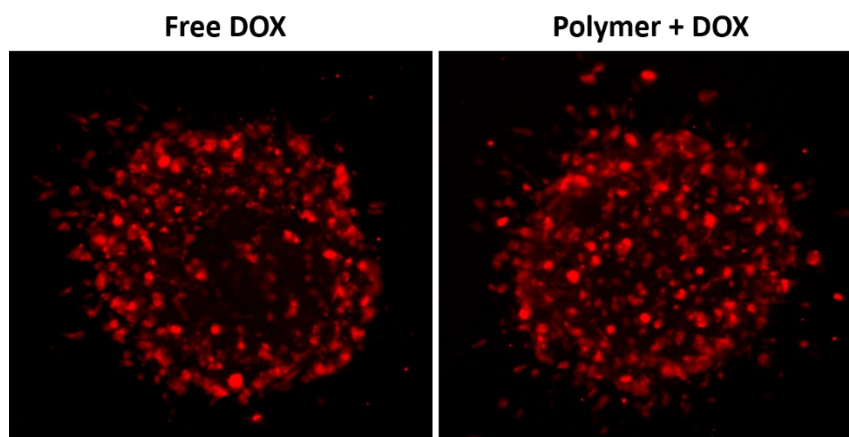
Figure 31. Micrographs showing the distribution of free DOX (left) and DOX-polymer formulation (right) in the 3D spheroidal cluster of cancer cells. After 3 h, the doxorubicin-associated fluorescence in the spheroids was imaged by a 10x objective using the Thunder Imager configuration of a Leica DMi8 microscope (excitation 470 nm). For each spheroid, the image represents a maximum projection of 100 stack images.

The second experiment was performed with cell proliferation inhibitor (GSK-429286) to evaluate the efficiency of DR by comparing the activity of the free inhibitor and the inhibitor-polymer formulation (**Figure 32**). The experiment was performed with two different concentrations of inhibitor (1 and 10 µM inhibitor solution) with duplicates to provide a statistical distribution (**Figure 33**). Images of the spheroids were taken immediately after embedding into the medium and 24 h after embedding. Four different cultivation media were prepared. The first one was a control medium containing 1 µL·mL^{-1} DMSO to ensure that DMSO did not affect the proliferation (this additional DMSO content is further addressed as DMSO); the hydrophobic inhibitor has to be applied as a DMSO solution. The first control medium allowed us to observe and quantify the free proliferation of spheroids for comparison. The second cultivation medium was a control medium containing free inhibitor (applied as a DMSO solution at a final inhibitor concentration of 10 µM) to observe and quantify the relative inhibition of the proliferation by the free inhibitor. The third medium was a control medium containing the polymer (polymer concentration 0.2 mg·mL^{-1} in DMSO) to establish any possible impact of the polymer on the experiment. Finally, the last medium contained the inhibitor-polymer formulation (polymer concentration 0.2 mg·mL^{-1} with 10 µM inhibitor), for which the relative inhibition of proliferation was quantified and compared to the control media. After 24 h, the control groups without the inhibitor proliferated naturally; neither the free polymer nor DMSO affected the proliferation. Compared to the control groups, the results showed that the inhibition of the spheroid growth in the group of the free inhibitor and inhibitor-polymer formulations occurred to the same degree at both tested inhibitor concentrations (**Figure 32** and **33**). This result implied that the polymer effectively released the inhibitor under the tested conditions, which mimicked the conditions in the cancer cell environment.
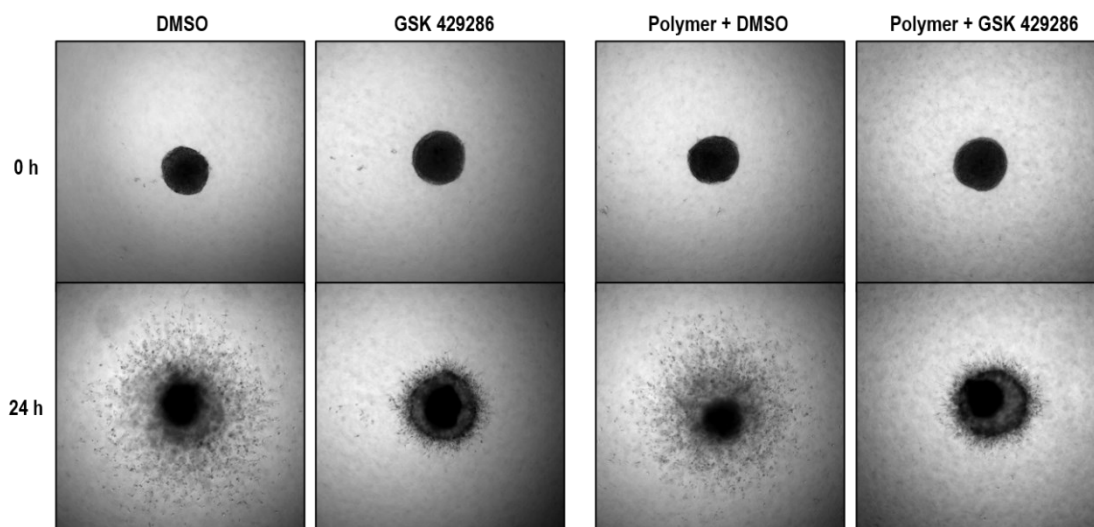
Figure 32. *In vitro* spheroid proliferation study. Left: Control medium with DMSO and control medium containing free inhibitor GSK-429286 (10 µM). Right: The polymer solution (0.2 mg·mL^{-1} with DMSO) and medium with inhibitor-polymer formulation (polymer concentration 0.2 mg·mL^{-1} with 10 µM concentration of inhibitor). Images were taken using the microscope immediately after immersion into the medium and 24 h after immersion.
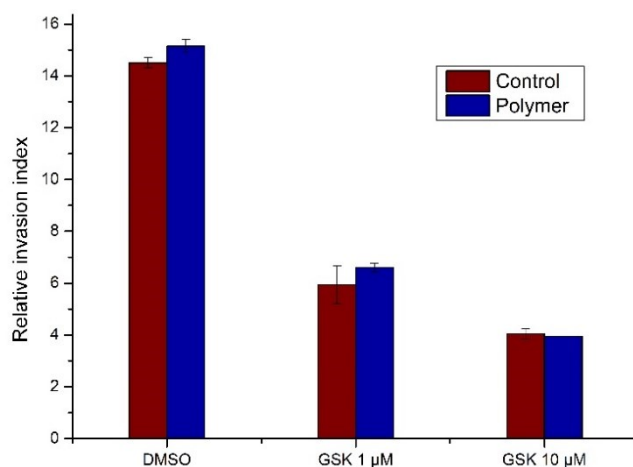
Figure 33. Evaluated relative invasion index of the spheroids in different media. The gray trend corresponds to the control media (medium containing DMSO and medium containing free inhibitor GSK-429286 at concentrations of 1 or 10 µM), compared to the blue trend, corresponding to the polymer solutions (medium with free polymer and DMSO, medium containing polymer with encapsulated inhibitor GSK-429286 at concentrations of 1 or 10 µM).

3.4. Thermo- and pH-responsive injectable implants with the ^{19}F MR imaging modality

3.4.1. Polymer design, synthesis, and characterization

We prepared random thermoresponsive copolymers composed of three different monomers: thermoresponsive *N*-(2,2-difluoroethyl)acrylamide (DFEA), hydrophilic *N*-(2-hydroxyethyl)acrylamide (HEAM) and pH-responsive *N*-[3-(*1H*-imidazole-1-yl)propyl]acrylamide (ImPAM), copolymerized *via* RAFT polymerization (**Scheme 3**). While the *N*-(2,2-difluoroethyl)acrylamide units ensured the ^{19}F MRI contrast and LCST properties of the copolymers, the pendant imidazole moieties ensured their pH-responsive character and provided the ability to tune the LCST at different pH values (an example of the LCST switch of one of prepared polymers is shown in **Figure 11**). Finally, the *N*-(2-hydroxyethyl)acrylamide units were used to modulate the polymer hydrophilicity. These polymers can be applied as injectable implants (depots with an encapsulated drug) for slow drug release (DR) *in situ* and accelerated release at lower pH (tumor, inflammation). Recently, an injectable fluorinated thermo- and pH-responsive polymer with a high concentration of fluorine for use as universal ^{19}F MRI tracer was reported in a communication.[66] However, the *in vivo* redissolution/bioerosion of the reported polymer implant under physiological conditions ranged from slow to virtually nonexistent, which limits its possible biomedical applications. Therefore, we introduced the hydrophilic monomer at various ratios to obtain polymeric implants with different dissolution rates while overcoming the main issue of biocompatibility observed in the previous system. The dissolution rates were summarized in a detailed pharmacokinetic study, which leads us to suggest a variety of possible applications for this type of system.
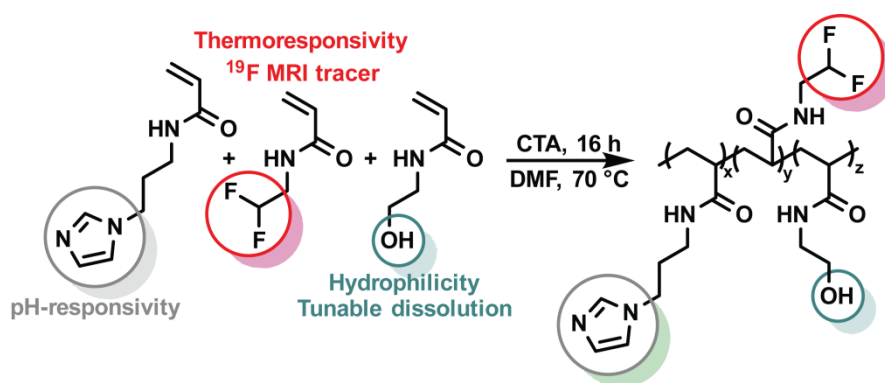
Scheme 3. Synthesis of thermoresponsive random copolymers as a theranostic for ^{19}F MRI *via* RAFT polymerization.

Copolymers poly{*N*-(2,2-difluoroethyl)acrylamide-*co*-*N*-[3-(*1H*-imidazol-1-yl)propyl]acrylamide-*co*-*N*-(2-hydroxyethyl) acrylamide} (P(DFEAM-ImPAM-HEAM)) were prepared by reversible addition-fragmentation chain-transfer (RAFT) copolymerization with the corresponding monomers and 4-cyano-4-(dodecylsulfanylthiocarbonyl)sulfanyl]pentanoic acid as the chain-transfer agent (CTA) (**Scheme 3**). The RAFT copolymerization was performed at 70 °C in an argon atmosphere overnight using dry DMF as the solvent. Afterward, the resulting copolymers were purified using the same procedure as all previously described

polymers. The copolymers were prepared with five different monomer unit ratios (**Table 9**, copolymers F1-F5) and compared to polymer F0 from a previous study.[66] The structure, purity of all copolymers and the ratio between particular monomers were determined by ^{1}H NMR spectroscopy (**Figure 34**) and the HSQC method (**Figure 35**). Narrow molecular weight distributions (dispersity $Đ \leq 1.20$) and molar masses (**Table 9**) of all copolymers were determined by size exclusion chromatography (**Figure 34**).

Table 9. Composition and physicochemical properties of the prepared polymers.

Polymer	Polymer composition[a] (mol. %)			Fluorine content (wt. %)	M_w (kDa)[b]	(M_w/M_n)
	DFEA	ImPAM	HEAM			
F0[66]	92	8	0	25.8	41.9	1.10
F1	88	7	5	24.8	37.8	1.12
F2	84	8	8	23.6	37.9	1.09
F3	76	9	15	21.4	32.8	1.19
F4	70	9	21	20.2	43.7	1.05
F5	58	9	33	16.3	47.4	1.09

[a]Determined by ^{1}H NMR spectroscopy, [b]and SEC.
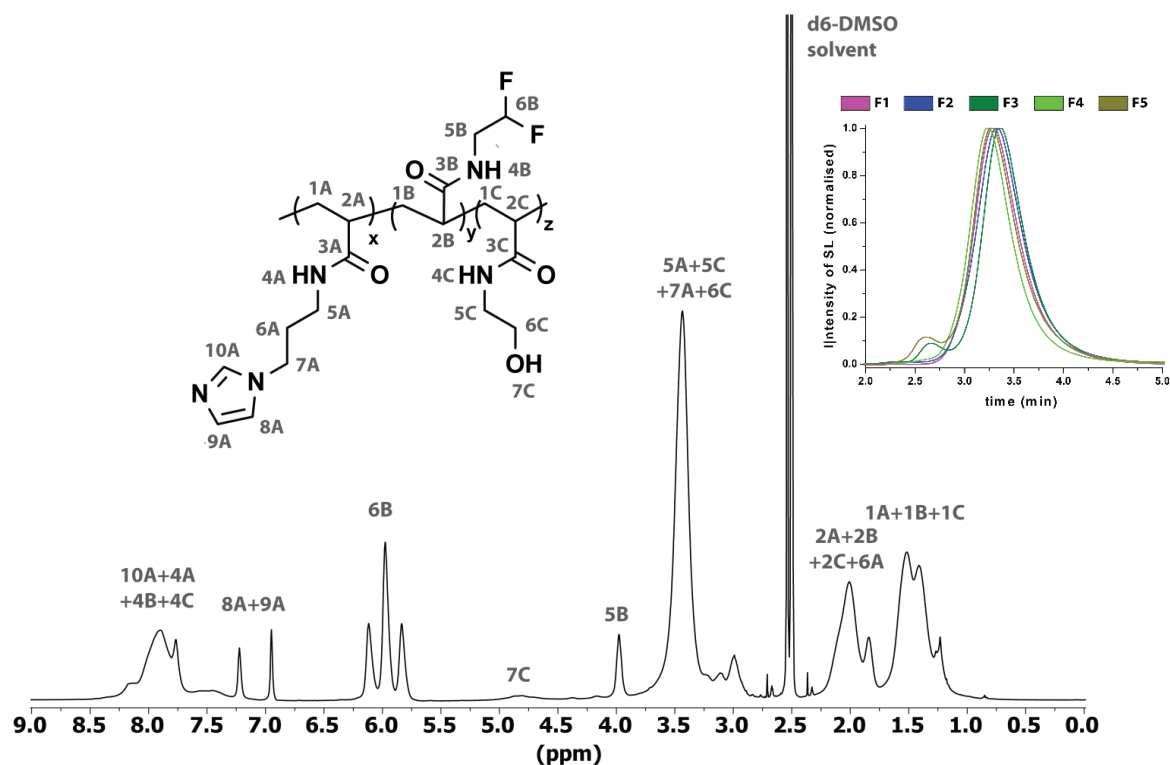
Figure 34. ^{1}H NMR spectrum of polymer F2, measured in DMSO-d_6 (c_{pol} = 0.5 mg·mL^{-1}), NS = 32, D1 = 30.00 s, acquired on a Bruker 300 MHz spectrometer. Size exclusion chromatography (SEC, top right) traces of the prepared polymers F1-F5 using an HPLC Ultimate 3000 system (Dionex, Sunnyvale, USA) equipped with an SEC column (TSKgel SuperAW3000 150 × 6 mm, 4 μm) with a methanol and sodium acetate buffer (0.3 M, pH 6.5) mixture (80:20 v/v, flow rate of 0.6 mL min^{-1}) as the mobile phase.
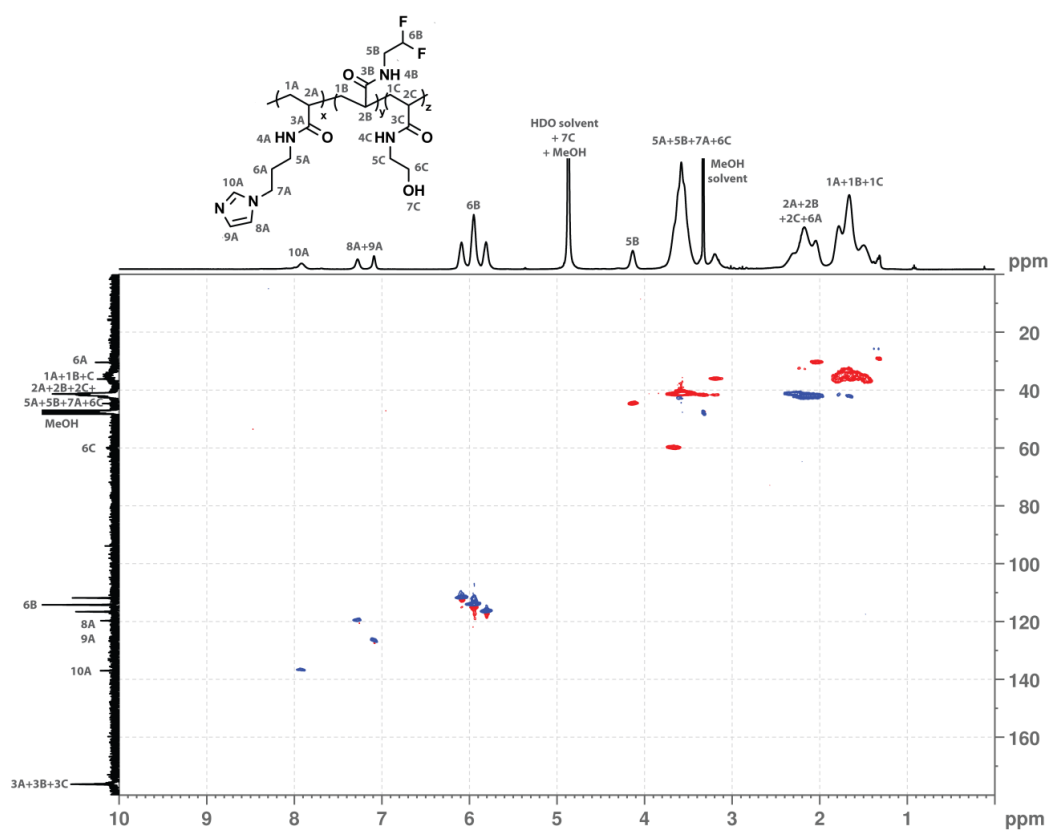
Figure 35. HSQC-edit of copolymer F1 (25 mg in DMSO-d_6, 550 µL), NS = 2, D1 = 1.50 s, 2048 to 512 points in spectrum; external projection was used. Red traces correspond to CH_2 groups, and blue traces correspond to CH groups.

3.4.2. Thermo- and pH-responsivity

The intended mechanism of polymer administration is shown in the schematic illustration in **Figure 36**. Polymers at lower pH values of ≈ 5.0 (biologically well-tolerated) should dissolve in water, which allows for the injection of their aqueous solution into the body without any obstruction of the needle during administration. After administration, the solution is exposed to the interstitial fluid within the tissue with the pH value 7.4, which has high buffering capacity immediately increasing pH of the injected liquid to neutral.[157,158] If the polymer is coadministered with a hydrophobic drug, it remains physically entrapped (or dissolved in this separated phase), forming a polymeric drug-containing depot. Additionally, it has already been mentioned that the pH in certain tissues is lowered (*e.g.*, tumor tissues tend to have pH ≈ 6 due to the Warburg effect or in inflammation), which could accelerate the local release of the coadministered compound.
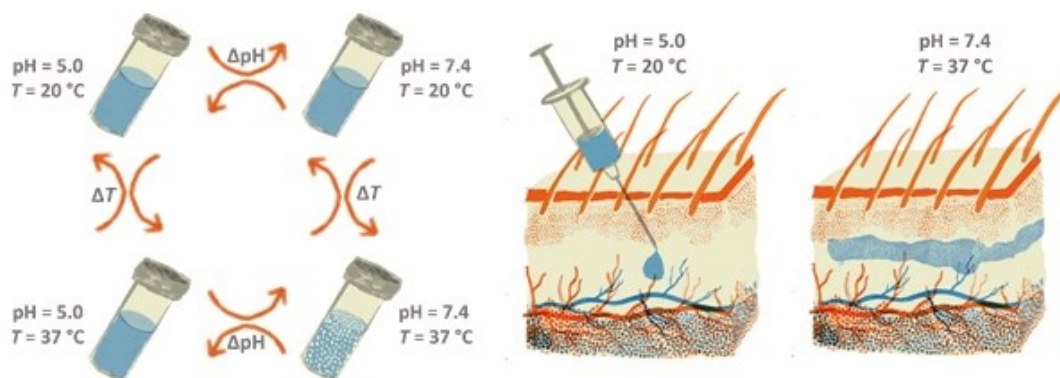
Figure 36. (Left) Illustration of the pH-dependent LCST behavior of the proposed polymers. (Right) Schematic illustration of ^{19}F MRI contrast implant formation.

The LCST behavior of the prepared polymers was evaluated by turbidimetry at physiological pH (pH 7.4) and acidic pH (pH 5) (**Figure 37**, **Table 10**). Large differences in the LCST (**Table 8**) were observed when switching from physiological to acidic conditions, which is beneficial for the intended application. In general, the prepared polymers generated precipitated implants under physiological conditions and dissolved at pH 5.0. With increasing amounts of hydrophilic *N*-(2-hydroxyethyl)acrylamide monomeric units, the T_{CP} increased. The results showed that the polymers with T_{CP} values within the required range were the copolymers F1, F2, and F3. Even though F3 precipitated at approximately 37 °C at pH 7.4, this temperature was sufficient for the formation of precipitated implants. The phase transition of most hydrophilic copolymers (F4, F5) occurred within a temperature range much higher than body temperature, and these copolymers were therefore not suitable as injectable implants; however, polymer F4, with the fastest expected dissolution rate, was used as a reference material.

Table 10. Corresponding cloud point temperatures, T_{CP}, of the synthetized copolymers F0-F5 in aqueous environment at two different pH values.

Polymer	T_{CP} (°C)	
	pH 7.4	**pH 5.0**
F0[66]	22	43
F1	27	60
F2	31	71
F3	37	≈ 85
F4	54	≈ 85
F5	≈ 67	≈ 85
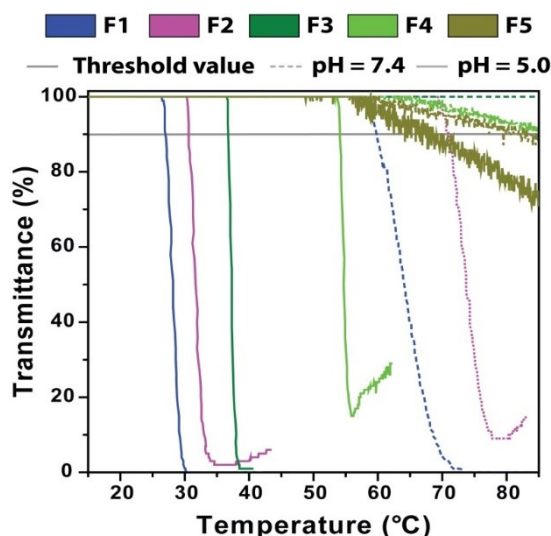
Figure 37. Transmittance ($\lambda = 600$ m) of the polymer solutions F0-F5 ($c_{pol} = 5.0$ mg·mL^{-1}) as a function of temperature at pH 5.0 or 7.4. The gray horizontal lines refer to transmittance levels of 30% and 70% and were omitted for clarity.

3.4.3. ^{19}F NMR spectroscopy and relaxation properties of the copolymers

The chemical shifts of all the described copolymers range from -125 ppm –124 ppm, which is a relatively unique chemical shift among the common ^{19}F MRI tracers (*e.g.*, perfluorocarbon usually has chemical shifts –80 to –70 ppm). This enables the possible simultaneous measurement of two (or more) different fluorinated tracers if required. Moreover, the chemical shift is far from the isoflurane peak, which is used as an anesthetic. Nevertheless, the most important information about our system and its suitability for ^{19}F MRI purposes are the T_1 and T_2 relaxation times and changes in the signal as a result of aggregation. The T_1 and T_2 relaxation times were measured with a 4.7 T MRI scanner at 37.0 °C and pH 5.0 and 7.4 (**Figure 38**). Both T_1 and T_2 in the given magnetic field (4.7 T) were approximately 380 ± 50 ms (they were equal within the margin of the experimental error) for all polymers in both their nonaggregated (pH = 5.0) and aggregated forms (pH = 7.4). These results showed that the polymers had exceptionally good relaxation properties, with great potential as very promising, highly sensitive tracers.

The effect of polymer aggregation on the signal was further investigated with 400 MHz NMR spectroscopy (9.4 T). The ^{19}F NMR signal was measured in three different solutions, PBS (pH 5.0 and 7.4), FBS or EMC gel, at two different temperatures, 20.0 °C and 37.0 °C. Afterward, the integrals and amplitudes of the polymer signals under different conditions were compared (**Figure 38**). The results showed only a mild effect of aggregation on the overall measured signal integral and slight signal broadening. The signal broadening was more pronounced in the spectra of the more hydrophobic polymers such as polymer F1 with the lowest amount of hydrophilic HEAM monomer (**Figure 39**). Moreover, the presence of naturally occurring proteins in biological media (FBS and EMC gel) did not cause any additional signal broadening above the $T_{CP,}$ and the broadening was similar to that in buffer solutions.

Polymer	pH	$T_1 \pm SD$ (s)	$T_2 \pm SD$ (s)
F1	5.0	0.430 ± 0.008	0.331 ± 0.003
	7.4	0.494 ± 0.050	0.285 ± 0.013
F2	5.0	0.370 ± 0.012	0.405 ± 0.004
	7.4	0.453 ± 0.004	0.414 ± 0.007
F3	5.0	0.424 ± 0.003	0.401 ± 0.005
	7.4	0.440 ± 0.008	0.331 ± 0.004
F4	5.0	0.326 ± 0.003	0.426 ± 0.006
	7.4	0.426 ± 0.008	0.383 ± 0.007
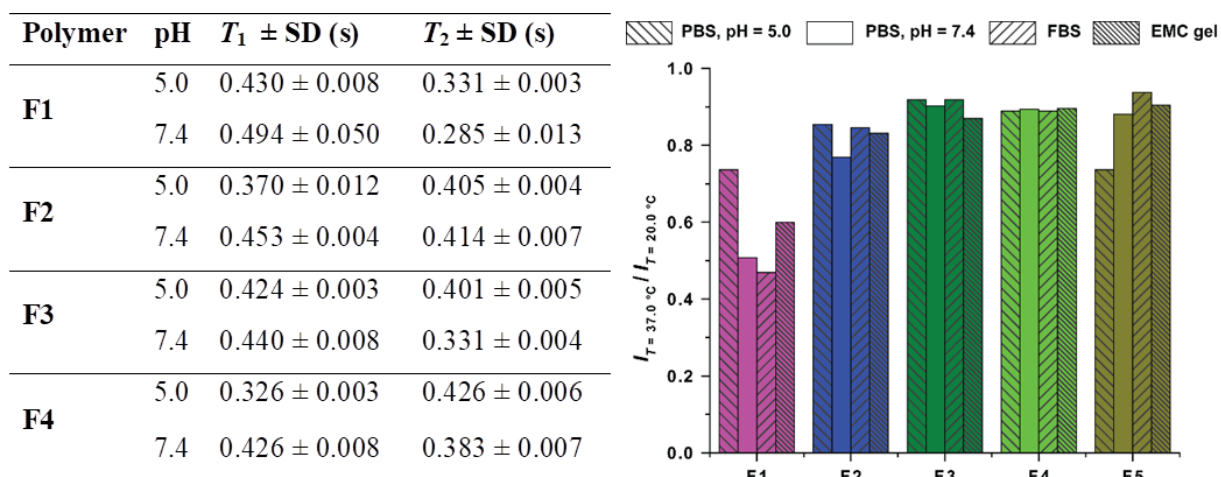
Figure 38. Left: Summary of the relaxation times of F1-F4 under a 4.7 T field at 37.0 °C (mean value ± SD based on the fitting residue). Right: Relative ^{19}F signal amplitude in buffer with pH 5.0 or 7.4 or in FBS or EMC gel after a change in temperature from 20.0 °C to 37.0 °C.
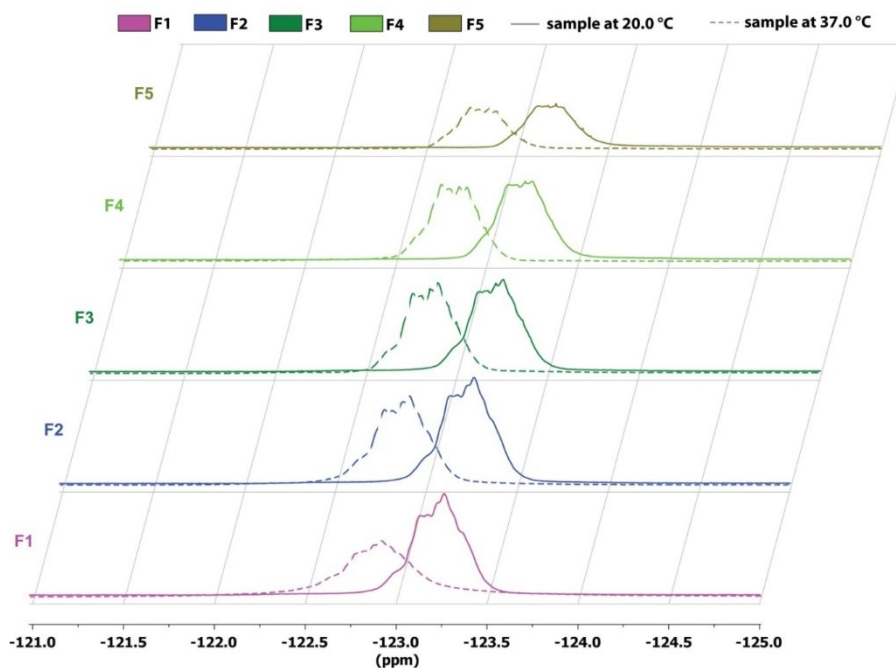
Figure 39. ^{19}F NMR scans of F1-F5 (c_{pol} = 15.0 mg·mL^{-1} in 40 mM phosphate-buffered saline, pH = 7.4), *D1* = 8.00 s, *NS* = 64, measured at 20.0 °C and 37.0 °C with a Bruker Avance III 400 MHz spectrometer (Bruker, Billerica, USA). The slight change in the chemical shifts observed at different temperatures is due to solvent (D$_2$O) locking.

3.4.4. In vivo ^{19}F MR imaging and implant dissolution

With the aim of injecting the prepared copolymers into the body to form implants or depots with the encapsulated drugs for slow drug release in mind, we investigated the fate of the implants *in vivo*. We could easily observe the dissolution *via* ^{19}F MRI, a precise and quantitative method for the investigation of the pharmacokinetics of the implant dissolution mechanism and rates. To obtain data for this kind of study, the polymers F1-F4 were injected subcutaneously (SC) and intramuscularly (IM) into healthy rats and monitored

69

by ^{19}F MRI (**Figure 40**, top). The obtained results were compared to those of polymer F0 from a previous study[66]; they were also compared with the concentration scale from a phantom measurement of polymer F3 in 150 mM PBS buffer, pH 7.4 (**Figure 35**, bottom).

	Hour 5	Day 1	Day 7	Day 30	Day 150	Day 275

^{1}H/ ^{19}F-RARE of phantoms

Polymer concetration (mg/mL)	100	50.0	25.0	12.5	6.25	3.13	1.56	0.00
Fluorine concentration (mg/mL)	21.4	10.7	5.35	2.68	1.34	0.67	0.33	0.00
Measured signal (relative)	1000	554	296	164	52.4	27.5	0.0	0.0
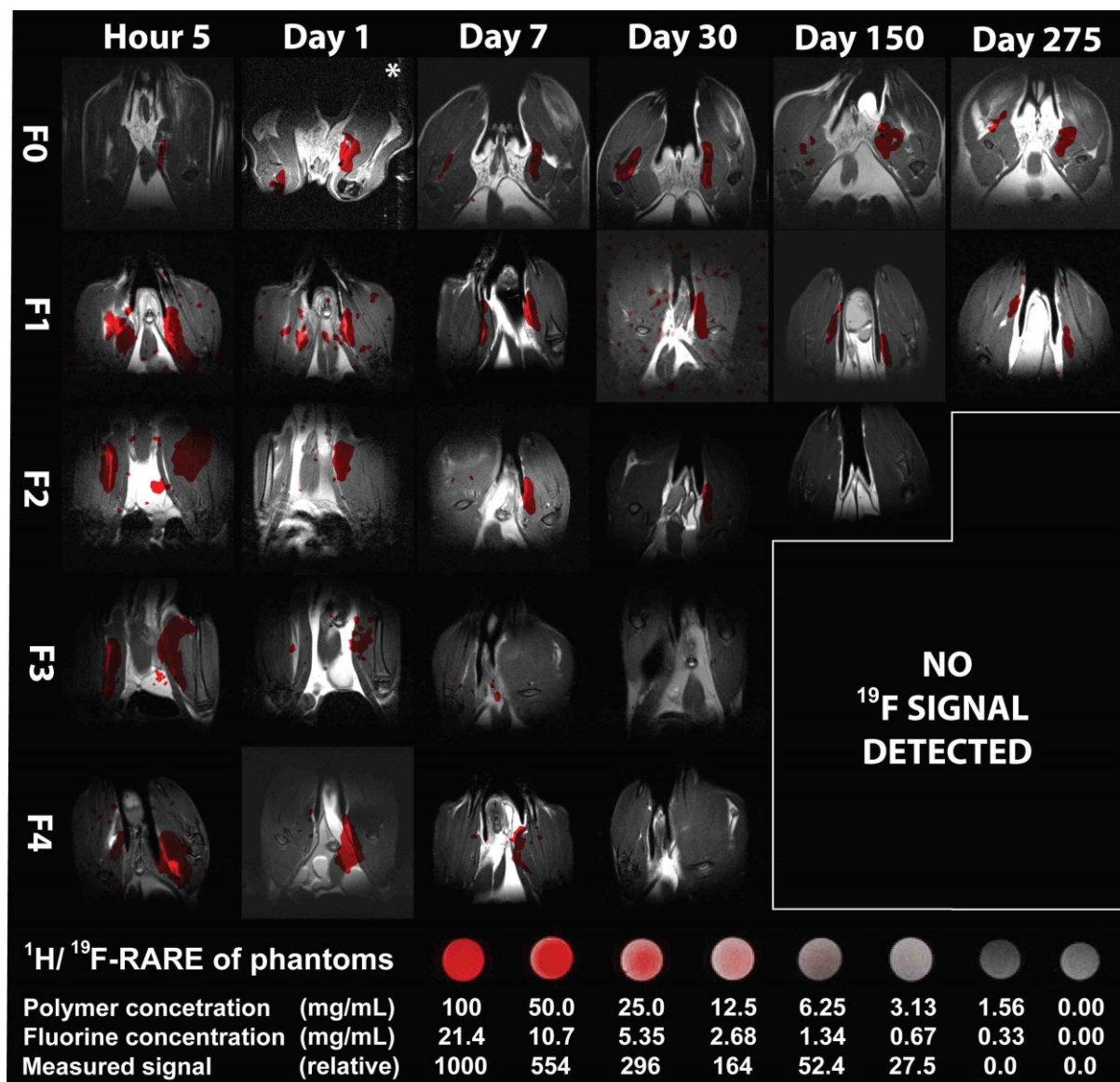
Figure 40. Top: Merged ^{1}H and ^{19}F MR images of rats injected with fluorinated polymers. Images were acquired at 5 h, 1 day, 7 days, 1 month and 9 months after administration. Since the image (*) from day 1 was not available, an image from day 4 was used instead. Bottom: Phantoms with a decreasing concentration of F3 polymer in 40 mM PBS (pH 7.4), merged ^{1}H/^{19}F-RARE images (17 min acquisition).

To quantify the ^{19}F signal, we collected the data from MR spectroscopy, MRI signal intensity (signal-to-noise ratio) and MRI-assessed implant volume and converted these data into specific pharmacokinetic data. However, as seen in **Figure 41**, the compared pharmacokinetics evaluation of the MRS data (top left) and the pharmacokinetics evaluation of MRI signal-to-noise data (bottom) showed that the most accurate way for quantification was

MR spectroscopy. The reason is that the MRS can evaluate the absolute integral of the ^{19}F signal of the measured implant, while the MRI signal and MRI-assessed implant volume are more prone to be influenced by the geometry of the implant and other factors. Therefore, to interpret the dissolution constants (**Figure 41**, top right), we used the MRS pharmacokinetic evaluation. As previously mentioned, the PDFEA-based polymers appear with a unique chemical shift in the MR spectrum, which does not interfere with the ^{19}F MR signal of isoflurane (a fluorinated inhalation anesthetic) used in this *in vivo* experiment (**Figure 42**).

Polymer	A_{MRS}	$t_{1/2} \pm SD$ (days)	R^2
F0	1.0	> 200	-
F1	0.6	86 ± 18	0.92
F2	0.2	48 ± 8	0.75
F3	0.1	36 ± 31	0.14
F4	0.2	31 ± 8	0.62
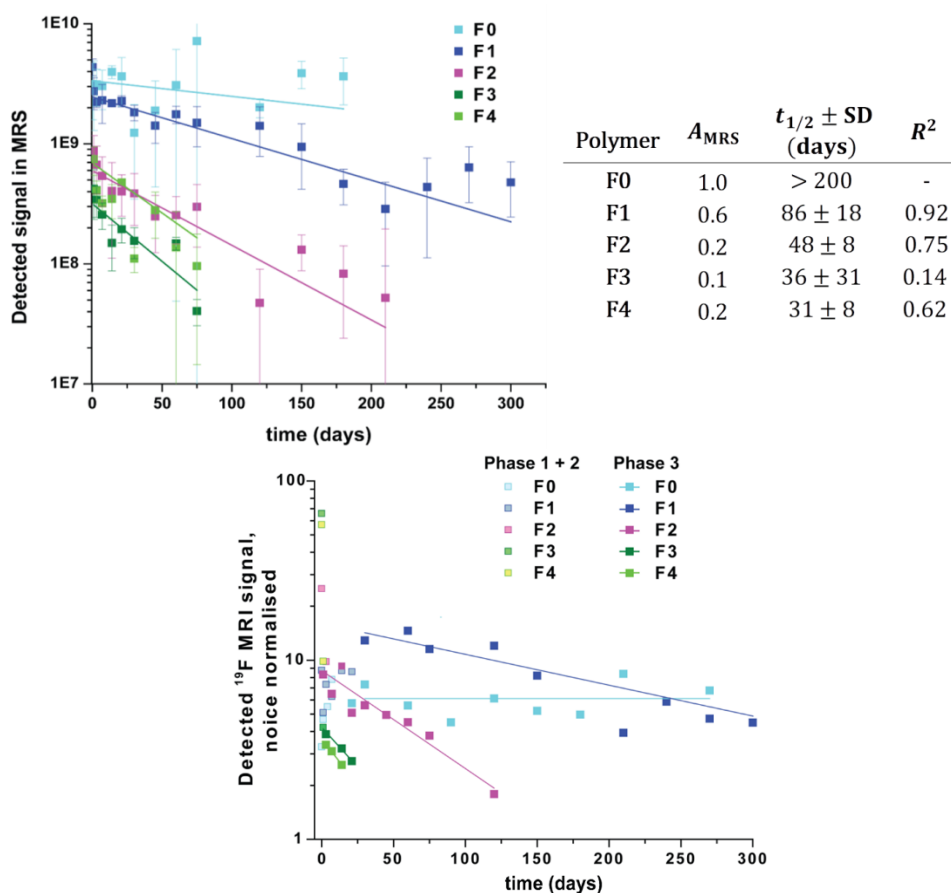
Figure 41. Top: ^{19}F MR spectroscopy performed on the thigh of a rat with a 4 cm circular ^{1}H/^{19}F RF surface coil, dissolution kinetics of polymers F0-F4 as a function of time. Parameters are the A_{MRS} and $t_{1/2}$ of the polymers, the fitting-based SD, and the fitting R^2. Bottom: ^{19}F MRI signal-to-noise dissolution kinetics of polymers F0-F4 after subcutaneous injection as a function of time. Demonstration of 1st-order kinetics during Phase 3 including data of more complex behavior in Phases 1 and 2. Standard deviations are not shown for clarity.
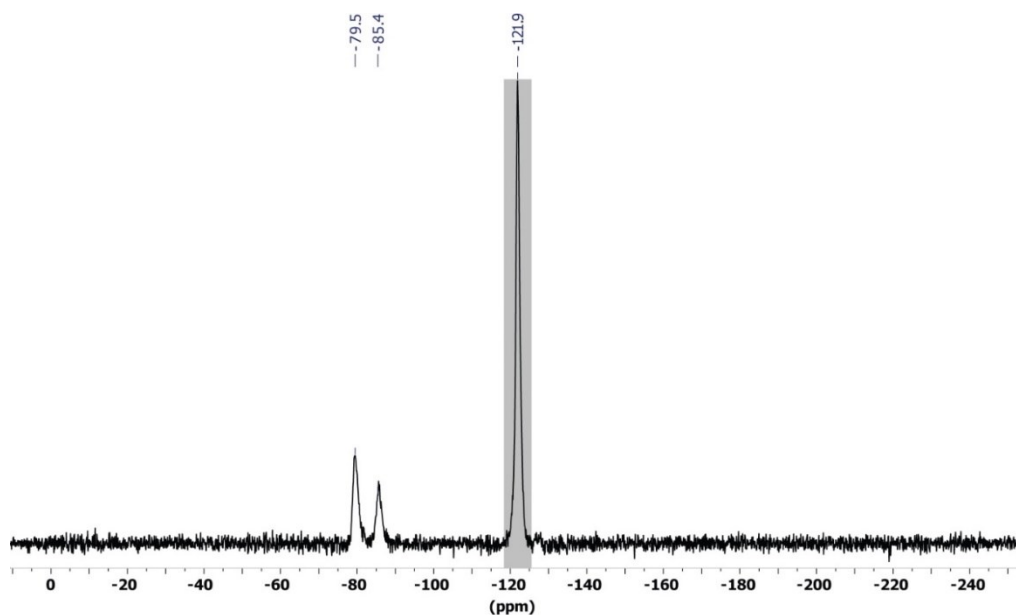
Figure 42. An *in vivo* ^{19}F spectrum at 4.7 T; the polymer signal and isoflurane signals can be observed. The gray rectangle shows the measured area during the MRI experiments (-125.4 to –118.4 ppm). No apodization was involved.

After the injection, the ^{19}F MR spectroscopic signal of the polymeric implant was detected. The administration was followed by a decrease in signal intensity over a short period (2 to 3 days), which was also observed in a similar study with radiolabeled poly(*N*-isopropylacrylamide (PNIPAM) injected as an implant.[159] We characterized this initial decrease in the signal by the parameter A_{MRS} (**Figure 41**, top right), which was more significant for the more hydrophilic polymers, indicating that dissolution into the blood and subsequent elimination occurred quickly during the first phase. After the first period, the polymer dissolution followed pseudo-1st-order kinetics (**Figure 41**).

We suggested a possible mechanism of implant dissolution based on the parameters from the kinetic study, as shown in **Figure 43**. As reported in several studies, during aggregation, thermoresponsive polymers tend to adhere to the cell membrane and bind to tissue.[160,161] It has also been shown that thermoresponsive polymers may be retained in organisms for a rather long time period; *e.g.*, poly(*N*-isopropylacrylamide with $M_W = 28$ kDa, $T_{LCST} = 32$ °C was retained after IM administration with a half-life of $t_{1/2} \geq 50$ days, which is in agreement with our findings.[159] The proposed mechanism showed that the cellular binding and dissolution into the blood were parallel processes; therefore, during the first period, when the polymer was not bound to the tissue, the signal decreased rapidly. The second phase consisted of a short and steady elimination of the tissue-bound polymer, which could be described with 1st-order kinetics.

72
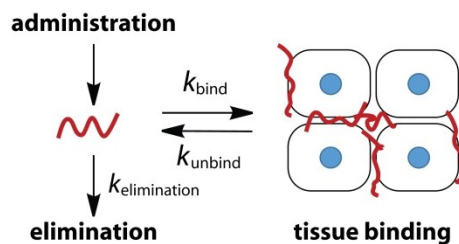
Figure 43. Proposed mechanism of polymer implant formation, interactions with tissues and their kinetics.

In conclusion, the kinetic parameters can be altered by changing the composition and by altering the LCST of the polymer. To demonstrate this effect, we plotted the parameter from the pharmacokinetics study and polymer T_{CP} as a function of the hydrophilic monomer concentration (**Figure 44**). With increasing hydrophilicity, the T_{CP} of the polymer at a given pH increased linearly, and the dissolution constant k_e increased (in other words, $t_{1/2}$ decreased). The parameter A_{MRS}, describing the portion of the tissue-bound polymer, decreased with the amount of hydrophilic monomer due to faster elimination of the polymer before binding to tissue.
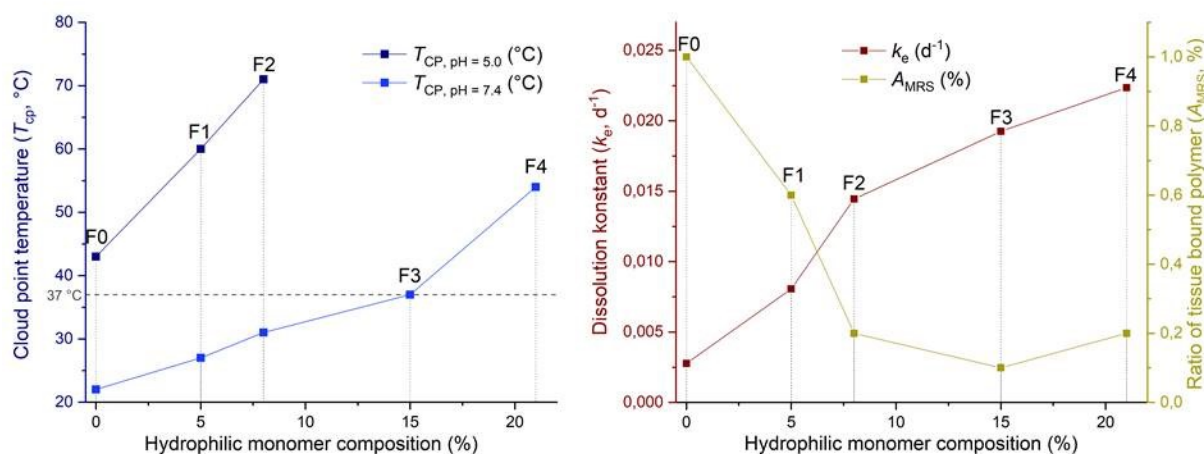
Figure 44. The resulting parameters of the synthetized copolymers as a function of the polymer composition. Parameters are evaluated from the MRS-assessed implant volumes after subcutaneous administration.

In general, the easiest way to quantify the dissolution rate of an implant is through its biological half-life, which for our polymer ranged from 30 days to more than 250 days. Interestingly, copolymers F3, with a T_{CP} close to body temperature, and F4, with a T_{CP} much higher than body temperature, showed very slow dissolution rates, as it would be in the case for diffusion-driven dissolution, suggesting that these polymers can partially bind to tissues as well. These findings open new possibilities for these polymers, such as tissue labeling for transplantations or tissue engineering. However, the mechanism of dissolution is only a proposition for further and more thorough study, and data from different thermoresponsive polymers are also required.

Finally, a rat with injected polymer F3 was subjected to a clinically used 3 T MRI scanner capable of measuring both ^{1}H MRI and ^{19}F MRI. The resulting image is shown in **Figure 45**, demonstrating the potential of our tracer to be used in clinical practice.
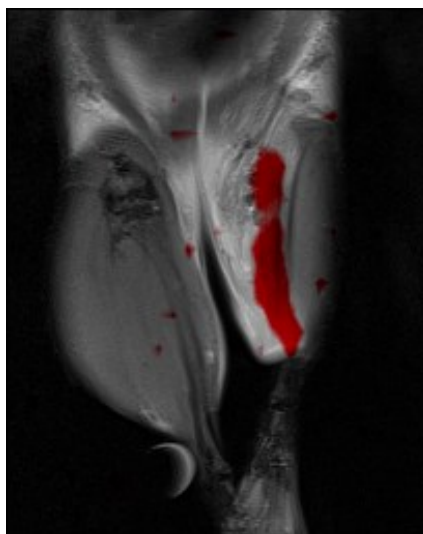
Figure 45. *In vivo* experiment with the clinically used 3 T MRI showing merged ^{19}F MRI (red) and ^{1}H MRI (grayscale).

3.4.5. Drug Release (DR)

To determine the ability of encapsulating and releasing a hydrophobic drug, we performed a simple DR experiment (**Figure 46**). For this experiment, we selected F1 as the experimental group and F4 as the control group since F4 did not form implants under physiological conditions. As a hydrophobic drug, dexamethasone (DXM) was used because it can be applied locally as an anti-inflammatory glucocorticoid; achieving its sustained release provides therapeutic value for a number of orthopedic applications. As a lipophilic drug, DXM can be encapsulated in the lipophilic aggregated state of the polymer, but its solubility (approx. 80 mg·L^{-1}) is still high enough for the compound to be detectable using HPLC with a UV-vis detector. In this experiment, the polymers were dissolved in a solution of DXM, transferred into a minidialysis kit and placed into a beaker with 25 mL of preheated (37 °C) PBS buffer. Small aliquots (20 µL) of the external liquid were taken, and the contents were analyzed using the previously mentioned HPLC device.

In both experiments, the DXM concentration in the external phase increased rather quickly during the initial phase (approx. 5 h), corresponding to the nonencapsulated polymer. After this first phase, significantly slower release was observed; less than 10% of the drug was released per day (with $t_{1/2} = 2.2$ d). Therefore, given the *in vitro* results, we can assume that our system can be used for the controlled release of hydrophobic drugs.
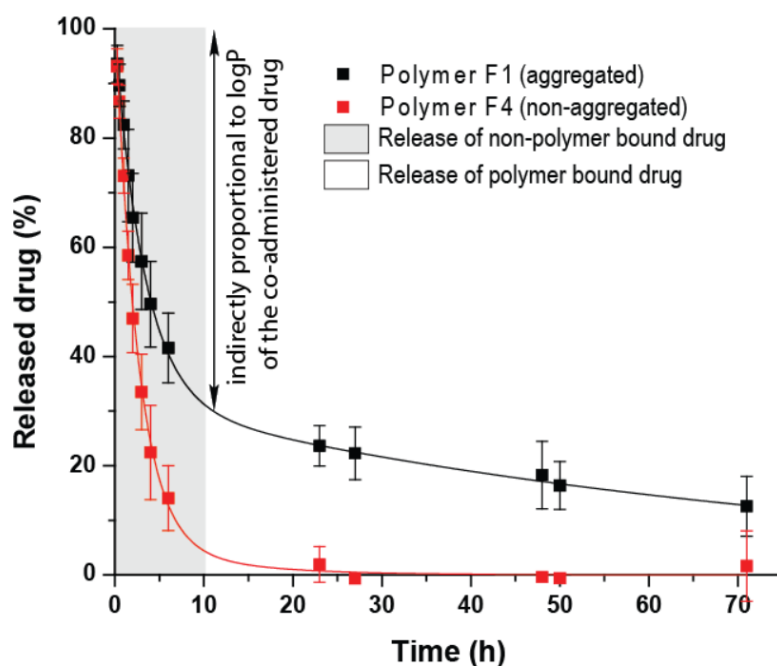
Figure 46. Drug release from the 50 mg depot *in vitro*; the plot shows the concentration of dexamethasone released from the depot as a function of time.

3.4.6. Biocompatibility study

To prevent undesirable reactions in the rats during the *in vivo* study with the prepared polymers, their cytotoxicity towards several cell lines was analyzed. None of the F1-F5 copolymers within the concentration range (8-1000 µg·mL^{-1}) decreased the cell viability of all tested cell lines below 70%, confirming the noncytotoxicity of the polymers (**Figure 47**).
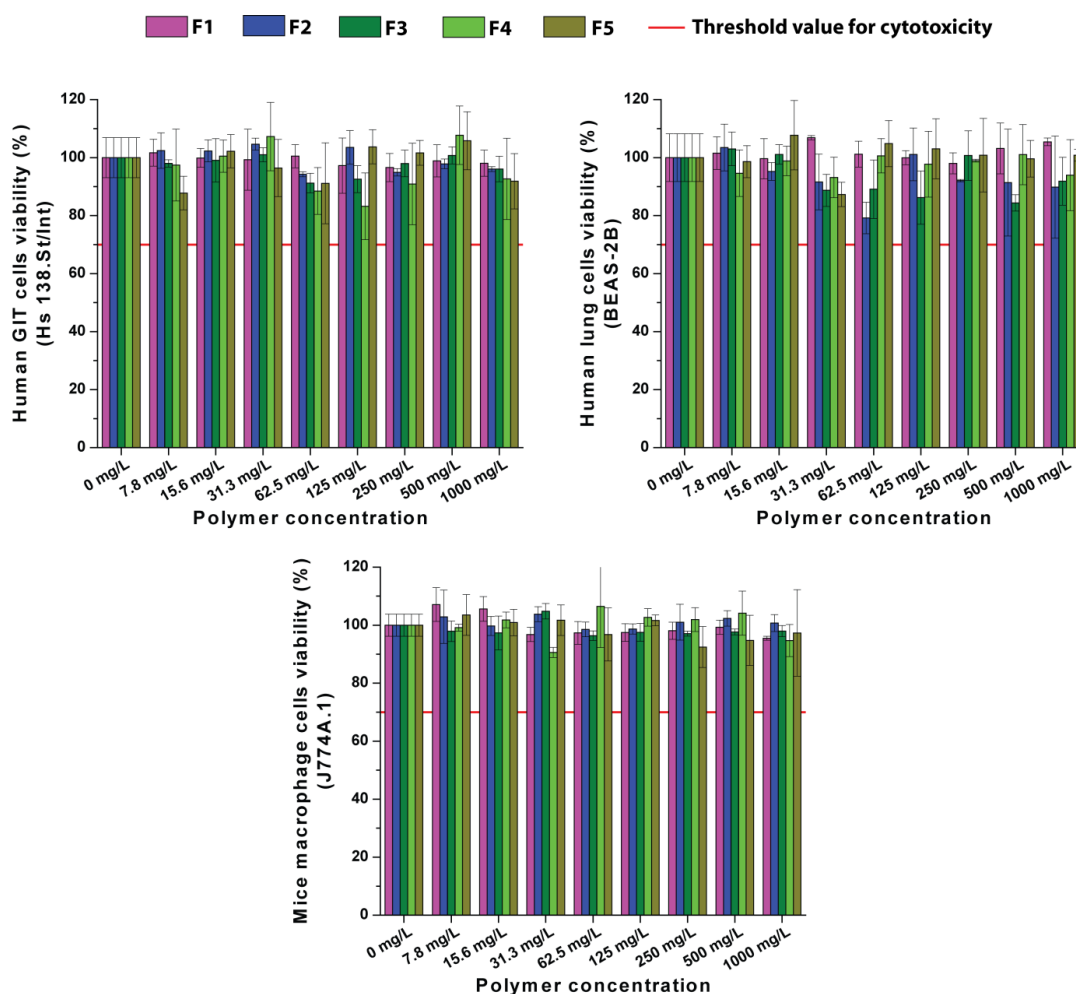
Figure 47. Viability of different cells (J774A.1, Hs 738. St/lnt and BEAS-2B) with increasing concentrations (0-1000 mg·L^{-1}) of polymer F1-F5.

The biocompatibility of the polymers was further studied during the *in vivo* ^{19}F MR imaging experiments in rats (**Figure 48**). Blood samples were taken and evaluated once a week at the beginning of the experiment and then once a month for the polymers with the longest dissolution times. A standard blood test was performed to assess the activities of aspartate aminotransferase (AST, EC 2.6.1.1) and alanine aminotransferase (ALT, EC 2.6.1.2) and the concentrations of bilirubin, creatinine, and albumin to ensure that there was no pathology or organ damage. Another indicator of pathology or discomfort is steady or decreasing weight; therefore, the weights of the rats were monitored during the experiment. All mentioned biomarker values were consistent throughout the experiment and within the range of the control group, indicating that the polymers had a minor to negligible influence on the rat health.
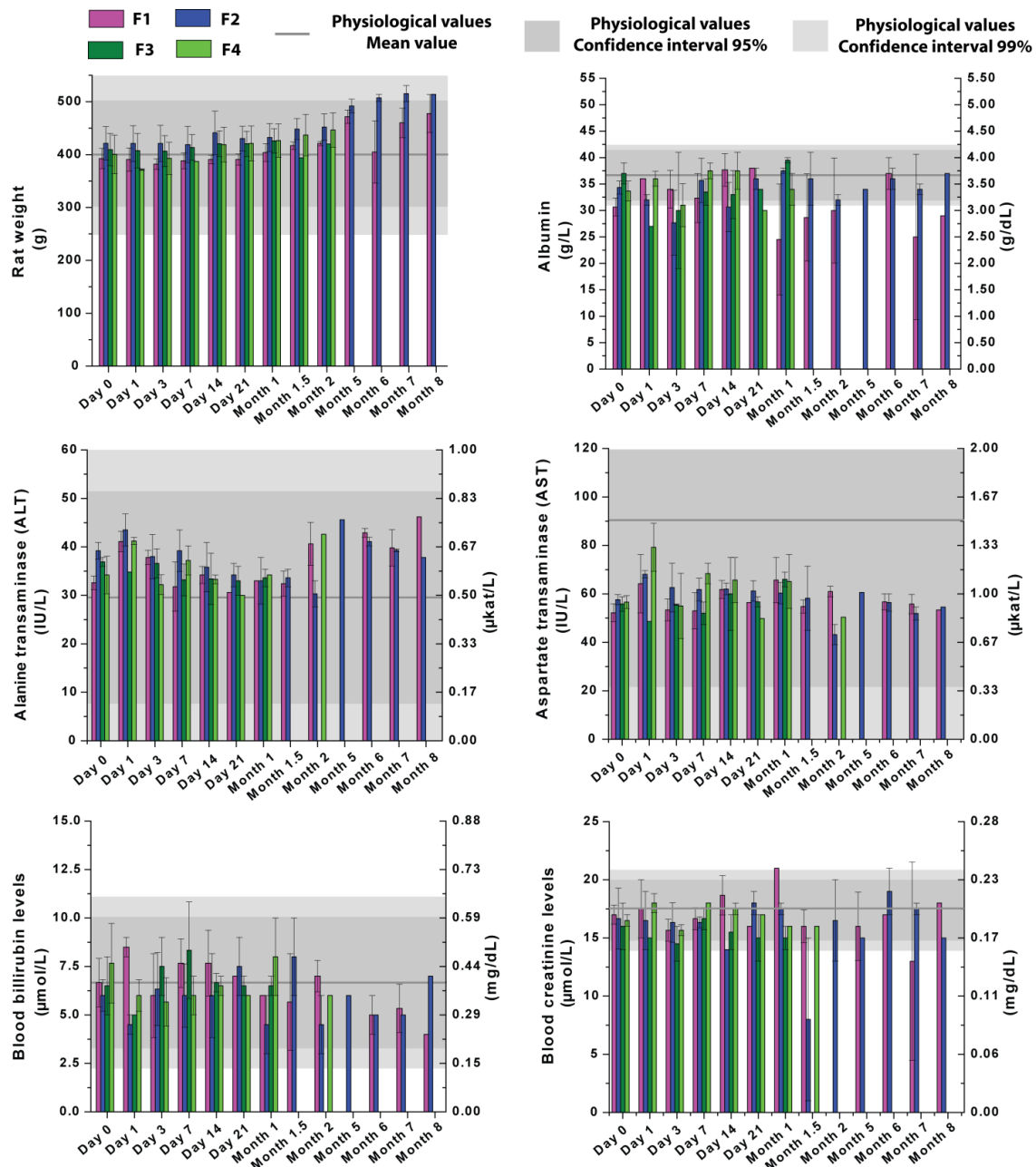
Figure 48. Tested biomarkers of systemic toxicity: body weight, albumin, ALT, AST, blood bilirubin and creatinine.

At the end of the experiment, the rats were sacrificed, and the sites of the implant formation were assessed to determine if there was any pathology. A histological examination was performed (**Figure 49**). Both investigations showed no pathology, implying that the polymers should be biocompatible in all aspects.
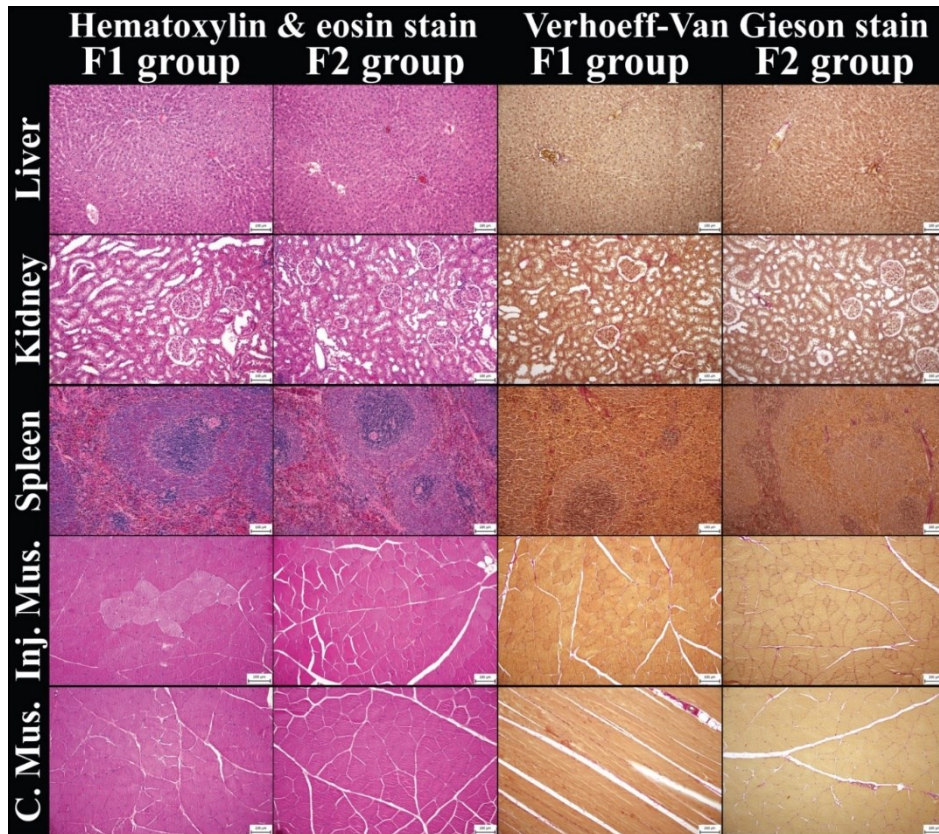
Figure 49. Histological examination of the tested animals: liver, kidney, spleen, muscle after administration and contralateral muscle of the groups F1 and F2 1 year after administration. Stained with hematoxylin and eosin and Verhoeff-Van Gieson stain; all images are magnified 200 times.

3.5. Summary of the developed ^{19}F MRI tracers and their applications

In this section, we review the main advantages and the importance of ^{19}F MRI as a highly promising method, which has emerged in clinical practice over the last few decades. On the other hand, this section also summarizes the main drawbacks and obstacles such as the low sensitivity and lipophilicity of ^{19}F MRI tracers as well as the possible way to overcome these problems. The main idea is to summarize the commonly used perfluorocarbons (PFCs) developed for medical purposes and their ^{19}F MRI properties and compare them to macromolecular fluorinated structures. Macromolecular ^{19}F MRI tracers are more advanced and can be tailored to meet the demands of the desired clinical application, which is highly advantageous for use in ^{19}F MRI. A detailed description of the MRI method, parameters of contrast agents and tracers, summary of the commonly used PFCs, macromolecular tracers and their synthesis as well as a smart theranostic systems with ^{19}F MRI modality are summarized in the Introduction, **Chapter 1.** The future perspectives of ^{19}F MRI and developing tracers are summarized in the Conclusion, **Chapter 4.**[29]

4. Conclusion

We described and thoroughly investigated following poly[(*N*- 2,2-difluoroethyl) acrylamide] (PDFEA) based systems:

1. The self-assembled thermoresponsive polymeric physically crosslinked nanogels suitable as a tracer for ^{19}F MRI with high loading of magnetically equivalent fluorine atoms (18.7 – 20.7 wt. %). The system was based on amphiphilic diblock copolymers with two different hydrophilic blocks – PHPMA or PMeOx, respectively. The structure of the particles was highly dependent on the block ratio, the size of the nanogels formed after heating from room to body temperature may be fine-tuned in a wide range. The *in vitro* ^{19}F MRI experiments reveal the excellent sensitivity of the copolymer contrast agents, while the nanogels were shown to be noncytotoxic for several cell lines. Polymer (PMeOx-*block*-PDFEA 1:2, MF), with the size ideal for medical applications (tens of nanometers) was selected for further study. The architecture and internal structure of assemblies prepared by heating up the aqueous solution of selected polymer was determined by various physicochemical methods (DLS, SLS, SANS, SAXS, ^{1}H and ^{19}F NMR, NOESY, DOSY). The polymer was shown to form complex nanoparticular structures both above and the cloud point temperature. We found out that there exists equilibrium between molecularly dissolved polymer chains, micelle-like structures, and larger aggregates. The formation of larger aggregates is then strongly dictated by the solvent properties as evidenced by varying behavior in different solvents. Furthermore, the larger aggregates were determined as physically crosslinked nanogels with the loosely formed network of hydrophobic blocks interconnected by hydrogen bonds whose hydrophobicity forces them out of the aqueous environment as demonstrated by the calculated Flory exponents. This network is then probably shielded by swollen hydrophilic PMeOx, binding high amounts of water, behaving as coils in a good solvent. Finally, our measurements of ^{19}F NMR showed that polymer provides measurable fluorine signal even in the aggregated state. In conclusion, the measured parameters are in an agreement with those for a suitable ^{19}F MRI tracer.

2. We modified the previously described system based on PHPMA-*block*-PDFEA 1:2, HF polymer with a few molar percent of ferrocene moieties in order to prepare a thermoresponsive system capable of controlled disassociation (and subsequent drug release) upon oxidation under certain conditions to obtain a theranostic system. Ferrocene was selected due to its well known sensitivity to oxidative environment. After oxidation to ferrocenium cation, it affects the amphiphilic character of the polymer and the particles are dissembled. We observed the self-assembly and disassembly with the change of temperature and after oxidation of ferrocene by DLS. The suitability for ^{19}F MRI was determined by collection of relaxation times, MRS and phantom measurement, which shows good sensitivity. The drug release of the hydrophobic drug was tested *in vitro* in the presence of tumor cells, naturally forming the oxidative environment. Results showed that the polymer is capable of effective drug release under these conditions.

3. We prepared a wide range of injectable PDFEA-based implants that can be easily visualized *via* ^{19}F MRI with equipment that is used in clinical practice, containing imidazole moieties as a pH-responsive monomer and hydrophilic monomers to tailor the polymer dissolution times. The suitability for ^{19}F MRI was determined by collection

of relaxation times, MRS and phantom measurement, which shows a good sensitivity. Finally, we performed *in vivo* experiments confirmed that the addition of a hydrophilic monomer to the polymer results in these multiresponsive polymers having a tunable dissolution rate and we used the data to propose the mechanism of aggregated implant dissolution in a biological system.

In summary, our polymer tracers contain a high content of equivalent fluorine atoms (all of them fit into the chemical shift window of interest, -124 nm), efficient mobility in aggregated state resulting in suitable relaxation times (varied according to certain modification, *e.g.* ferrocene significantly lowered the T_2 relaxation times), adequate solubility in water, modifiable structure for targeting and controlled release and reliable pharmacokinetic and pharmacodynamic properties, including biodegradability and elimination after the probe fulfills its task.

5. References

(1)   Lauterbur, P. C. Image Formation by Induced Local Interactions: Examples Employing Nuclear Magnetic Resonance. *Nature* **1973**, *242*, 190–191.

(2)   Rinck, P. A. A Short History of Magnetic Resonance Imaging. *Spectrosc. Eur.* **2008**, *20*, 7-9.

(3)   Mansfield, P.; Grannell, P. K. "Diffraction" and Microscopy in Solids and Liquids by NMR. *Phys. Rev. B* **1975**, *12*, 3618–3634.

(4)   Getting in Tune: Resonance and Relaxation. *MRI from Picture to Proton*; McRobbie, D. W., Moore, E. A., Graves, M. J., Prince, M. R., Eds.; *Cambridge University Press: Cambridge*, **2017**, 124–143.

(5)   Allisy-Roberts, P.; Williams, J. *Chapter 10 - Magnetic Resonance Imaging*; Allisy-Roberts, P., Williams, J. B., **2008**, 169–195.

(6)   Huettel, S. A.; Song, A. W.; McCarthy, G. *FUNCTIONAL Magnetic Resonance Imaging*, First.; Sinauer Associates: Sunderland, **2004**.

(7)   Kini, L.; Gee, J.; Litt, B. Computational Analysis in Epilepsy Neuroimaging: A Survey of Features and Methods. *NeuroImage Clin.* **2016**, *11*, 519-529.

(8)   Nelson, T. R.; Newman, F. D.; Schiffer, L. M.; Reith, J. D.; Cameron, S. L. Fluorine Nuclear Magnetic Resonance: Calibration and System Optimization. *Magn. Reson. Imaging* **1985**, *3*, 267–273.

(9)   Tooyama, I.; Yanagisawa, D.; Taguchi, H.; Kato, T.; Hirao, K.; Shirai, N.; Sogabe, T.; Ibrahim, N. F.; Inubushi, T.; Morikawa, S. Amyloid Imaging Using Fluorine-19 Magnetic Resonance Imaging (^{19}F-MRI). *Ageing Res. Rev.* **2016**, *30*, 85–94.

(10)   Friebe, M. Computed Tomography and Magnetic Resonance Imaging Contrast Media Injectors: Technical Feature Review - What Is Really Needed? *Med. Devices Evid. Res.* **2016**, *2016*, 231–239.

(11)   Ahrens, E. T.; Rothbächer, U.; Jacobs, R. E.; Fraser, S. E. A Model for MRI Contrast Enhancement Using T_1 Agents. *Proc. Natl. Acad. Sci.* **1998**, *95*, 8443–8448.

(12)   Na, H. Bin; Hyeon, T. Nanostructured T_1 MRI Contrast Agents. *J. Mater. Chem.* **2009**, *19*, 6267–6273.

(13)   Servant, A.; Jacobs, I.; Bussy, C.; Fabbro, C.; da Ros, T.; Pach, E.; Ballesteros, B.; Prato, M.; Nicolay, K.; Kostarelos, K. Gadolinium-Functionalised Multi-Walled Carbon Nanotubes as a T_1 Contrast Agent for MRI Cell Labelling and Tracking. *Carbon N. Y.* **2016**, *97*, 126–133.

(14)   Qin, J.; Laurent, S.; Jo, Y. S.; Roch, A.; Mikhaylova, M.; Bhujwalla, Z. M.; Muller, R. N.; Muhammed, M. A High-Performance Magnetic Resonance Imaging T_2 Contrast Agent. *Adv. Mater.* **2007**, *19*, 1874–1878.

(15)   Ye, F.; Laurent, S.; Fornara, A.; Astolfi, L.; Qin, J.; Roch, A.; Martini, A.; Toprak, M. S.; Muller, R. N.; Muhammed, M. Uniform Mesoporous Silica Coated Iron Oxide Nanoparticles as a Highly Efficient, Nontoxic MRI T_2 Contrast Agent with Tunable Proton Relaxivities. *Contrast Media Mol. Imaging* **2012**, *7*, 460–468.

(16) Im, G. H.; Kim, S. M.; Lee, D.-G.; Lee, W. J.; Lee, J. H.; Lee, I. S. Fe3O4/MnO Hybrid Nanocrystals as a Dual Contrast Agent for Both T_1- and T_2-Weighted Liver MRI. *Biomaterials* **2013**, *34*, 2069–2076.

(17) www.wikipedia.org https://en.wikipedia.org/wiki/MRI_contrast_agent.

(18) Geraldes, C. F. G. C.; Laurent, S. Classification and Basic Properties of Contrast Agents for Magnetic Resonance Imaging. *Contrast Media Mol. Imaging* **2009**, *4*, 1–23.

(19) Chen, Y.; Chen, H.; Zhang, S.; Chen, F.; Sun, S.; He, Q.; Ma, M.; Wang, X.; Wu, H.; Zhang, L.; Zhang, L.; Shi, J. Structure-Property Relationships in Manganese Oxide - Mesoporous Silica Nanoparticles Used for T_1-Weighted MRI and Simultaneous Anti-Cancer Drug Delivery. *Biomaterials* **2012**, *33*, 2388–2398.

(20) Na, H. B.; Lee, J. H.; An, K.; Park, Y. I.; Park, M.; Lee, I. S.; Nam, D.-H.; Kim, S. T.; Kim, S.-H.; Kim, S.-W.; Lim, K.-H.; Kim, K.-S.; Kim, S.-O.; Hyeon, T. Development of a T_1 Contrast Agent for Magnetic Resonance Imaging Using MnO Nanoparticles. *Angew. Chemie Int. Ed.* **2007**, *46*, 5397–5401.

(21) Li, X.; Zhao, W.; Liu, X.; Chen, K.; Zhu, S.; Shi, P.; Chen, Y.; Shi, J. Mesoporous Manganese Silicate Coated Silica Nanoparticles as Multi-Stimuli-Responsive T_1-MRI Contrast Agents and Drug Delivery Carriers. *Acta Biomater.* **2016**, *30*, 378–387.

(22) Bulte, J. W. M.; Cuyper, M. de; Despres, D.; Frank, J. A. Preparation, Relaxometry, and Biokinetics of PEGylated Magnetoliposomes as MR Contrast Agent. *J. Magn. Magn. Mater.* **1999**, *194*, 204–209.

(23) Cheng, Z.; Thorek, D. L. J.; Tsourkas, A. Gadolinium-Conjugated Dendrimer Nanoclusters as a Tumor-Targeted T_1 Magnetic Resonance Imaging Contrast Agent. *Angew. Chemie Int. Ed.* **2010**, *49*, 346–350.

(24) Staal, X.; Koshkina, O.; Srinivas, M., *Chapter 11 - In Vivo 19-Fluorine Magnetic Resonance Imaging,* Progress in Fluorine Science; Haufe, G., Leroux Medicinal Diagnostics, and Agrochemicals, *Academic Press*, **2019**, 397–424.

(25) Ruiz-Cabello, J.; Barnett, B. P.; Bottomley, P. A.; Bulte, J. W. M. Fluorine (19F) MRS and MRI in Biomedicine. *NMR Biomed.* **2011**, *24*, 114–129.

(26) Floger, U.; Ahrens, E. *Fluorine Magnetic Resonance Imaging*, 1st ed.; Jenny Stanford Publishing, **2016**.

(27) Srinivas, M.; Heerschap, A.; Ahrens, E. T.; Figdor, C. G.; Vries, I. J. M. de. [19]F MRI for Quantitative *in Vivo* Cell Tracking. *Trends Biotechnol.* **2010**, *28*, 363–370.

(28) Gillis, E. P.; Eastman, K. J.; Hill, M. D.; Donnelly, D. J.; Meanwell, N. A. Applications of Fluorine in Medicinal Chemistry. *J. Med. Chem.* **2015**, *58*, 8315–8359.

(29) Jirak, D.; Galisova, A.; Kolouchova, K.; Babuka, D.; Hruby, M. Fluorine Polymer Probes for Magnetic Resonance Imaging: Quo Vadis? *Magn. Reson. Mater. Physics, Biol. Med.* **2019**, *32*, 173–185.

(30) Mattrey, R. F. Perfluorooctylbromide: A New Contrast Agent for CT, Sonography, and MR Imaging. *Am. J. Roentgenol.* **1989**, *152*, 247–252.

(31) Cho, M. H.; Shin, S. H.; Park, S. H.; Kadayakkara, D. K.; Kim, D.; Choi, Y. Targeted, Stimuli-Responsive, and Theranostic [19]F Magnetic Resonance Imaging Probes. *Bioconjug. Chem.* **2019**, *30*, 2502–2518.

(32) Jacoby, C.; Temme, S.; Mayenfels, F.; Benoit, N.; Krafft, M. P.; Schubert, R.; Schrader, J.; Flögel, U. Probing Different Perfluorocarbons for *in Vivo* Inflammation Imaging by ^{19}F MRI: Image Reconstruction, Biological Half-Lives and Sensitivity. *NMR Biomed.* **2014**, *27*, 261–271.

(33) Srinivas, M.; Boehm-Sturm, P.; Figdor, C. G.; de Vries, I. J.; Hoehn, M. Labeling Cells for *in Vivo* Tracking Using ^{19}F MRI. *Biomaterials* **2012**, *33*, 8830–8840.

(34) Srinivas, M.; Cruz, L. J.; Bonetto, F.; Heerschap, A.; Figdor, C. G.; de Vries, I. J. M. Customizable, Multi-Functional Fluorocarbon Nanoparticles for Quantitative *in Vivo* Imaging Using ^{19}F MRI and Optical Imaging. *Biomaterials* **2010**, *31*, 7070–7077.

(35) Constantinides, C.; Maguire, M.; McNeill, E.; Carnicer, R.; Swider, E.; Srinivas, M.; Carr, C. A.; Schneider, J. E. Fast, Quantitative, Murine Cardiac ^{19}F MRI/MRS of PFCE-Labeled Progenitor Stem Cells and Macrophages at 9.4T. *PLoS One* **2018**, *13*, e0190558.

(36) Barnett, B. P.; Ruiz-Cabello, J.; Hota, P.; Ouwerkerk, R.; Shamblott, M. J.; Lauzon, C.; Walczak, P.; Gilson, W. D.; Chacko, V. P.; Kraitchman, D. L.; Arepally, A.; Bulte, J. W. M. Use of Perfluorocarbon Nanoparticles for Non-Invasive Multimodal Cell Tracking of Human Pancreatic Islets. *Contrast Media Mol. Imaging* **2011**, *6*, 251–259.

(37) Tirotta, I.; Mastropietro, A.; Cordiglieri, C.; Gazzera, L.; Baggi, F.; Baselli, G.; Bruzzone, M. G.; Zucca, I.; Cavallo, G.; Terraneo, G.; Baldelli Bombelli, F.; Metrangolo, P.; Resnati, G. A Superfluorinated Molecular Probe for Highly Sensitive *in Vivo* ^{19}F-MRI. *J. Am. Chem. Soc.* **2014**, *136*, 8524–8527.

(38) Larson, P. E. Z.; Han, M.; Krug, R.; Jakary, A.; Nelson, S. J.; Vigneron, D. B.; Henry, R. G.; McKinnon, G.; Kelley, D. A. C. Ultrashort Echo Time and Zero Echo Time MRI at 7T. *Magn. Reson. Mater. Physics, Biol. Med.* **2016**, *29*, 359–370.

(39) Bloembergen, N.; Purcell, E. M.; Pound, R. V. Relaxation Effects in Nuclear Magnetic Resonance Absorption. *Phys. Rev.* **1948**, *73*, 679–712.

(40) Amatsubo, T.; Morikawa, S.; Inubushi, T.; Urushitani, M.; Taguchi, H.; Shirai, N.; Hirao, K.; Kato, M.; Morino, K.; Kimura, H.; Nakano, I.; Yoshida, Ch.; Okada, T.; Sano, M.; Tooyama, I. Trifluoromethoxy-benzylated ligands improve amyloid detection in the brain using ^{19}F magnetic resonance imaging. *J. Neurosci. Res.* **2009**, *63*, 76–81.

(41) Bennett, K. M.; Jo, J.; Cabral, H.; Bakalova, R.; Aoki, I. MR Imaging Techniques for Nano-Pathophysiology and Theranostics. *Adv. Drug Deliv. Rev.* **2014**, *74*, 75–94.

(42) Alexis, F.; Anker, J. N. Theranostic Nanotechnologies: Moving beyond Imaging Drug Localization? *Ther. Deliv.* **2014**, *5*, 97–100.

(43) Vu-Quang, H.; Vinding, M. S.; Nielsen, T.; Ullisch, M. G.; Nielsen, N. C.; Kjems, J. Theranostic Tumor Targeted Nanoparticles Combining Drug Delivery with Dual near Infrared and [19]F Magnetic Resonance Imaging Modalities. *Nanomedicine Nanotechnology, Biol. Med.* **2016**, *12*, 1873–1884.

(44) Fuchs, A. V; Bapat, A. P.; Cowin, G. J.; Thurecht, K. J. Switchable ^{19}F MRI Polymer Theranostics: Towards in Situ Quantifiable Drug Release. *Polym. Chem.* **2017**, *8*, 5157–5166.

(45) Porsch, C.; Zhang, Y.; Östlund, Å.; Damberg, P.; Ducani, C.; Malmström, E.; Nyström, A. M. *In Vitro* Evaluation of Non-Protein Adsorbing Breast Cancer Theranostics Based on ^{19}F-Polymer Containing Nanoparticles. *Part. Part. Syst. Charact.* **2013**, *30*, 381–390.

(46) Sumer, B.; Gao, J. Theranostic Nanomedicine for Cancer. *Nanomedicine* **2008**, *3*, 137–140.

(47) Dewitte, H.; Geers, B.; Liang, S.; Himmelreich, U.; Demeester, J.; De Smedt, S. C.; Lentacker, I. Design and Evaluation of Theranostic Perfluorocarbon Particles for Simultaneous Antigen-Loading and ^{19}F-MRI Tracking of Dendritic Cells. *J. Control. Release* **2013**, *169*, 141–149.

(48) Shin, S. H.; Park, E.-J.; Min, C.; Choi, S. Il; Jeon, S.; Kim, Y.-H.; Kim, D. Tracking Perfluorocarbon Nanoemulsion Delivery by ^{19}F MRI for Precise High Intensity Focused Ultrasound Tumor Ablation. *Theranostics* **2017**, *7*, 562–572.

(49) Ganta, S.; Devalapally, H.; Shahiwala, A.; Amiji, M. A Review of Stimuli-Responsive Nanocarriers for Drug and Gene Delivery. *J. Control. Release* **2008**, *126*, 187–204.

(50) Giraudeau, C.; Geffroy, F.; Mériaux, S.; Boumezbeur, F.; Robert, P.; Port, M.; Robic, C.; Le Bihan, D.; Lethimonnier, F.; Valette, J. [19]F Molecular MR Imaging for Detection of Brain Tumor Angiogenesis: *In Vivo* Validation Using Targeted PFOB Nanoparticles. *Angiogenesis* **2013**, *16*, 171–179.

(51) Southworth, R.; Kaneda, M.; Chen, J.; Zhang, L.; Zhang, H.; Yang, X.; Razavi, R.; Lanza, G.; Wickline, S. A. Renal Vascular Inflammation Induced by Western Diet in ApoE-Null Mice Quantified by ^{19}F NMR of VCAM-1 Targeted Nanobeacons. *Nanomedicine Nanotechnology, Biol. Med.* **2009**, *5*, 359–367.

(52) Bae, P. K.; Jung, J.; Lim, S. J.; Kim, D.; Kim, S.-K.; Chung, B. H. Bimodal Perfluorocarbon Nanoemulsions for Nasopharyngeal Carcinoma Targeting. *Mol. Imaging Biol.* **2013**, *15*, 401–410.

(53) Sebastian, T.; Christoph, G.; Christine, Q.; Christoph, J.; Maria, G.; Zhaoping, D.; Christoph, O.; Friederike, M.; W., F. J.; Rolf, S.; Jürgen, S.; Ulrich, F. Noninvasive Imaging of Early Venous Thrombosis by [19]F Magnetic Resonance Imaging With Targeted Perfluorocarbon Nanoemulsions. *Circulation* **2015**, *131*, 1405–1414.

(54) Waters, E. A.; Chen, J.; Allen, J. S.; Zhang, H.; Lanza, G. M.; Wickline, S. A. Detection and Quantification of Angiogenesis in Experimental Valve Disease with Integrin-Targeted Nanoparticles and 19-Fluorine MRI/MRS. *J. Cardiovasc. Magn. Reson.* **2008**, *10*, 43.

(55) Weibel, S.; Basse-Luesebrink, T. C.; Hess, M.; Hofmann, E.; Seubert, C.; Langbein-Laugwitz, J.; Gentschev, I.; Sturm, V. J. F.; Ye, Y.; Kampf, T.; Jakob, P. M.; Szalay, A. A. Imaging of Intratumoral Inflammation during Oncolytic Virotherapy of Tumors by ^{19}F-Magnetic Resonance Imaging (MRI). *PLoS One* **2013**, *8*, e56317.

(56) Waiczies, H.; Guenther, M.; Skodowski, J.; Lepore, S.; Pohlmann, A.; Niendorf, T.; Waiczies, S. Monitoring Dendritic Cell Migration Using ^{19}F/[1]H Magnetic Resonance Imaging. *JoVE* **2013**, *73*, e50251.

(57) Ahrens, E. T.; Helfer, B. M.; O'Hanlon, C. F.; Schirda, C. Clinical Cell Therapy Imaging Using a Perfluorocarbon Tracer and Fluorine-19 MRI. *Magn. Reson. Med.* **2014**, *72*, 1696–1701.

(58) Ahrens, E. T.; Bulte, J. W. M. Tracking Immune Cells *in Vivo* Using Magnetic Resonance Imaging. *Nat. Rev. Immunol.* **2013**, *13*, 755–763.

(59) Ahrens, E. T.; Flores, R.; Xu, H.; Morel, P. A. *In Vivo* Imaging Platform for Tracking

Immunotherapeutic Cells. *Nat. Biotechnol.* **2005**, *23*, 983–987.

(60)   Peng, H.; Blakey, I.; Dargaville, B.; Rasoul, F.; Rose, S.; Whittaker, A. K. Synthesis and Evaluation of Partly Fluorinated Block Copolymers as MRI Imaging Agents. *Biomacromolecules* **2009**, *10*, 374–381.

(61)   Peng, H.; KJ, T.; Blakey, I.; Taran, E.; AK, W. Effect of Solvent Quality on the Solution Properties of Assemblies of Partially Fluorinated Amphiphilic Diblock Copolymers. *Macromolecules* **2012**, *45*, 8681–8690.

(62)   Cheng, C.; Powell, K. T.; Khoshdel, E.; Wooley, K. L. Polydimethylsiloxane- (PDMS-) Grafted Fluorocopolymers by a "Grafting through" Strategy Based on Atom Transfer Radical (Co)Polymerization. *Macromolecules* **2007**, *40*, 7195–7207.

(63)   Nyström, A. M.; Bartels, J. W.; Du, W.; Wooley, K. L. Perfluorocarbon-Loaded Shell Crosslinked Knedel-like Nanoparticles: Lessons Regarding Polymer Mobility and Self-Assembly. *J. Polym. Sci. Part A Polym. Chem.* **2009**, *47*, 1023–1037.

(64)   Babuka, D.; Kolouchova, K.; Hruby, M.; Groborz, O.; Tosner, Z.; Zhigunov, A.; Stepanek, P. Investigation of the Internal Structure of Thermoresponsive Diblock Poly(2-Methyl-2-Oxazoline)-b-Poly[N-(2,2-Difluoroethyl)Acrylamide] Copolymer Nanoparticles. *Eur. Polym. J.* **2019**, *121*, 109306.

(65)   Kolouchova, K.; Sedlacek, O.; Jirak, D.; Babuka, D.; Blahut, J.; Kotek, J.; Vit, M.; Trousil, J.; Konefał, R.; Janouskova, O.; Podhorska, B.; Slouf, M.; Hruby, M. Self-Assembled Thermoresponsive Polymeric Nanogels for ^{19}F MR Imaging. *Biomacromolecules* **2018**, *19*, 3515–3524.

(66)   Sedlacek, O.; Jirak, D.; Galisova, A.; Jager, E.; Laaser, J. E.; Lodge, T. P.; Stepanek, P.; Hruby, M. ^{19}F Magnetic Resonance Imaging of Injectable Polymeric Implants with Multiresponsive Behavior. *Chem. Mater.* **2018**, *30*, 4892–4896.

(67)   Heskins, M.; Guillet, J. E. Solution Properties of Poly(N-Isopropylacrylamide). *J. Macromol. Sci. Part A - Chem.* **1968**, *2*, 1441–1455.

(68)   Bloksma, M. M.; Bakker, D. J.; Weber, C.; Hoogenboom, R.; Schubert, U. S. The Effect of Hofmeister Salts on the LCST Transition of Poly(2-Oxazoline)s with Varying Hydrophilicity. *Macromol. Rapid Commun.* **2010**, *31*, 724–728.

(69)   Sedlacek, O.; Bera, D.; Hoogenboom, R. Poly(2-Amino-2-Oxazoline)s: A New Class of Thermoresponsive Polymers. *Polym. Chem.* **2019**, *10*, 4683–4689.

(70)   de la Rosa, V. R. Poly(2-Oxazoline)s as Materials for Biomedical Applications. *J. Mater. Sci. Mater. Med.* **2014**, *25*, 1211–1225.

(71)   Kotsuchibashi, Y.; Ebara, M.; Aoyagi, T.; Narain, R. Recent Advances in Dual Temperature Responsive Block Copolymers and Their Potential as Biomedical Applications. *Polymers*. **2016**, *8*, 380-405.

(72)   Luxenhofer, R.; Han, Y.; Schulz, A.; Tong, J.; He, Z.; Kabanov, A. V; Jordan, R. Poly(2-Oxazoline)s as Polymer Therapeutics. *Macromol. Rapid Commun.* **2012**, *33*, 1613–1631.

(73)   Hoogenboom, R.; Thijs, H. M. L.; Jochems, M. J. H. C.; van Lankvelt, B. M.; Fijten, M. W. M.; Schubert, U. S. Tuning the LCST of Poly(2-Oxazoline)s by Varying Composition and Molecular Weight: Alternatives to Poly(N-Isopropylacrylamide)? *Chem. Commun.* **2008**, *44*, 5758–5760.

(74) Yamada, S. Surfactant Assemblies (Micelles, Vesicles, Emulsions, Films, Etc.), an Overview BT - Encyclopedia of Polymeric Nanomaterials; Kobayashi, S., Müllen, K., Eds.; Springer Berlin Heidelberg: Berlin, Heidelberg, **2014**, 1–6.

(75) Holder, S.; Sommerdijk, N. New Micellar Morphologies from Amphiphilic Block Copolymers: Disks, Toroids and Bicontinuous Micelles. *Polym. Chem.* **2011**, *2*, 1018-1028.

(76) Blanazs, A.; Armes, S. P.; Ryan, A. J. Self-Assembled Block Copolymer Aggregates: From Micelles to Vesicles and Their Biological Applications. *Macromol. Rapid Commun.* **2009**, *30*, 267–277.

(77) Ward, M. A.; Georgiou, T. K. Thermoresponsive Polymers for Biomedical Applications. *Polymers (Basel).* **2011**, *3*, 1215-1242.

(78) Klouda, L.; Mikos, A. G. Thermoresponsive Hydrogels in Biomedical Applications. *Eur. J. Pharm. Biopharm.* **2008**, *68*, 34–45.

(79) Wagner, V.; Dullaart, A.; Bock, A.-K.; Zweck, A. The Emerging Nanomedicine Landscape. *Nat. Biotechnol.* **2006**, *24*, 1211–1217.

(80) Pridgen, E. M.; Langer, R.; Farokhzad, O. C. Biodegradable, Polymeric Nanoparticle Delivery Systems for Cancer Therapy. *Nanomedicine* **2007**, *2*, 669–680.

(81) Bamrungsap, S.; Zhao, Z.; Chen, T.; Wang, L.; Li, C.; Fu, T.; Tan, W. Nanotechnology in Therapeutics: A Focus on Nanoparticles as a Drug Delivery System. *Nanomedicine* **2012**, *7*, 1253–1271.

(82) Zhang, G.; Zeng, X.; Li, P. Nanomaterials in Cancer-Therapy Drug Delivery System. *Journal of Biomedical Nanotechnology*, **2013**, *9*, 741–750.

(83) Maeda, H.; Bharate, G. Y.; Daruwalla, J. Polymeric Drugs for Efficient Tumor-Targeted Drug Delivery Based on EPR-Effect. *Eur. J. Pharm. Biopharm.* **2009**, *71*, 409–419.

(84) Maeda, H.; Wu, J.; Sawa, T.; Matsumura, Y.; Hori, K. Tumor Vascular Permeability and the EPR Effect in Macromolecular Therapeutics: A Review. *J. Control. Release* **2000**, *65*, 271–284.

(85) Gupta, P.; Vermani, K.; Garg, S. Hydrogels: From Controlled Release to PH-Responsive Drug Delivery. *Drug Discov. Today* **2002**, *7*, 569–579.

(86) Pang, X.; Jiang, Y.; Xiao, Q.; Leung, A. W.; Hua, H.; Xu, C. PH-Responsive Polymer–Drug Conjugates: Design and Progress. *J. Control. Release* **2016**, *222*, 116–129.

(87) Schmaljohann, D. Thermo- and PH-Responsive Polymers in Drug Delivery. *Adv. Drug Deliv. Rev.* **2006**, *58*, 1655–1670.

(88) Popat, A.; Liu, J.; Lu, G. Q. (Max); Qiao, S. Z. A PH-Responsive Drug Delivery System Based on Chitosan Coated Mesoporous Silica Nanoparticles. *J. Mater. Chem.* **2012**, *22*, 11173–11178.

(89) Xing, L.; Zheng, H.; Cao, Y.; Che, S. Coordination Polymer Coated Mesoporous Silica Nanoparticles for PH-Responsive Drug Release. *Adv. Mater.* **2012**, *24*, 6433–6437.

(90) Gao, Q.; Xu, Y.; Wu, D.; Sun, Y.; Li, X. PH-Responsive Drug Release from Polymer-Coated Mesoporous Silica Spheres. *J. Phys. Chem. C* **2009**, *113*, 12753–12758.

(91) Li, M.; Song, W.; Tang, Z.; Lv, S.; Lin, L.; Sun, H.; Li, Q.; Yang, Y.; Hong, H.; Chen, X. Nanoscaled Poly(l-Glutamic Acid)/Doxorubicin-Amphiphile Complex as PH-Responsive Drug Delivery System for Effective Treatment of Nonsmall Cell Lung Cancer. *ACS Appl. Mater. Interfaces* **2013**, *5*, 1781–1792.

(92) Yang, X.; Grailer, J. J.; Rowland, I. J.; Javadi, A.; Hurley, S. A.; Matson, V. Z.; Steeber, D. A.; Gong, S. Multifunctional Stable and PH-Responsive Polymer Vesicles Formed by Heterofunctional Triblock Copolymer for Targeted Anticancer Drug Delivery and Ultrasensitive MR Imaging. *ACS Nano* **2010**, *4*, 6805–6817.

(93) Huo, M.; Yuan, J.; Tao, L.; Wei, Y. Redox-Responsive Polymers for Drug Delivery: From Molecular Design to Applications. *Polym. Chem.* **2014**, *5*, 1519–1528.

(94) Sun, J.-T.; Piao, J.-G.; Wang, L.-H.; Javed, M.; Hong, C.-Y.; Pan, C.-Y. One-Pot Synthesis of Redox-Responsive Polymers-Coated Mesoporous Silica Nanoparticles and Their Controlled Drug Release. *Macromol. Rapid Commun.* **2013**, *34*, 1387–1394.

(95) Zhang, X.; Han, L.; Liu, M.; Wang, K.; Tao, L.; Wan, Q.; Wei, Y. Recent Progress and Advances in Redox-Responsive Polymers as Controlled Delivery Nanoplatforms. *Mater. Chem. Front.* **2017**, *1*, 807–822.

(96) Vogt, A. P.; Sumerlin, B. S. Temperature and Redox Responsive Hydrogels from ABA Triblock Copolymers Prepared by RAFT Polymerization. *Soft Matter* **2009**, *5*, 2347–2351.

(97) Yang, Q.; Tan, L.; He, C.; Liu, B.; Xu, Y.; Zhu, Z.; Shao, Z.; Gong, B.; Shen, Y.-M. Redox-Responsive Micelles Self-Assembled from Dynamic Covalent Block Copolymers for Intracellular Drug Delivery. *Acta Biomater.* **2015**, *17*, 193–200.

(98) Wen, H.; Dong, C.; Dong, H.; Shen, A.; Xia, W.; Cai, X.; Song, Y.; Li, X.; Li, Y.; Shi, D. Engineered Redox-Responsive PEG Detachment Mechanism in PEGylated Nano-Graphene Oxide for Intracellular Drug Delivery. *Small* **2012**, *8*, 760–769.

(99) Luo, Z.; Cai, K.; Hu, Y.; Li, J.; Ding, X.; Zhang, B.; Xu, D.; Yang, W.; Liu, P. Redox-Responsive Molecular Nanoreservoirs for Controlled Intracellular Anticancer Drug Delivery Based on Magnetic Nanoparticles. *Adv. Mater.* **2012**, *24*, 431–435.

(100) Zhuang, Y.; Deng, H.; Su, Y.; He, L.; Wang, R.; Tong, G.; He, D.; Zhu, X. Aptamer-Functionalized and Backbone Redox-Responsive Hyperbranched Polymer for Targeted Drug Delivery in Cancer Therapy. *Biomacromolecules* **2016**, *17*, 2050–2062.

(101) Shi, C.; Guo, X.; Qu, Q.; Tang, Z.; Wang, Y.; Zhou, S. Actively Targeted Delivery of Anticancer Drug to Tumor Cells by Redox-Responsive Star-Shaped Micelles. *Biomaterials* **2014**, *35*, 8711–8722.

(102) Linsley, C. S.; Wu, B. M. Recent Advances in Light-Responsive on-Demand Drug-Delivery Systems. *Ther. Deliv.* **2017**, *8*, 89–107.

(103) de la Rosa, V. R.; Woisel, P.; Hoogenboom, R. Supramolecular Control over Thermoresponsive Polymers. *Mater. Today* **2016**, *19*, 44–55.

(104) WALBA, H.; ISENSEE, R. W. Acidity Constants of Some Arylimidazoles and Their Cations. *J. Org. Chem.* **1961**, *26*, 2789–2791.

(105) Kolouchova, K.; Jirak, D.; Groborz, O.; Sedlacek, O.; Ziolkowska, N.; Vit, M.; Sticova, E.; Galisova, A.; Svec, P.; Trousil, J.; Hajek, M.; Hruby, M. Implant-Forming Polymeric

^{19}F MRI-Tracer with Tunable Dissolution. *J. Control. Release* **2020**, *327*, 50–60.

(106) Priya James, H.; John, R.; Alex, A.; Anoop, K. R. Smart Polymers for the Controlled Delivery of Drugs – a Concise Overview. *Acta Pharm. Sin. B* **2014**, *4*, 120–127.

(107) Funkhouser, J. Reinventing Pharma: The Theranostic Revolution. *Curr. Drug Discov.* **2002**, 17-36.

(108) Del Vecchio, S.; Zannetti, A.; Fonti, R.; Pace, L.; Salvatore, M. Nuclear Imaging in Cancer Theranostics. *Quarterly Journal of Nuclear Medicine and Molecular Imaging*. **2007**, *51*, 152-215.

(109) Kelkar, S. S.; Reineke, T. M. Theranostics: Combining Imaging and Therapy. *Bioconjug. Chem.* **2011**, *22*, 1879-903.

(110) Yoo, D.; Lee, J. H.; Shin, T. H.; Cheon, J. Theranostic Magnetic Nanoparticles. *Acc. Chem. Res.* **2011**, *44*, 863–874.

(111) Chen, F.; Ehlerding, E. B.; Cai, W. Theranostic Nanoparticles. *J. Nucl. Med.* **2014**, *55* 1919–1922.

(112) Ahmed, N.; Fessi, H.; Elaissari, A. Theranostic Applications of Nanoparticles in Cancer. *Drug Discovery Today* **2012**, *17*, 928-34.

(113) Loukotová, L.; Kučka, J.; Rabyk, M.; Höcherl, A.; Venclíková, K.; Janoušková, O.; Páral, P.; Kolářová, V.; Heizer, T.; Šefc, L.; Štěpánek, P.; Hrubý, M. Thermoresponsive β-Glucan-Based Polymers for Bimodal Immunoradiotherapy – Are They Able to Promote the Immune System? *J. Control. Release* **2017**, *268*, 78–91.

(114) Ulrich, F.; Zhaoping, D.; Hendrik, H.; Sebastian, J.; Gaby, R.; Christoph, J.; Rolf, S.; Jürgen, S. *In Vivo* Monitoring of Inflammation After Cardiac and Cerebral Ischemia by Fluorine Magnetic Resonance Imaging. *Circulation* **2008**, *118*, 140–148.

(115) Boehm-Sturm, P.; Mengler, L.; Wecker, S.; Hoehn, M.; Kallur, T. *In Vivo* Tracking of Human Neural Stem Cells with ^{19}F Magnetic Resonance Imaging. *PLoS One* **2011**, *6*, e29040.

(116) van Heeswijk, R. B.; Pilloud, Y.; Flögel, U.; Schwitter, J.; Stuber, M. Fluorine-19 Magnetic Resonance Angiography of the Mouse. *PLoS One* **2012**, *7*, e42236.

(117) Zhu, J.; Zhang, H.; Chen, K.; Li, Y.; Yang, Z.; Chen, S.; Zheng, X.; Zhou, X.; Jiang, Z.-X. Peptidic Monodisperse PEG "Comb" as Multifunctional "Add-On" Module for Imaging-Traceable and Thermo-Responsive Theranostics. *Adv. Healthc. Mater.* **2020**, *9*, e1901331.

(118) Oishi, M.; Sumitani, S.; Nagasaki, Y. On−Off Regulation of ^{19}F Magnetic Resonance Signals Based on PH-Sensitive PEGylated Nanogels for Potential Tumor-Specific Smart ^{19}F MRI Probes. *Bioconjug. Chem.* **2007**, *18*, 1379–1382.

(119) Huang, X.; Huang, G.; Zhang, S.; Sagiyama, K.; Togao, O.; Ma, X.; Wang, Y.; Li, Y.; Soesbe, T. C.; Sumer, B. D.; Takahashi, M.; Sherry, A. D.; Gao, J. Multi-Chromatic PH-Activatable ^{19}F-MRI Nanoprobes with Binary ON/OFF PH Transitions and Chemical-Shift Barcodes. *Angew. Chemie Int. Ed.* **2013**, *52*, 8074–8078.

(120) Wang, K.; Peng, H.; Thurecht, K. J.; Puttick, S.; Whittaker, A. K. PH-Responsive Star Polymer Nanoparticles: Potential ^{19}F MRI Contrast Agents for Tumour-Selective Imaging. *Polym. Chem.* **2013**, *4*, 4480–4489.

(121) Guo, C.; Xu, S.; Arshad, A.; Wang, L. A PH-Responsive Nanoprobe for Turn-on ^{19}F-Magnetic Resonance Imaging. *Chem. Commun.* **2018**, *54*, 9853–9856.

(122) Fu, C.; Herbst, S.; Zhang, C.; Whittaker, A. K. Polymeric ^{19}F MRI Agents Responsive to Reactive Oxygen Species. *Polym. Chem.* **2017**, *8*, 4585–4595.

(123) Xie, D.; Kim, S.; Kohli, V.; Banerjee, A.; Yu, M.; Enriquez, J. S.; Luci, J. J.; Que, E. L. Hypoxia-Responsive ^{19}F MRI Probes with Improved Redox Properties and Biocompatibility. *Inorg. Chem.* **2017**, *56*, 6429–6437.

(124) Yu, J.-X.; Kodibagkar, V. D.; Hallac, R. R.; Liu, L.; Mason, R. P. Dual ^{19}F/^{1}H MR Gene Reporter Molecules for *in Vivo* Detection of β-Galactosidase. *Bioconjug. Chem.* **2012**, *23*, 596–603.

(125) Liu, L.; Kodibagkar, V. D.; Yu, J.-X.; Mason, R. P. ^{19}F-NMR Detection of LacZ Gene Expression *via* the Enzymic Hydrolysis of 2-Fluoro-4-Nitrophenyl β-d-Galactopyranoside *in Vivo* in PC3 Prostate Tumor Xenografts in the Mouse. *FASEB J.* **2007**, *21*, 2014–2019.

(126) Akazawa, K.; Sugihara, F.; Nakamura, T.; Mizukami, S.; Kikuchi, K. Highly Sensitive Detection of Caspase-3/7 Activity in Living Mice Using Enzyme-Responsive ^{19}F MRI Nanoprobes. *Bioconjug. Chem.* **2018**, *29*, 1720–1728.

(127) Moad, G.; Rizzardo, E.; Thang, S. Radical Addition-Fragmentation Chemistry in Polymer Synthesis. *Polymer (Guildf).* **2008**, *49*, 1079–1131.

(128) Krieg, A.; Weber, C.; Hoogenboom, R.; Becer, C. R.; Schubert, U. S. Block Copolymers of Poly(2-Oxazoline)s and Poly(Meth)Acrylates: A Crossover between Cationic Ring-Opening Polymerization (CROP) and Reversible Addition–Fragmentation Chain Transfer (RAFT). *ACS Macro Lett.* **2012**, *1*, 776–779.

(129) Quirk, R. P.; Kinning, D. J.; Fetters, L. J. Chapter 1 - Block Copolymers; Allen, G., Bevington, J. C. B. T.-C. P. S. and S., Eds.; Pergamon: Amsterdam, **1989**; 1–26.

(130) Capella, V.; Rivero, R. E.; Liaudat, A. C.; Ibarra, L. E.; Roma, D. A.; Alustiza, F.; Mañas, F.; Barbero, C. A.; Bosch, P.; Rivarola, C. R.; Rodriguez, N. Cytotoxicity and Bioadhesive Properties of Poly-N-Isopropylacrylamide Hydrogel. *Heliyon* **2019**, *5*, e01474.

(131) Wyffels, L.; Verbrugghen, T.; Monnery, B. D.; Glassner, M.; Stroobants, S.; Hoogenboom, R.; Staelens, S. MPET Imaging of the Pharmacokinetic Behavior of Medium and High Molar Mass [89]Zr-Labeled Poly(2-Ethyl-2-Oxazoline) in Comparison to Poly(Ethylene Glycol). *J. Control. Release* **2016**, *235*, 63–71.

(132) Seymour, L. W.; Duncan, R.; Strohalm, J.; Kopeček, J. Effect of Molecular Weight (M_w) of *N*-(2-Hydroxypropyl)Methacrylamide Copolymers on Body Distribution and Rate of Excretion after Subcutaneous, Intraperitoneal, and Intravenous Administration to Rats. *J. Biomed. Mater. Res.* **1987**, *21*, 1341–1358.

(133) Knop, K.; Hoogenboom, R.; Fischer, D.; Schubert, U. S. Poly(Ethylene Glycol) in Drug Delivery: Pros and Cons as Well as Potential Alternatives. *Angew. Chemie Int. Ed.* **2010**, *49*, 6288–6308.

(134) Glassner, M.; Palmieri, L.; Monnery, B. D.; Verbrugghen, T.; Deleye, S.; Stroobants, S.; Staelens, S.; wyffels, L.; Hoogenboom, R. The Label Matters: MPET Imaging of the Biodistribution of Low Molar Mass 89Zr and 18F-Labeled Poly(2-Ethyl-2-Oxazoline).

Biomacromolecules **2017**, *18*, 96–102.

(135) Sedláček, O.; Černoch, P.; Kučka, J.; Konefal, R.; Štěpánek, P.; Vetrík, M.; Lodge, T. P.; Hrubý, M. Thermoresponsive Polymers for Nuclear Medicine: Which Polymer Is the Best? *Langmuir* **2016**, *32*, 6115–6122.

(136) Atta-ur-Rahman; Choudhary, M. I.; Atia-tul-Wahab. Chapter 5 - The Second Dimension; Atta-ur-Rahman, Choudhary, M. I., Atia-tul-Wahab, B. T.-S. P. with N. M. R. S. (Second E., Eds.; Academic Press: Boston, **2016**; 191–225.

(137) Moore, J. C. Gel Permeation Chromatography. I. A New Method for Molecular Weight Distribution of High Polymers. *J. Polym. Sci. Part A Gen. Pap.* **1964**, *2*, 835–843.

(138) Brown W. Dynamic Light Scattering: The Method and Some Applications. Chapter 16 Diffusion Spectroscopy **1993**.

(139) Kim, H.-A.; Seo, J.-K.; Kim, T.; Lee, B.-T. Nanometrology and Its Perspectives in Environmental Research. *Environ. Health Toxicol.* **2014**, *29*, e2014016.

(140) Andersen, K. E.; Hansen, M. B. Static Light Scattering. In Methods and Applications of Inversion; **2005**.

(141) Zhang, F.; Roosen-Runge, F.; Skoda, M.; Jacobs, R.; Wolf, M.; Callow, P.; Frielinghaus, H.; Pipich, V.; Prévost, S.; Schreiber, F. Hydration and Interactions in Protein Solutions Containing Concentrated Electrolytes Studied by Small-Angle Scattering. *Phys. Chem. Chem. Phys.* **2012**, *14*, 2483–2493.

(142) Ruska, E. The Early Development of Electron Lenses and Electron Microscopy. *Microsc. Acta. Suppl.* **1980**, *5*, 1-140.

(143) Chianese, A.; Bravi, M.; Fazio, E. Turbidimetry and Nephelometry. In Industrial Crystallization Process Monitoring and Control; **2012**.

(144) Luo, C.; Fu, W.; Li, Z.; Zhao, B. Multi-Responsive Polymethacrylamide Homopolymers Derived from Tertiary Amine-Modified l-Alanine. *Polymer (Guildf).* **2016**, *101*, 319–327.

(145) Sun, J.; Peng, Y.; Chen, Y.; Liu, Y.; Deng, J.; Lu, L.; Cai, Y. Effect of Molecular Structure on Thermoresponsive Behaviors of Pyrrolidone-Based Water-Soluble Polymers. *Macromolecules* **2010**, *43*, 4041–4049.

(146) Wang, X.; Wu, C. Light-Scattering Study of Coil-to-Globule Transition of a Poly(*N*-Isopropylacrylamide) Chain in Deuterated Water. *Macromolecules* **1999**, *32*, 4299–4301.

(147) Bianchi, A.; Mauri, M.; Bonetti, S.; Koynov, K.; Kappl, M.; Lieberwirth, I.; Butt, H.-J.; Simonutti, R. Hierarchical Self-Assembly of PDMA-b-PS Chains into Granular Nanoparticles: Genesis and Fate. *Macromol. Rapid Commun.* **2014**, *35*, 1994–1999.

(148) Snyder, S. L.; Sobocinski, P. Z. An Improved 2,4,6-Trinitrobenzenesulfonic Acid Method for the Determination of Amines. *Anal. Biochem.* **1975**, *64*, 284–288.

(149) Lubach, J.; Drenth, W. Enolization and Oxidation: II. Oxidation of Ferrocene by Molecular Oxygen and Hydrogen Peroxide in Acidic Media. *Recl. des Trav. Chim. des Pays-Bas* **1973**, *92*, 586–592.

(150) Epton, R.; Hobson, M. E.; Marr, G. Oxidation of Ferrocene and Some Substituted

Ferrocenes in the Presence of Horseradish Peroxidase. *J. Organomet. Chem.* **1978**, *149*, 231–244.

(151) Traverso, O.; Scandola, F. Photooxidation of Ferrocene in Halocarbon Solvents. *Inorganica Chim. Acta* **1970**, *4*, 493–498.

(152) Bao, D.; Millare, B.; Xia, W.; Steyer, B. G.; Gerasimenko, A. A.; Ferreira, A.; Contreras, A.; Vullev, V. I. Electrochemical Oxidation of Ferrocene: A Strong Dependence on the Concentration of the Supporting Electrolyte for Nonpolar Solvents. *J. Phys. Chem. A* **2009**, *113*, 1259–1267.

(153) Chatterjee, S. Oxidative Stress, Inflammation, and Disease. In Oxidative Stress and Biomaterials; Dziubla, T., Butterfield, D. A., Eds.; **2016**; 404.

(154) Gufler, H.; Laubenberger, J.; DeGregorio, G.; Dohnicht, S.; Langer, M. Pelvic Floor Descent: Dynamic MR Imaging Using a Half-Fourier RARE Sequence. *J. Magn. Reson. Imaging* **1999**, *9*, 378–383.

(155) Schmieder, A. H.; Caruthers, S. D.; Keupp, J.; Wickline, S. A.; Lanza, G. M. Recent Advances in 19-Fluorine Magnetic Resonance Imaging with Perfluorocarbon Emulsions. *Engineering* **2015**, *1*, 475–489.

(156) Wang, X.; Zhen, X.; Wang, J.; Zhang, J.; Wu, W.; Jiang, X. Doxorubicin Delivery to 3D Multicellular Spheroids and Tumors Based on Boronic Acid-Rich Chitosan Nanoparticles. *Biomaterials* **2013**, *34*, 4667–4679.

(157) Clancy, R. L.; Brown, E. B. *In Vivo* CO-2 Buffer Curves of Skeletal and Cardiac Muscle. *Am. J. Physiol.* **1966**, *6*, 1309-1312.

(158) Böning, D.; Klarholz, C.; Himmelsbach, B.; Hütler, M.; Maassen, N. Extracellular Bicarbonate and Non-Bicarbonate Buffering against Lactic Acid during and after Exercise. *Eur. J. Appl. Physiol.* **2007**, *100*, 457-467.

(159) Kucka, J.; Hrubý, M.; Lebeda, O. Biodistribution of a Radiolabelled Thermoresponsive Polymer in Mice. *Appl. Radiat. Isot.* **2010**, *68*, 1073–1078.

(160) Takezawa, T.; Mori, Y.; Yoshizato, K. Cell Culture on a Thermo-Responsive Polymer Surface. *Nat. Biotechnol.* **1990**, *8*, 854-856.

(161) Wang, J.; Ayano, E.; Maitani, Y.; Kanazawa, H. Tunable Surface Properties of Temperature-Responsive Polymer-Modified Liposomes Induce Faster Cellular Uptake. *ACS Omega* **2017**, *2*, 316-325.

Appendix 1

Kolouchova, K.; Sedlacek, O.; Jirak, D.; Babuka, D.; Blahut, J.; Kotek, J.; Vit, M.; Trousil, J.; Konefal, R.; Janouskova O.; Podhorska, B.; Slouf, M.; Hruby, M. Self-Assembled Thermoresponsive Polymeric Nanogels for ^{19}F MR Imaging. *Biomacromolecules* **2018**, *19*, 3515-3524. IF 5.667

Appendix 2

Babuka, D.; **Kolouchova, K.**; Hruby, M.; Groborz, O.; Tosner, Z.; Zhigunov, A.; Stepanek, P. Investigation of the internal structure of thermoresponsive diblock poly(2-methyl-2-oxazoline)-*b*-poly[*N*-(2,2-difluoroethyl)acrylamide] copolymer nanoparticles, *European Polymer Journal* **2019**, *121*, e109306. IF 3.862

Appendix 3

Kolouchova, K.; Jirak, D.; Groborz, O.; Sedlacek, O.; Ziolkowska, N.; Vit, M.; Sticova, E.; Galisova, A.; Svec, P.; Trousil, J.; Hajek, M.; Hruby, M. Implant-forming polymeric ^{19}F MRI-tracer with tunable dissolution, *Journal of Controlled Release,* **2020**, *327*, 50-60. IF 7.727

Appendix 4

Jirak, D.; Galisova, A.; **Kolouchova, K.**; Babuka, D.; Hruby, M. Fluorine polymer probes for magnetic resonance imaging: quo vadis? *Magnetic Resonance Materials in Physics, Biology and Medicine* **2019**, *32*, 173-185. IF 1.956